A study on the fracturing behavior and scaling of carbon/glass hybrid composites

Abhishek Das

A thesis submitted in partial fulfillment of the requirements for the degree of

Master of Science

University of Washington

2018

Reading Committee:

Marco Salviato, Chair

Mark Tuttle

Junlan Wang

Program Authorized to Offer Degree:
Mechanical Engineering

University of Washington

Abstract

A study on the fracturing behavior and scaling of carbon/glass hybrid composites

Abhishek Das

Chair of the Supervisory Committee:
Marco Salviato
Department of Aeronautics and Astronautics

One of the factors hindering the broad application of composites is their relative brittleness leading to sudden failure with no significant damage precursors. This makes designing with composites very challenging and frequent health monitoring becomes an expensive need. In the past ten years, significant work has been focused on introducing a certain level of ductility in composite structures through techniques such as adding nano-particles or leveraging a complex heterogeneous mesostructure such as in discontinuous fiber composites (DFCs). Hybridization is another such alternative and studies on carbon/glass hybrid composites have shown promising results. While extensive work has been done to characterize the behavior of smooth (un-notched or un-cracked) hybrid specimens, very little is known about the fracturing behavior in the presence of sharp notches. This lack of knowledge is an impediment to the widespread use of such materials. This work aims at filling this knowledge gap by means of a thorough experimental and computational investigation.

Fracture in quasi brittle materials such as composites involve a number of non-linear phenomenon which makes it impossible to characterize them using Linear Elastic fracture Mechanics (LEFM) techniques. Moreover, a wide class of materials such as nanocomposites, concrete, composites, polymers show fracture behavior which can be characterized using a bi-linear cohesive law shape. This study develops a modeling technique which incorporates

a bi-linear cohesive law in ABAQUS models to simulate fracture. A MATLAB subroutine was devloped to generate Damage displacement data for bi-linear cohesive crack laws. This data was an input to the material model in ABAQUS which was used for the simulations. These simulation results were used to obtain size effect plots which characterize the specific material system and cohesive crack law.

Once the modeling technique was established, a dimensional analysis was carried out to obtain the dimensionless parameters which are critical to the cohesive zone simulations. These dimensionsionless paramters were used to obtain size effect curves in the dimensionless space. Subsequently, the parameters were swept over a wide range of values to obtain master curves spanning different cohesive law shpaes and material properties. Finally a universal fitting equation was generated which can be used to accurately capture these size effect curves.

The second part of the work involved experiments on Carbon/glass hybrid composites. Experiments were performed on Single Edge Notch Tension (SENT) samples over three different sizes to obtain experimental size effect curves. Finally an attempt was made to use the modeling technique developed previously to explain the results obtained through these experiments in order to explain the fracture of the hybrid composites.

TABLE OF CONTENTS

LIST OF FIGURES

LIST OF TABLES

ACKNOWLEDGMENTS

I would like to express my gratitude to my supervisor Prof. Marco Salviato his kind suggestions and support.

I would also like to thank the other members of my thesis commitee, Prof. Mark Tuttle and Prof. Junlan Wang for their valuable feedback and suggestions.

I would like to thank my lab mates Yao, Antonio and Seunghyun for their assistance with experiments and simulations.

Finally I would like to thank my friends here in University of Washington and my parents Jaya and Anandamoy for their support and encouragement during the duration of my research.

Chapter 1

INTRODUCTION

The thirst for knowledge and a never ending desire for improvement has driven mankind towards technological progress. The same values were the cornerstones for advancement in material science and technology. The driving factors which have lead to constant improvement in material science fall in line with the industry requirements to develop better structures - machines, buildings, roads, aircrafts, automobiles, electronic devices .etc. These requirements can be of different categories. We may need stronger materials or materials with higher yield/ultimate strength to withstand higher loads. Materials with high stiffness may be desirable for applications where minimizing deflection is the priority. In some cases low density materials with good strength properties are required to reduce weight. Similarly we may need materials with high or low thermal conductivity if we want to facilitate or limit heat conduction. These wide range of requirements opens up a plethora of opportunities for scientists and researchers to come up with ingenious ways to create new and improved materials or establish guidelines for material selection suited to the requirements.

1.1 History of Composites

The main idea behind using composites is to combine two or more materials in a way such that the merits of each of the components are retained while masking their deficiencies.

One of earliest uses of composites involved the Mesopotamians at around 3000 B.C, who combined wooden strips at various angles to create plywood. Around 1500 BC straw was used to reinforce mud bricks, pottery and boats by Egyptians and Mesopotamians. Cement,

also a type of composite has been described in *The Ten Books on Architecture* [1] as early as 25 B.C. The type of cement described was reported to be similar or even superior to Portland Cement, the most common type of cement used today.

Around 1200 A.D Mongolians invented the composite bow [61]. It was composed of wood, bone, bamboo, cattle tendons and animal glue wrapped in birch bark. These bows were known to be very powerful and accurate and were integral to Genghis Khan's dominance in warfare.

Around the late 1800s and early 1900s, the development of composites received a major boost with the advent of plastics. Since plastics by themselves were not robust enough, they needed to be reinforced to improve their strength and rigidity. In 1935, Games Slayter of Owens Corning introduced glass fiber [19], which when combined with polymers lead to a strong yet lightweight material.This lead to the FRP (Fiber Reinforced Polymer) industry.

World War II lead to further advancement in composites which had the desirable qualities of being lightweight but strong at the same time. Beyond such patent benefits, certain composites had some unique advantages, such as fiberglass - which was used to shelter electronic radar equipment because it was transparent to radio frequencies. Even after the war, composites were being extensively promoted for commercial use, such as in the manufacture of boat hulls, surfboards and in a major way in the automotive industry, as seen in the 1953 Corvette which used Fiberglass impregnated with resins. During this time two major molding methods emerged as the predominant technique used in the automotive industry and other industries which used composites. They were the compression molding of Sheet Molding Compound (SMC) and Bulk Molding Compound (BMC).

Brandt Goldsworthy often regarded as the "grandfather of composites" played a major role in improving composite fabrication techniques. He invented the pultrusion technique [6]

for manufacturing fiberglass reinforced products. This technique is still used today to manufacture tool handles, pipes, arrow shafts, armor, train floors and medical devices among others.

The 1950s and 60s also saw some major progress in the composites industry. Filament winding [8] was a fabrication procedure used to make large scale rocket motors, which was the driving force behind space exploration in the 1960s and beyond. In 1961 the first carbon fiber was patented [48]. Carbon fibers improved the stiffness to weight ratios in thermosets, thus leading to their increased application in the aerospace, automotive and sports equipment industries. Even then, the marine market was the largest consumer of composites in the 1960s.

In the 1970s, plastic resins and improved reinforcing fibers were developed. Aramid fiber (Kevlar) developed by DuPont [32] was used in body armors due its high tensile strength, density and low weight. Carbon fibers started replacing steel in various components. Fibers made of ultra high molecular weight polyethylene were developed. Improved resins were developed which could withstand higher temperatures and corrosive environments. During this period, the automotive industry surpassed the marine industry as the largest consumer of composite materials, a position it holds even today. Mar-Bal was founded in 1970, and they started making custom molded components for the electrical, motor Assembly and small appliance industries. It went on to become the most integrated Thermoset Composites Solution Provider in the world.

Around the mid 1990s, composites had entered the mainstream industry when it came to manufacturing and construction. It started replacing metals and other traditional materials in various components in industries such as appliances, construction, electronics and transportation. The common people started coming in contact with composites in their everyday lives. The development of the 787 Dreamliner in the mid 2000s established the

fact that composites are well suited for high strength and rigid applications. Composites are still widely used in the automotive, aerospace and marine industries. Of late, they are also finding application in the realm of nanotechnology.

The widespread use of composites and more severe requirements will drive research in composite technology. Their areas of application will only keep increasing. There is a constant demand for lighter, stronger, stiffer and more robust composites which can benefit the construction, aerospace and automotive industry. Currently, research in composites is also bent towards developing environment friendly resins and fibers. The demand for improved composite materials will drive their advancement for many more decades.

1.2 Carbon fibers

Carbon fibers play a major role in the composites industry. The first high performance Carbon fibers were created by Roger Bacon in 1958 [48] at the Union Carbide Parma Technical Center located outside Cleveland, Ohio. Strands of Rayon were heated until they were carbonized to produce these fibers. The process produced fibers containing only 20% Carbon and they had low strength and stiffness. Improved methods of producing Carbon fibers were discovered over the next few years. In 1960, Richard Millington of H.I. Thompson Fiberglas Co. was successful in producing a high carbon content (99%) fiber starting with Rayon as a raw material [39]. These Carbon fibers were sufficiently stiff and strong and thus could be used in applications requiring materials with high strength to weight ratios.Since then, a number of other methods were developed to manufacture Carbon fibers which showed improved results. PAN based manufacturing of Carbon fibers gained in prominence. Japanese companies such as Toray, Nippon Carbon, Toho Rayon and Mitsubishi were instrumental in the development of Crabon fiber fabrication technology and are considered among the world leaders in this area. Fibers with higher strength and stiffness were developed such as T400 from Toray with a tensile strength of 4,000 MPa elastic modulus of 400 GPa. These

fibers were used extensively in the aerospace industry - both in military and civil aviation by companies such as McDonnell Douglas, Boeing and Airbus.

Carbon fiber is a long strand of material around 5-10 microns in diameter and is composed mainly of Carbon atoms. Fig. 1.1 [34] shows a carbon fiber strand compared to a human hair. The Carbon atoms are bonded together in microscopic crystals which are mostly aligned to the long axis of the fiber and this alignment is the secret to the high strength of Carbon fibers. A large number of Carbon fibers can be twisted together to form yarns shown in Fig. 1.2, which can then be combined with epoxy to form different composites. The yarns may also be used by themselves in structural components.

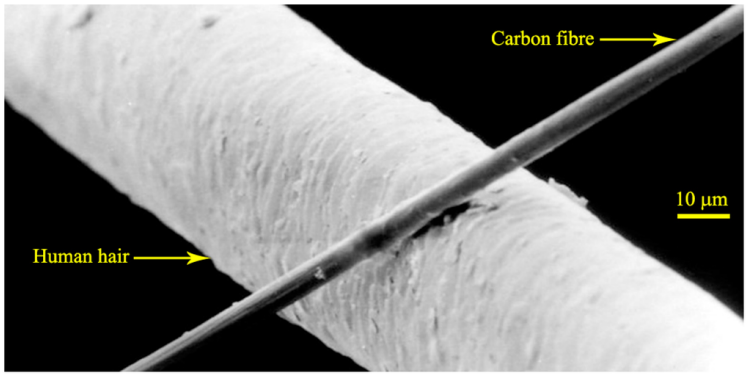

Figure 1.1: Carbon fiber compared to human hair [34]

The raw material used for producing carbon fiber is called the precursor. Around 90% of the Carbon Fibers produced today have polyacrylonitrile(PAN) as the precursor. These raw materials are nothing but organic polymers with long strings of molecules held together by Carbon atoms.Other raw materials used include Rayon and petroleum pitch. The exact formulation of the raw materials are specific to the company and are generally kept as a trade secret.

Figure 1.2: Yarn of Carbon fiber

1.2.1 Manufacturing Carbon Fibers

The manufacturing process involves drawing the precursor into long strands and subsequently heating them to very high temperatures in the absence of oxygen. The lack of oxygen prevents them from burning and the high temperature causes the atoms to vibrate vigorously, thus expelling all atoms other than Carbon. This process is called carbonization. The major steps in the manufacturing process (Fig. 1.3) when PAN is used as the precursor are as follows:

1. **Spinning** - Acrylonitrile plastic powder and another type of plastic such as methyl acrylate or methyl methacrylate are mixed and reacted together in the presence of catalyst to form PAN plastic. It is then spun to fibers thus forming its internal atomic structure. They are subsequently washed and stretched to the desired diameter. The stretching step is instrumental in aligning the molecules with the fiber thus leading to closely bonded carbon crystals after Carbonization.

2. **Stabilizing** - Before Carbonization the fibers need to undergo chemical alteration to convert their linear bonding to a more stable ladder bonding. This is achieved by heating the fibers to 390-590 °F for 30-120 minutes in the presence of air which causes

the fibers to pick oxygen molecules thus altering their atomic bonding pattern. This leads to stabilization of the fibers.

3. **Carbonizing** - The stabilized fibers are heated in an oxygen free furnace containing other gases at high pressure to a temperature of 1,830-5,500 °F for several minutes. This heating process leads to the fibers losing various atoms other than Carbon (a small percentage of Carbon atoms may also be lost). As a result of this we are left with tightly bonded Carbon crystals that are more or less aligned parallel to the long axis of the fiber.

4. **Surface Treatment** - The surface of the Carbon fiber obtained after Carbonization is not suited to bond with other materials (such as epoxies) to form composites. In order to obtain a slightly rougher surface for mechanical bonding and also to facilitate bonding with other materials, the surface is oxidized by immersing fibers in an oxygen rich environment.

5. **Sizing** - Sizing is the process of coating the fibers to protect them from damage during weaving and winding. The coating materials are chosen such that they are compatible with the adhesives used in composite materials. The fibers are then wound into cylinders called bobbins which can then be twisted to yarns of desired sizes using spinning machines.

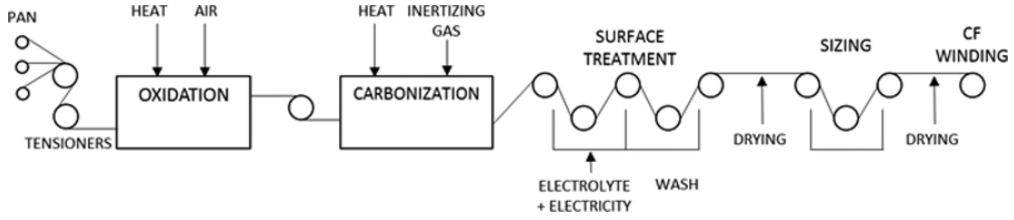

Figure 1.3: Schematic of the Carbonization process [20]

1.2.2 Mechanical properties and applications of Carbon Fibers

The main advantage of Carbon fibers which makes them valuable in structural applications is their high stiffness to weight ratio and strength to weight ratio. The tensile strength of Carbon fibers is normally more than 1 GPa and easily reaches values of 3.5-4 GPa and sometimes even 5.5 GPa or higher [59]. The Young's Modulus is around 230 GPa and can go upto 500 GPa or even higher for high modulus grade Carbon fibers [59]. Even then, the density of Carbon fibers with epoxy resin are normally limited to 2000 kg/m^3 [40]. Such strong mechanical properties at low densities makes it attractive to automotive and aerospace industries where light weight components are highly desirable.

Carbon fiber in composites is used in many cases in the form of Carbon fiber reinforced polymer (CFRP). In general most of the aircrafts built these days use CFRP in many of its structural components. Carbon fiber is being used by SpaceX for its super heavy-lift launch vehicle, the ITS launch vehicleas well as the two very large spacecraft that will be launched by it, the Interplanetary Spaceship and the ITS tanker. The high strength to weight ratio also makes it very useful in the automotive racing industry.

1.3 Reinforcement in composites

Reinforcement is the process of strengthening the matrix and thereby improving the structural properties of the composite. Fiber reinforced polymer composites is very common and involves reinforcing a polymeric matrix with stiff fibers. While the fibers by themselves are stiff and have high strength, they need to bonded together to be useful structural entities. The polymer matrix plays the role of holding the fibers together to provide the composite its structural integrity.

Carbon Fiber reinforced polymer (CFRP) is one of the most useful reinforced polymer

composite. As mentioned previously, CFRP is extensively used in the industry. Their structural robustness is the reason for their prevalence in the industry and thus, their wide range of applications deserve a detailed description.

CFRP had its earliest applications applications in the sports and aerospace industry. [43] highlights the use of CFRP in racquets and golf clubs due to its high strength and stiffness and low weight - a combination of properties ideal for sports-persons in this domain. Since then CFRPs have spread to other sporting equipments such as skis [22], skateboards [21], racquet sports [65](tennis being the leader), golf clubs [24] and sports bikes [51].

The aerospace industry has always been a major market for CFRP. Earlier, they were used in small quantities in parts such as the rudders, spoilers, airbrakes etc. But, with time CFRP and composites in general are being increasingly used in aircrafts.The first instance of composites being used in a major component in a commercial aircraft was by Airbus in 1983 in the rudder of A300 and A310 A honeycomb core with CFRP plates was a part of the elevator in A310 [46] . In the A320, the tail structure, fuselage belly skin,trailing-edge flaps and flap-track fairings, spoilers, ailerons, wheel doors,etc . among other components were made of composites thus making up 28% by weight of the airframe [46]. The use of composites increased further in the later Airbus models. The world's largest aircraft - the A380 is around 22% composites by weight. CFRP is used in the top and bottom skin panels, the front, centre and rear spars, rear pressure bulkhead, the upper deck floor beams, the ailerons, spoilers and outer flaps [46]. The Boeing 777 uses composites in its wings fixed leading edge, the trailing-edge panels, the flaps and flaperons, the spoilers, and the outboard aileron thus making up 20% by weight. The Boeing 787 Dreamliner uses 50% composites in its structural components with most of it being CFRP in its primary structure [46] . According to [37] the high usgae of composites makes the aircraft 10,000 lb lighter and and uses around 20% less fuel than a comparable sized aircraft made with all aluminum. The Airbus A350 XWB has its wing spars and fuselage both made of CFRP and at 52% of the total weight made of

CFRP it has surpassed the Boeing 787 as the aircraft with the highest weight percentage of CFRP till date. According to [41] the increased use of composites in the A350 XWB has also increased its service intervals from 6 to 12 years thus reducing maintenance costs significantly.

The uses of CFRP in aerospace in not limited to commercial aircrafts. They are also used extensively in defense aircrafts and fighter jets. The Military Aircraft Division demonstrated the first use of Carbon fiber composites in structural applications with the Jet Provost trim tab, flown in 1970 [33]. The Experimental Aircraft Project (EAP) contained 25% Carbon fiber composites by weight [33]. The use of CFRPs have kept on increasing ever since. Many European fighter jets have at least 20% by weight Carbon Fiber composites in their structures. The Dassault Rafael is 26% composite whereas it ranges from 20 to 25 % for the Saab Gripen and EADS Mako [46]. Around 40% of the structural weight if the Eurofighter is Carbon Fiber reinforced composite [46].

In high end automobile racing, reduction in weight is of paramount importance, due to which, CFRP is extensively used in this industry. The high strength to weight ratio and its obvious benefits mitigate the high cost of using CFRP in their construction. Omnidirectional carbon fiber weaves, which apply strength in all directions as opposed to normal CFRPs which offer high strength in only one direction, are used in high performance cars in the "safety cell" monocoque chassis assembly. [53] gives a review of the current and future use of CFRP in automobiles. The latest McLaren MP4-12C supercar contains a CFRP MonoCell tub, moulded as a single-piece which is intended to protect the occupants [53]. As mentioned in [53], the re-engineered Murcielago LP670-4 SV is 220 lbs lighter due to the use of CFRP, which not only led to a better weight to power ratio but also improved its agility. The Sesto Elemento, a demonstrator concept car by Lamborghini weighs only 999 kgs. The 2011 Z06 Carbon Limited Edition Corvette by Chevrolet features a carbon fibre hood, roof panel with a full-width body spoiler, rocker panels and air splitters. The Tesla Roadster also demonstrated extensive use of CFRP in its body. Even in everyday road cars, the use

of CFRP is catching up as more people acquire expertise in their use and they become less expensive.

1.4 Problems associated with Carbon fibers

The high stiffness and strength of Carbon fibers and CFRP combined with its low density makes it an ideal material for structural applications. However, its prevalence in the industry is still nowhere near that of metals or other conventional materials used in structural applications. This can be attributed to two main reasons:

1. **Cost** - Carbon fiber and CFRP costs around 10-12 times that of steel. The raw material (PAN) used to make Carbon fibers is quite expensive to start with. On top of that, the manufacturing process used to make Carbon Fibers is complicated, consumes a lot of power, involves powerful machinery and leads to a lot of waste material. Treatment of waste products also adds to the cost. Once the Carbon fiber is produced, they need to stretched and aligned properly so that we can harness its strong unidirectional properties. Subsequently, there is also the process of integrating them with polymer resins as reinforcements, to make them suitable for structural applications. They all add up to make the procedure of producing CFRP a very expensive one.

2. **Brittle failure** - Even though Carbon fiber based composites have exceptional strength and stiffness properties coupled with a low density, they show brittle failure. Components made of Carbon fiber hardly have any residual load carrying capacity or progressive damage after failure is initiated and this inherent brittleness leads to sudden and catastrophic failure with almost no warning. This property prohibits their use in critical components where such sudden failure cannot be tolerated. Hence, they are limited to applications where light weight, high strength and high stiffness are much

more important than ductile material behavior and warning before failure is not critical. Another problem associated with their brittle behavior is that designers have to design components with very high safety factors because they know that structures which pass a visual inspection may still fracture at much lower loads than expected with no prior failure indications. This counteracts the advantages associated with their low density leading to heavier and much more expensive products.

1.5 Hybridization - a possible solution to brittle failure in Carbon fiber composites

Hybrid composites are systems of two or more fibers combined together in the same matrix. It is a way to counteract the demerits associated with each fiber, while at the same time retaining their useful properties, thereby creating a better product with well balanced mechanical characteristics. A hybrid composite could thus lead to a solution to the problems associated with brittle failure in Carbon fiber composites. Combining Carbon fiber with another fiber such that the resulting composite shows higher failure strain and a more ductile behavior would be highly desirable and thus vastly improve the usability of Carbon fiber composites in critical structural applications. Researchers have found that glass fibers can be used in conjunction with Carbon fibers in a polymer resin to form hybrid composites which show higher failure strain and a more ductile behavior compared to CFRP.

1.5.1 Early work on Carbon-glass Hybrid composites

Glass fibers are considerably less stiff compared to Carbon fibers with Youngs Modulus for Glass ranging from 70-90 GPa compared to over 250 GPa for the latter. But at the same time, the failure strain for Glass is almost 2-3 times that of Carbon fibers and it is also relatively inexpensive, and these are the factors which have been the driving force behind research on Carbon-Glass hybrid composites. The idea is to combine the two fibers in a polymeric resin based matrix to obtain a product which has substantial strength and stiffness from the Carbon fibers and at the same time is cheap, relatively ductile and has a higher

failure strain due to the Galss fibers. Another aspect which makes Carbon-Glass hybrids interesting is the fact that in some cases researchers have shown that the mechanical properties of the hybrid turned out better than that expected from the Rule of mixtures prediction. This phenomenon was called the Hybrid effect or synergistic effect.

In general, positive or negative hybrid effect is the positive or negative deviation of a mechanical property from the values predicted by the rule of mixtures. In some cases authors use the term 'hybrid effect' as a general term representative of a positive hybrid effect. The Hybrid effect was first reported by [25] who enhanced the failure strain of Carbon fiber by 40% with the addition of Glass fibers. According to [30], increasing Carbon content in hybrid composites led to a linear increase in fracture stress and initial modulus and the authors also observed that the failure was not catastrophic, with Glass fibers taking over the load upon failure of Carbon fibers. [7] conducted tensile tests on Carbon-glass hybrids and two different cases were discussed, one in which the layers were bonded to each other and another in which layers were separated by silicone paper (un-bonded). They showed that for the former case, the modulus was same as that predicted by the rule of mixtures until the first instance of failure in the Carbon layers. The strain at the first observed failure of Carbon was higher than that the failure strain for the Carbon layer tested individually. This was attributed to residual compressive stresses developed during manufacturing. Moreover, even after the first occurrence of failure in Carbon, it was observed that they continue to share some load. This is due to the bonding between the layers. They talked about the existence of a critical length for effective reinforcement by stiffer layers such that at a distance of the half the critical length, the load carried by the CFRP layer is same as that it would have carried had no fracture occurred. As a result of interlayer bonding, multiple fracture of CFRP layers occurred and the final failure strain was less than that of the individual glass layers. The second case, where the interlayer bonding was absent, showed an initial modulus same as that given by the rule of mixtures until the CFRP layers fractured, beyond which they ceased to share the load, which was taken up completely by the GRP layers and the

behavior of the composite was same as that of individual GRP layers. The final failure strain for the un-bonded case was same as of individual grp layers. So, even though the elastic modulus did not show a positive deviation from the rule of mixtures, a hybrid effect in terms of failure strain was apparent in the case where the layers were bonded together. In this case the final failure strain was higher than the failure strain of individual CFRP layers and more importantly, a relatively stable failure with progressive damage was apparent, compared to a sudden load drop associated with catastrophic CFRP failure in the un-bonded case.

Bader and Manders [2] discusses the enhancement of failure strain in glass shell/carbon core laminates. A hybrid effect was apparent and the increment in failure strain of the Carbon fiber was greater with lower volume fraction of Carbon and reduced thickness of the smallest continuous element in the composite. Moreover, the failure strain enhancement is more pronounced for thinner Carbon fiber layers and is virtually non existent above a certain core thickness dimension. Progressive failure of the Carbon fiber layer with multiple cracks was observed. Two theories for tensile fracture in Hybrids were identified by [44], the fiber bundle theory and the crack propagation theory. According to the former, the weakest Carbon layers, even after fracturing at their normal failure strain, keep sharing load since they are surrounded by Glass fibers. As a result of this, the stronger fibers fail at strains higher than their typical failure strains. The crack propagation theory states that the propensity of Catastrophic failure caused by sudden crack propagation in CFRP is mitigated by Glass fibers which exhibit a gradual failure process characterized by crack arrest. Thus, the probability of sudden failure is reduced in hybrids with a high percentage of glass fibers.

Harris and Bunsell [23] performed Imapact tests on Carbon/Glass hybrids, and they showed that for notched specimens, the flexural modulus and the work of fracture by impact follows the rule of mixtures. Marom et al. [35] found that the modulus, strength and K_{1c} values were almost equal to or lower than the values predicted by the rule of mixtures and the fracture energy even showed a negative hybrid effect. They explained that the fracture

energy is associated with the pull out length of each of the constituent fibers and an upper and lower bound for the fracture energy can be obtained based on the extremes of the pull out lengths. In one extreme case, the pull-out length of the glass fiber will shrink to that of the Carbon fiber leading to the lowest value of fracture energy while in the other case the pull out length of the carbon fiber will extend to that of the glass fiber leading to high fracture energies. The low values of fracture energy observed in their experiments were attributed to the fact that the close contact of the glass and Carbon layers led to a shortening of the pull-out lengths for glass fibers. Finally, they suggested that for hybrids with more segregated layers, a positive hybrid effect with respect to the fracture energy is possible if the pull out lengths of the constituent fibers increase substantially.

So, a review of the early work done on hybrids indicates that there is some discrepancy in the results reported by the authors. While some researchers indicated the presence of a positive hybrid effect, others claim that the mechanical properties simply follow the rule of mixtures or even show a negative hybrid effect. In some cases the hybrid effect is apparent only in some properties, such as the failure strain, whereas the other properties seem to follow the rule of mixtures. In general, the modulus for the hybrid composites seem to satisfy the rule of mixtures, whereas, the failure strain showed a positive hybrid effect - in the sense that its value was higher than that for the standalone Carbon fiber composites. The synergistic effect and the mechanical behavior of the hybrid depends on a lot of different aspects. Researchers have used different materials with different base fiber properties. Also, the layout of the fibers in the hybrid - interlaminated, intermingled, unidirectional alignment, multidirectional alignment etc. all have a deep role to play in how to composite behaves. In most of the cases it was observed that the failure strain and hybrid effect was higher for low volume fractions of Carbon fiber. Another advantage of using smaller amounts of Carbon fiber is that once they break, the load sharing is more gradual and the glass fibers are sufficient to take up the extra load and thus catastrophic failure is avoided. The hybrid effect is normally more pronounced for a higher dispersion or more intimately mixed fibers. The

variability in the materials used and the results obtained make it difficult to see clear trends in the mechanical behavior but a positive hybrid effect or synergistic effect is apparent in Carbon/Glass hybrid composites. Review papers such as [54], [52] and [31] give a detailed overview of the research performed in the domain of Carbon/glass hybrid composites during the earlier stages and the progress made until the 1980s.

1.5.2 State of the art in the field of Carbon-glass Hybrid composites

During the initial few years, research in the domain of Carbon/glass hybrid composites was focused on establishing a hybrid effect and settling the debate on the existence of a synergistic effect. But since then, the focus shifted to explaining failure mechanisms and the physics behind the hybrid effect and deviation from rule of mixtures behavior. Theoretical models also shifted from statistical models to ones which are more deterministic. A more fundamental understanding of the failure mechanisms have helped researchers not only establish that the hybrid effect exists, but it also enabled them to design better hybrids which had mechanical properties indicating higher effects of synergism. Another aspect patent in the recent work carried out in this domain is the effort towards design of composites which show a pseudo ductile behavior, thus preventing catastrophic failure. This is important to ensure that there is sufficient warning before final failure of structures made of hybrid composites, thus facilitating their use in more critical applications.

Swolfs et al.[57] analyzed failure development in Carbon/glass hybrid composites studied the effect of fiber dispersion on the initial failure strain. A strength model for Carbon/glass hybrid composites was developed with local load sharing assumptions. They talk about three main hypothesis used to explain the hybrid effect in composites - changes in sequences of mechanisms by which failure develops, influence of thermal residual stresses on failure and dynamic effects. The focus in this paper was only on the first hypothesis since the other two were deemed to be much less dominant [31], [45]. For a non-hybrid material, when the

weakest fiber breaks, the load is transferred to surrounding fibers through shear stresses. At a certain distance from the breaking point, the axial stresses return to the nominal value. The part where the stress has not been recovered is the ineffective length. So, the nearby fibers are subjected to stress concentrations thus making them more likely to fail. Subsequently clusters of broken fibers form which lead to further stress concentrations. Finally the cluster behaves like a large defect on reaching a critical size and the propagation of this defect finally leads to composite failure. On adding a second fiber, the failure development mechanism changes. The stress concentration and ineffective length depends on the own fiber type as well as the neighboring fiber types. The break clusters can be bridged by the unbroken fibers of the high strain material, thus leading to a delay in failure/further development of the cluster and requiring a larger break cluster size for it to become critical. Furthermore, the fact that there are lesser number of carbon fibers (since they have been replaced by glass fibers) will lead to the Carbon fibers failing at a higher strain. This paper thus explains the failure development in a hybrid which leads to a synergistic effect with respect to failure strain. They also introduce a model developed to simulate the failure of the hybrid, using a chain of bundles approach used by Rosen [50]. The model was used to study the effect of hybrid volume fraction and dispersion on the failure strain and other mechanical properties of the composite. In general, the hybrid effect increased for higher volume fractions of Glass fibers. When arranged in bundles of fibers (instead of layer by layer arrangement), increased dispersion (or smaller bundles) leads to higher hybrid effect and delayed break cluster development. Also, for the same volume fraction of fibers, a layer by layer arrangement gave better hybrid effect than random arrangement or the the case where the fibers are aligned in bundles and this phenomenon was explained based on how cluster development occurs in a hybrid composite. The paper deals with the failure mechanisms leading to the propagation of the first critical cluster, and it does not delve into fiber fragmentation, delamination or any other phenomenon that may occur after the first critical cluster propagates. Even though the model can be improved further with a Local Load sharing model as opposed to the Very local lead sharing model, this paper throws light on the

failure development in hybrid composites and goes a long way in explaining the hybrid effect.

Swolfs et al.[56] uses a Global load sharing (GLS) model to conduct a parametric study on the hybrid effect in Carbon/glass hybrids. Previously, Zweben[66] had claimed that the ratio of the failure strains of the constituent fibers in a hybrid play a major role in deciding the hybrid effect, whereas, on the contrary, Fukuda[18] suggested that the failure strain ratios barely affect the hybrid effect. To, investigate this matter, [56] used the Global load sharing model and found that the failure strain ratio does play a role, but it is not as critical as predicted by Zweben[66]. A more accurate local load sharing model could show that the failure strain effect is less pronounced than Zweben's prediction but more that the GLS prediction. The effect of the fiber strength scatter was also studied and they claimed that the strength scatter of the Carbon fibers were critical to the hybrid effect but that of the glass fibers did not play a major role. Other than that, the authors observed that higher volume fractions of the high elongation fiber led to increased hybrid effects, falling in line with previous literature, and the tensile strength follows the bi-linear rule of mixtures for the most part and starts deviating at higher Glass fiber volume fractions.

Jalalvand et al.[27] introduced an FEA based modeling approach to study the damage process in Unidirectional hybrid composites. The damage process was analysed beyond initial failure of the Low elongation component and mechanisms such as carbon fragmentation, delamination and final glass fiber failure were studied. They studied different layup configurations and carbon/glass fiber ratios and how they affect failure development. The analysis was depicted in the form of charts - damage mode maps, associating the damage mode with the absolute and relative thickness of carbon layers. The same authors improved on the FEA based modeling scheme to develop an analytical method to study damage in hybrids [28]. The paper highlights the four situations that follow first crack initiation in the Carbon layer

-

1. Premature failure of the Glass fibers

2. Sudden and rapid delamination leading to Glass layer fracture

3. Multiple fractures (fragmentation) in the Low strain layers followed by Glass layer fracture

4. Fragmentation in the carbon fiber layers followed by dispersed delamination before high strain material failure

Carbon layer fragmentation followed by delamination is highly preferred because it leads to a stress strain curve with minimum load drop and a highly pseudo ductile and smooth failure. Mathematical equations representing stresses required for the damage modes - Fragmentation in low strain material, Delmination and Failure in high strain material, were derived. Using these equations, the magnitude of stress required for each damage mode can be computed for a particular configuration or layup. Based on the order in which the stress values can be achieved, the analytical model can be used for obtain the stress strain curve and damage development for different hybrid configurations. The analytical model is a faster and more efficient alternative to the FEA based method discussed in the previous paper. The analytical model discussed here was applied to conduct a parametric study on the failure mechanisms for different configurations[29]. Damage mode maps were proposed and a major conclusion was that the highest pseudo-ductile strains can be obtained when the damage modes in the hybrids occur at stress values close to each other. This can be achieved for configurations lying close to the intersections of the boundaries in the damage mode maps. Also, increasing the stiffness and strength of the low strain material improves the pseudo-ductile strain and yield stress values. The analysis and the damage mode maps discussed in these papers will not only help us gain a better insight into the damage mechanisms after initial failure of the Low strain component, but will also help us play with different configurations and carry out parametric studies to setup accurate design guidelines and come up with much more efficient

hybrid configurations suited to structural requirements.

As mentioned previously, in the recent past, researchers have focused their attention on designing better hybrid composites which show increased hybrid effect and pseudo ductile failure profiles. Improvement in hybrid characteristics have been achieved by a number of researchers. Swolfs at al. [58] used a strength model with a fully random dispersion of Low Elongation and high elongation fibers. The model was applied to conduct a parametric study on the effects of the Low Elongation fiber strength scatter, failure ratio and high elongation fiber stiffness. They found that a large scatter in Low Elongation fiber strength corresponding ot a low Weibull modulus leads to earlier cluster development, thus facilitating the delay of this development by fiber hybridization. A high failure strain ratio (above 2 in the present case) was found to be beneficial. Also, greater stiffness of High Elongation fiber components reduces stress concentration in the Low elongation fibers. A global load sharing analysis was used in [47] to design hybrids which has better stiffness, strength and pull-out stress compared to a high elongation fiber with same failure strain. This was achieved by hybridizing the high elongation fibers with small to moderate volume fractions of the low elongation stiffer fibers. Czél et al. [14] demonstrated pseudo ductility in Carbon/glass hybrids using thin ply carbon prepregs. The main idea behind their work was to ensure stable pullout after initial cracking of the Low elongation carbon fiber layer. They used a fracture mechanics based criterion to ensure this, where the strain energy release rate (GII_c) for pull out of the inter facial layer on either side has to be less than the delamination fracture energy. Satisfying this criterion ensures that unstable pull out or delamination is avoided. Another criterion that needs to be satisfied is that the thickness of the glass layers should be able to take up the residual load after fracture of the Carbon layer. Ensuring that the above criteria are met, the authors validated their hypothesis through experiments where they showed that keeping the Carbon layers below a certain thickness - decided by the Mode II energy release rate (Fracture toughness) of the interface, it is possible to achieve pseudo ductile failure characterized by stable pull out and carbon layer fragmentation leading to a smooth non-linear

stress strain curve. The transition is the thickness beyond which the energy release rate on fracture of carbon exceeds the Mode II fracture toughness. The value of the transition thickness predicted from theoretical calculations almost matched the experimental observations, thus further corroborating the hypothesis. Another alternative to using thin carbon fiber plies is to use discontinuous Carbon layers or platelets between continuous layers of Glass fibers [12]. The condition requiring the Mode II energy release rate to be less than the interfacial fracture toughness is relaxed because stable delamination can initiate prior to Carbon layer fracture. To ensure stable pull-out occurs prior to platelet fracture, the hybrid needs to be designed to release enugh energy to initiate stable delamination of the Carbon/epoxy platelets at a lower over stress than their fracture stress. This is done by making sure that the energy release rate at Carbon fracture higher than the Mode II fracture toughness of the interface. The glass layers should be thick enough to be able to take up the load shed by broken Carbon fibers. Ensuring the fulfillment of these criteria, the authors experimentally demonstrated that it is possible to design composites which show pseudo ductile failure with smooth transitions between elastic and plateau regimes and favorable stress strain response. The modulus and plateau stress for each of the hybrid configurations were predicted accurately and there was good correlation between the modeled stress strain responses and their experimental counterparts. The advantage of using discontinuous Carbon fibers over thin ply carbon layers is that it relaxes the thickness restrictions, thus allowing a higher volume fraction of Carbon fibers, leading to an increase in initial hybrid modulus and plateau stress. The analysis techniques and design methodology using the damage mode maps discussed in [28] and [29] were applied to design actual composite hybrids with the configurations showing favorable pseudo ductile behavior characterized by stable pull-out and Carbon layer fragmentation, thus validating the analytical model discussed previously.

From recent literature, it is apparent that substantial progress has been made towards development of pseudo ductile composites and hybrids which show enhanced synergistic effect in their mechanical properties. Wisnom [62] gives an account of the various mechanisms

used to obatin composites showing pseudo ductile behavior. Swolfs[55] is one of the most recent review papers in the domain of hybrid polymer composites and gives a comprehensive overview of the progress made in this field in the recent past.

(a) Ski poles (source: www.massdrop.com)

(b) Skateboard deck (source: www.julicarbonfiber.com)

(c) Tennis racket (source:www.wilson.com)

(d) Golf club (source: www.outdoorlifex.com)

(e) Bike wheel (source: www.bikes2udirect.com)

Figure 1.4: Applications of Carbon fibers and CFRP in sports

(a) The Airbus A350 XWB is 53 percent composite by weight

(b) The Boeing 787 is almost 50 percent composite by weight

(c) The Eurofighter contains substantial amount of composite materials in its structural design

Figure 1.5: Applications of Composite materials in the Aerospace industry

(a) McLaren MP4 12C

(b) Lamborghini LP 670 SV

Figure 1.6: High end sports cars which use significant amounts of CFRP

Chapter 2

COMPUTATIONAL MODELING

2.1 Different types of Fracture behavior: Brittle, Ductile and quasi-brittle materials

The distinction between different types of material behavior is often based on factors such strain to failure, amount of plastic deformation or energy absorbed during fracture. High plastic deformation, and high strain to failure are associated with ductile behavior whereas materials which fail at relatively low strains and do not show much plastic deformation are said to be brittle. While the use of such definitions for ductile and brittle materials are not completely incorrect, a more accurate representation of the fracture behavior of different materials can be made using the Fracture Process Zone (FPZ).

The non-linear zone in front of the crack tip can be divided into two parts: the Plastic Zone (PZ) and the Fracture Process Zone (FPZ). The PZ can involve hardening plasticity - where the stress increases with increase in strain, or perfect plasticity - where the stress remains constant with increasing strain. The FPZ exhibits damage and is characterized by softening - decrease in stress with increasing deformation. The relative sizes of these non-linear zones with respect to each other and the structure as a whole decides the type of fracture behavior and materials can thus be classified as:

1. **Brittle** - The PZ and the FPZ are both very small compared to the dimensions of the structure. These materials thus have a very small non-linear zone and their fracture behavior can be explained with reasonable accuracy using the principles of Linear Elastic Fracture Mechanics(LEFM). Materials such as glass, brittle ceramic and plexiglass fall in this category.

2. **Ductile** - For these type of materials, the non-linear zone size is not negligible but most of the non-linearity is accounted for by the PZ. The FPZ is still negligibly small compared to the PZ as well as the overall structure. The fracture of ductile materials can be characterized using Elastic Plastic Fracture Mechanics. Examples of such materials include stainless steel, silver and most ductile metals.

3. **Quasi-brittle** - Quasi-brittle materials also have a non-linear zone which is not negligible compared to the size of the structure but most of it is occupied by the FPZ. Strain softening mechanisms such as microcracking, void formation, interface breakages, slips, crystallographic transformation (ceramics), debonding and pullout (composites) lead to a substantial FPZ size. The PZ is negligible due to lack of perfect yielding or hardening and this may lead to a sudden transition from damage to elastic response. Materials such as concrete, ice, rock, composites and nano-composites show quasi-brittle behavior. Size effect plays a major role for the fracture behavior of such materials and a structure which shows quasi-brittle properties for one size may show significant brittleness when on being substantially scaled up.

Fig. 2.1 shows a schematic representation of the zones in front of the crack tip and the different types of fracture behavior. It should be noted that in some cases, the PZ as well as the FPZ are both significant in size compared to the structure and in such cases it is difficult to make a clear distinction between ductile and quasi-brittle behavior.

2.2 Size Effect studies

The dependence of the nominal strength of a structure on the structural size is called Size Effect. A size effect study, with reference to quasi brittle materials, involves testing of samples across different dimensions and studying the effect of scaling on the mechanical and fracture behavior. Fig. 2.2 shows a typical size effect plot for a quasi brittle material where the peak

nominal stress (σ_N) obtained from experiments are plotted against the sample width (D) on a logarithmic scale. The characteristic size chosen (width in the present case) can be any major structural dimension that scales across the different sized specimens. For lower values of D (smaller samples) the points are expected to lie near or along the straight horizontal line indicating the strength limit. The failure behavior for structures of this size are governed by strength based criteria. For large sized samples, the points should lie close to the straight line inclined at 45° in Fig. 2.2 indicating the Linear Elastic Fracture Mechanics (LEFM) limit. In these cases the failure behavior can be predicted using LEFM. Structural sizes which happen to be between the two extremities will lead to points on the size effect curve which will not lie very close to any of the two red dotted lines indicated in Fig. 2.2 but they will be a part of the transition zone. The location of points on the size effect curve can be related to the extent of devlopment of the FPZ. The points lying close to the strength limit line. On the other hand points lying close to the LEFM limit indicate that the structural sizes are large enough for the FPZ to develop completely, thus diminishing the effect of the FPZ on the failure stress and making it possible to predict fracture behavior using LEFM.

2.3 Cohesive Zone Modeling

The Cohesive Zone Model (CZM) is a phenomenological model which is used to simulate fracture in a wide variety of materials. Cohesive Zone Modeling is a very powerful numerical technique which has gained substantial popularity over the last few decades with the advancement of Finite Element Analysis (FEA) and non-linear fracture mechanics. Its ability to incorporate non-linear fracture behavior, applicability to a wide range of materials and relative ease of implementation has lead to its favorability. This approach developed from the works of Dugdale [16] who proposed the Strip Yield Model and Barenblatt [3]. Further development occurred through the work of various researchers such as Hillerborg [26] who introduced the concept of a fictitious crack model and discussed to possibility of cohesive cracks appearing anywhere even in the absence of a pre-crack, Needleman [42], Tvergaard [60] among others.

The Cohesive Zone (CZ) approach regards fracture as a gradual phenomenon where the separation between two imaginary surfaces increases as the crack develops. The cohesive zone is this extended virtual crack and the separation of these surfaces is resisted by the presence of cohesive traction forces. This extension of the crack tip is a numerical definition and is not detectable by physical instruments. Another difference between the cohesive crack and a conventional crack is that the pair of cohesive surfaces can transmit forces among themselves whereas actual crack surfaces are generally traction free. The cohesive forces start acting on the surfaces only on the application of external load. Initially, the cohesive tractions increase with increasing distance between the virtual crack surfaces, until it reaches a peak value. Beyond the peak value, softening ensues and the traction gradually goes down to zero. The instant at which cohesive forces become zero, the virtual surfaces are said to have separated completely and this stage is associated with the formation of an actual microscopic crack at the location. In other words, at any given time, the last location at which the surface tractions have diminished to zero is associated with the crack tip.

The decay of the cohesive forces beyond the peak is governed by a cohesive law (also known as a Traction Separation Law), which relates the traction forces to the separation between the cohesive surfaces. In the most common approach towards obtaining the traction separation law for the fracture of a given material/ structure/ interface, we start with an assumed relation between the forces and separation for the cohesive zone and cohesive parameters are treated as modeling constants. These modeling constants are calculated by running cohesive zone simulations and matching these simulations to experimental data. Thus the cohesive zone shape and the cohesive parameters are obtained through an iterative process. The cohesive zone shape can take various forms depending on the type of material and the micro-mechanics of the fracture process. Needleman [42] used a cubic polynomial function to represent the normal interaction for the process of void nucleation in metal matrices. Xu and Needleman [64] used an exponential cohesive law in a study of void nucle-

ation at matrix-particle interface. Tvergaard and Hutchinson [60] studied interface fracture in elastic-plastic solids using a trapezoidal traction-separation law. Camacho and Ortiz [9] used a linear softening model to study impact in brittle materials. Espinosa and Zavattieri [17] used a bi-linear cohesive law in their study of polycrystalline brittle materials. Fig. 2.3d shows some typical cohesive law shapes.

The parameters of the cohesive law depend on a number of factors such as the function chosen to represent the traction-separation relation, the micro-mechanics involved in the fracture process, the type of material.etc. These parameters are not necessarily material properties but they depend on the particular modeling situation. While the number of fitting parameters may depend on the individual fracture problem being modeled and the cohesive law shape, some parameters are generally present in any situation and are key to describe the Cohesive Zone Model. They are - Cohesive strength (peak value of the traction-separation curve), the cohesive energy (area under the traction-separation curve) and a characteristic length of the separation of the virtual surfaces.

The advantages of using cohesive zone modeling include the ability to model complex softening behavior with relative ease and handle non-linear fracture effects. This modeling scheme is self-sufficient in that no other fracture criteria is necessary to describe the fracture behavior. It is capable of non only dealing with fracture toughness and initiation of fracture, but it can describe the entire progressive fracture process ahead of the crack tip, including crack propagation. It removes the singularity associated with the crack tip and represents the physics of the fracture process. Another key benefit of using this technique over conventional fracture analysis methods is that it eliminates the requirement of the presence of an initial crack. The validity of this technique has been verified through countless works by various researchers for studying a wide range of materials such as metals, polymers, concrete, ceramics, composites. etc. It has successfully represented various fracture processes such as void growth and nucleation, interface fracture, delamination, dynamic crack growth, frag-

mentation, fiber bridging, creep and even fatigue. The ability to represent such a wide range of fracture processes, its applicability to a large variety of materials and its relative ease of implementation makes the Cohesive Zone Modeling approach a very powerful simulation tool.

2.4 Damage modeling and implementation of Cohesive zone simulations using the in-built Cohesive zone modeling features in ABAQUS

Modeling damage involved characterizing the softening portion of the traction separation law i.e. the portion beyond the peak stress in the cohesive zone curve. A bi-linear cohesive zone shape was chosen for the present work.

2.4.1 Derivation of damage parameter

This section describes the derivation of the expression of the Damage parameter (D) for a bi-linear cohesive law. The bi-liner cohesive law involves the following modeling parameters:

1. **Elastic modulus(E)** - Elastic modulus of the material, represented by the slope of the initial rising linear portion(line AB in Fig. 2.4) of the curve.

2. **Cohesive strength (σ_y)** - Peak value of the cohesive curve and can be considered to have the same value as the yield strength of the material.

3. **Cohesive Energy (GF)** - This is the Fracture energy or Fracture toughness of the material and is given by the area under the entire cohesive law curve. It signifies energy dissipated during the fracture process. In Fig. 2.4 it is given by the sum of the area of the triangles ABE and ECD.

4. **Initial fracture energy (Gf)** - As seen in Fig. 2.4 it is the area of the blue triangle ABE. Point E is obtained by extending BC to the horizontal axis and Gf signifies the fracture energy corresponding to a material which follows a linear cohesive law given by ABE.

5. **Kink point** - The kink point is represented by C in Fig. 2.4 and is the location in the traction-separation curve where the transition occurs from the first linear arm (BC) to the second one (CD)

6. **Characteristic length (l_c)** - The separation between the virtual crack surfaces in the cohesive zone.

7. **Knock down factor (k_d)** - The ratio of the stress at kink point to the cohesive strength. It is generally less than one and with reference to FIg. 2.4, $k_d = \frac{\sigma_k}{\sigma_y}$.

Fig. 2.4 shows a bi-linear traction separation law. The normalized separation on the horizontal axis can be approximated to the strain of the cohesive element and the vertical axis represents the stress experienced by the element. In the initial portion of the traction-separation law, line AB represents nothing but the linear elastic behavior of the cohesive element, thus the slope of the line is the Elastic Modulus (E) of the material. Once the peak stress (σ_y) is reached at point B, softening starts. The corresponding strain at B is given by ε_y. BC represents the first linear portion of the softening curve and the cohesive curve transitions into the second linear portion CD at point C. C is called the kink point and has coordinates ε_k and σ_k. The last point in the traction-separation curve D has coordinates ε_2 and 0. The area under the entire curve represented by the sum of the area of the blue triangle ABE and red triangle ECD is the Fracture Energy GF.

The cohesive zone modeling features in the material properties of ABAQUS allows direct implementation of linear or exponential softening, but bi-linear softening (or any other form of softening) needs to be modeled by supplying data points for the Damage vs displacement plot in a tabular form which corresponds to the bi-linear softening curve. The Damage vs displacement plot is a graphical representation of how the Damage parameter varies as a function of the displacement or deformation at the cohesive zone strip. The derivation of the expressions for the Damage-displacement relation is presented next.

The parameters which act as inputs to the problem or simulation (thus considered known for the purpose of derivation) are E, σ_y, k_d, G_F and $\frac{G_f}{G_F}$. For simulation purposes we preferred to use ratios k_d and $\frac{G_f}{G_F}$ as the set of known parameters but essentially it means that the quantities G_f and σ_k are known through these ratios.

In Fig. 2.4 the equation for line AB is given by,

$$\sigma = E\varepsilon \tag{2.1}$$

Line BC is given by,

$$\sigma - \sigma_y = \frac{\sigma_k - \sigma_y}{\varepsilon_k - \frac{\sigma_y}{E}}(\varepsilon - \frac{\sigma_y}{E}) \tag{2.2}$$

Here, ε_y was replaced with $\frac{\sigma_y}{E}$.

Line CD is given by,

$$\sigma = \frac{\sigma_k}{\varepsilon_k - \varepsilon_2}(\varepsilon - \varepsilon_2) \tag{2.3}$$

We need the intersection of line BC with the ε axis and this is obtained by setting $\sigma = 0$ in Eq. 2.2. This leads to,

$$\varepsilon_1 = \frac{\sigma_y\varepsilon_k - \frac{\sigma_y^2}{E}}{\sigma_y - \sigma_k} + \varepsilon_y \tag{2.4}$$

Now, we use the fact that the area of the triangle ABE is equal to G_f. So,

$$Gf = \frac{1}{2}\varepsilon_1\sigma_y \tag{2.5}$$

Using Eq. 2.5 and Eq. 2.4, we obtain an expression for ε_k in terms of the other known quantities.

$$\varepsilon_k = \frac{\sigma_k \sigma_y^2 + 2EG_f\sigma_y - 2EG_f\sigma_k}{E\sigma_y^2} \tag{2.6}$$

Point F is the intersection of a line dropped vertically downward from B and the horizontal axis. Now, the sum of the areas of triangles ABF,FBC and FCD is equal to the total area under the curve which is nothing but G_F. So, we have

$$G_F = \frac{1}{2}\frac{\sigma_y^2}{E} + \frac{1}{2}\sigma_y(\varepsilon_k - \frac{\sigma_y}{E}) + \frac{1}{2}\sigma_k(\varepsilon_2 - \frac{\sigma_y}{E}) \tag{2.7}$$

Using the expression for ε_k from Eq. 2.6 and the above expression for G_F, we obtain

$$\varepsilon_2 = \frac{2(G_F + \frac{\varepsilon_y\sigma_k}{2} - \frac{\sigma_y(\varepsilon_k - \varepsilon_y)}{2} - \frac{\sigma_y^2}{2E})}{\sigma_k} \tag{2.8}$$

Now, the Damage parameter D is represented by the general Eq. 2.9 for any given portion of the traction-separation curve.

$$\sigma = (1 - D)E\varepsilon \tag{2.9}$$

Comparing the above expression with the equation of the respective lines AB, BC and CD we obtain the damage parameter expressions for the three different sections of the cohesive zone curve.

So, comparing Eq. 2.9 with Eq. 2.1 gives us

$$D = 0 \tag{2.10}$$

for line AB. Comparing Eq. 2.9 with Eq. 2.2, we get the following expression for the Damager parameter D along BC,

$$D = \frac{E\varepsilon + (\frac{\sigma_y - \sigma_k}{\varepsilon_k - \frac{\sigma_y}{E}})(\varepsilon - \varepsilon_y) - \sigma_y}{E\varepsilon} \tag{2.11}$$

Similarly, for line CD, Eq. 2.9 was compared with Eq. 2.3 which leads to

$$D = \frac{E\varepsilon + (\frac{\sigma_k}{\varepsilon_2 - \varepsilon_k})(\varepsilon - \varepsilon_2)}{E\varepsilon} \tag{2.12}$$

The above expressions were incorporated into a MATLAB subroutine which can be used to plot Damage-displacement curves and obtain the corresponding data points which can be used for bi-linear cohesive modeling in ABAQUS.

2.4.2 Verification of MATLAB subroutine and ABAQUS bi-linear model

Before using the Cohesive zone modeling technique, it was important to verify proper implementation of the MATLAB subroutine used to obtain damage-displacement data and ensure that the results from the ABAQUS CZ simulation performed using this data falls in line with what is expected. A typical bi-linear Cohesive zone shape was chosen for this process. The parameters used were: $G_F = 100N/mm, G_f\{G_F = 2, k_d = 0.8, E = 70000MPa, \sigma_y = 500MPaandl_c = 0.1mm$. After generating damage-displacement data for these parameters, the ABAQUS simulation was performed for a single element model. The important simulation details are provided in 2.1.

Fig. 2.6 shows the damage-displacement plot obtained using the MATLAB subroutine for the CZ parameters mentioned. Fig. 2.7 shows that the stress-strain plot obtained for the cohesive element from the ABAQUS simulation matches exactly with the actual cohesive law curve. The energy under the stress-strain curve was found to be $995.91N/mm^2$ corresponding to a Fracture energy value of $99.591N/mm$ when $l_c = 0.1mm$ is taken into consideration. Thus the fracture energy is with 0.5% of the expected value of $100N/mm$. Thus, the MATLAB subroutine and the implementation of the bi-linear cohesive law for ABAQUS simulations has been verified.

Element dimensions	0.1 by 0.1 mm
Part type	2D planer, deformable shell
Elastic material properties	E=70000 MPa, G1=G2=26900 MPa
Density	1.25 e-07 ton/mm^3
Maxs damage inputs (CZ material)	Nominal stress=500MPa
Damage evolution properties	Type:displacement, softening:tabular (damage displacement data was entered in a tabular form in this section)
Section	Section type: cohesive, response:traction separation, initial thickness=0.1 (has to be same as l_c), out of plane thickness=1
Mesh	quad structured
Element type	Linear explicit Cohesive - COH2D4: A 4-node two-dimensional cohesive element
Step	dynamic explicit(Explicit solver was used), non-linear geometry ON
Field output history request	Stress, logarithmic strain, displacement, forces we requested for 200 intervals
History output requests	ALLIE (Internal energy), ALLKE (kinetic energy) and ALLSE (strain energy) were requested
Boundary conditions	refer to Fig. 2.5

Table 2.1: Modeling details for 1 element CZ simulation

2.5 Computational size effect studies using bi-linear cohesive law

The fracture toughness calculation of a wide variety of materials such as metals, polymers and nano-composites is currently governed by the protocols mentioned in ASTM 5045-99 [15]. But it should be noted that the standards are applicable to brittle and ductile only and were developed assuming LEFM to be valid in general. [38] demonstrated that the this standard approach for measuring fracture toughness is not applicable to graphene nano-composites. Moreover, it has been shown by researchers that it is necessary to incorporate a non-linear Cohesive Crack law to capture the fracturing behavior of quasi-brittle materials accurately [63], [49], [10]. A bi-linear cohesive law shape is one of the viable options and is applicable to concrete and other quasi-brittle materials.

Bažant's Size Effect Law first introduced in 1984 [4] gives an efficient way of obtaining the fracture toughness as described in [5]for materials which show quasi-brittle behavior and size effect. But, if a bi-linear cohesive behavior needs to be represented, a more accurate expression is necessary, and this work is an effort towards filling that gap. This project aims to develop a technique to obtain better estimates of the various bi-linear cohesive law parameters and obtain the complete bi-linear cohesive law shape, which will be instrumental in advanced modeling applications such as crash modeling of composites and scaling in nano-composites. In general, this study intends to provide protocols for better damage tolerant design of quasi-brittle structures over a wide range of length scales.

This computational study involved the following phases:

1. Obtaining a group of dimensionless parameters to model bi-linear cohesive law

2. Development of accurate modeling capability to simulate size effect in fracture using bi-linear cohesive law

3. Size effect studies in parametric space - Obtaining fitting equation for specific modeling parameters and verifying asymptotic behavior

4. Conducting parametric study and developing master curve of fitting equations

The following sections elaborate on the details of the work done in each phase.

2.5.1 Obtaining a group of dimensionless parameters to model bi-linear cohesive law

In order to develop a modeling tool which can possibly serve as a design protocol, it is important to ensure that the techniques are applicable to a wide range of situations. Dimensionless analysis is an efficient technique which was used in the present work to obtain a group of dimensionless cohesive law parameters which can be used to demonstrate the applicability of the modeling techniques for a wide range of structures of different dimensions, loading configurations and mechanical properties.

We start with a set of parameters which can used to describe the structure and the bi-linear cohesive law. They are - $\sigma_y, G_F, G_f, \sigma_k, \sigma_N, E, a, D, l, t$. Here all the symbols have their usual meanings and t is the sample thickness. Also, it should be noted that the first four parameters are related to the cohesive law, last four represent the structural dimensions and the other two involve the mechanical properties of the material. The thickness 't' can be ignored as since it is much smaller than the major dimensions of the specimen. So, we have nine parameters to work with. We use the Buckingham theorem for the dimensional analysis and choose force [F] and length [L] as our fundamental physical quantities and G_F and D as our fundamental variables or parameters. Expressing the other seven parameters in terms of the fundamental variables we have,

$$\pi_1 = \sigma_N G_F^{\alpha} D^{\beta} = \frac{\sigma_N D}{G_F} \tag{2.13a}$$

$$\pi_2 = \sigma_y G_F^{\alpha} D^{\beta} = \frac{\sigma_y D}{G_F} \tag{2.13b}$$

$$\pi_3 = G_f G_F^{\alpha} D^{\beta} = \frac{G_f}{G_F} \tag{2.13c}$$

$$\pi_4 = \sigma_k G_F^{\alpha} D^{\beta} = \frac{\sigma_k D}{G_F} \tag{2.13d}$$

$$\pi_5 = E G_F^{\alpha} D^{\beta} = \frac{E D}{G_F} \tag{2.13e}$$

$$\pi_6 = a G_F^{\alpha} D^{\beta} = \frac{a}{D} \tag{2.13f}$$

$$\pi_7 = l G_F^{\alpha} D^{\beta} = \frac{l}{D} \tag{2.13g}$$

$$\tag{2.13h}$$

Now, we introduce g_α as the normalized energy release rate, l_{ch} as Hillerborg's characteristic length, $g(\alpha)^{'}$ as the first derivative of $g(\alpha)$ with respect to α, X as the dimensionless measure of specimen size and Y as the dimensionless measure of strength.

$$g(\alpha) = \frac{G(\alpha) E}{D \sigma_N^2} \tag{2.14}$$

$$l_{ch} = \frac{E G_F}{\sigma_y^2} \tag{2.15}$$

$$X = \frac{g_\alpha D}{g_\alpha^{'} l_{ch}} \tag{2.16}$$

$$Y = \frac{(\frac{\sigma_y}{\sigma_N})^2}{g(\alpha)^{'}} \tag{2.17}$$

Now we re-arrange some terms to obtain

$$\pi_1^{'} = \frac{\pi_2^2}{\pi_1^2 g(\alpha)'} = \frac{\sigma_y}{\sigma_N})^2 \frac{1}{g(\alpha)'} = Y \tag{2.18a}$$

$$\pi_2^{'} = \frac{\pi_2}{\pi_5} = \frac{\sigma_y}{E} \tag{2.18b}$$

$$\pi_4^{'} = \frac{\pi_4}{\pi_2} = \frac{\sigma_k}{\sigma_y} = k_d \tag{2.18c}$$

$$\pi_5^{'} = \frac{\pi_2^2}{\pi_5} \frac{g(\alpha)}{g(\alpha)'} = \frac{D}{l_{ch}} \frac{g(\alpha)}{g(\alpha)'} = X \tag{2.18d}$$

$$\tag{2.18e}$$

We can express $\pi_1^{'} = Y$ as a function of the other six parameters giving us

$$Y = f(\frac{a}{D}, \frac{l}{D}, X, k_d, \frac{G_f}{G_F}, \frac{\sigma_y}{E}) \tag{2.19}$$

In general, for most quasi-brittle materials, $\sigma_y << E$ and this allows us to neglect the dependence of Y on the last parameter in the above expression. Also, since we scale all the major specimen dimensions in our size effect studies, we ignore the first two parameters in the expression for Y. These simplifying assumptions were made to reduce the number of variables we need to work with, thus reducing the complexity of the problem. So, we finally have,

$$Y = f(X, k_d, \frac{G_f}{G_F}) \tag{2.20}$$

Eq. 2.20 is the fundamental starting point for parametric studies using bi-linear cohesive zone simulation studies.

2.5.2 Development of accurate modeling capability to simulate size effect in fracture using bi-linear cohesive law

This section describes a computational study where the size effect was investigated for two different bi-linear cohesive law shapes. The two shapes considered were : convex with param-

eters $G_F = 100N/mm, fracG_fG_F = 2, k_d = 0.8, E = 70000GPa, \sigma_y = 1200MPaandl_c = 0.05mm$, and concave with parameters $G_F = 100N/mm, fracG_fG_F = 0.5, k_d = 0.2, E = 70000GPa, \sigma_y = 1200MPaandl_c = 0.05mm$. The cohesive law shapes for these parameters are shown in Fig. 2.8. The details of a typical simulation is provided next.

The basic framework of the simulation involves modeling a SENT specimen which is loaded under displacement control until the cohesive surfaces are fully separated throughout their length leading to complete fracture of the sample. There were two parts in the model - the main SENT sample part and a rigid tab part, whose central reference point was used to obtain reaction forces. The model was partitioned into different sections to make the meshing easier and facilitate assignment of different section properties and elements for each partition. A uniform mesh was used in front of the crack tip and for larger sizes, a biased mesh was used beyond the uniform mesh region to reduce computation time. The uniform mesh region spanned at-least the length of the estimated Fracture Process Zone obtained using Irwin's characteristic length (l_{ch}) given by Eq. 2.21 and for the material properties chosen, it was obtained to be $4.86mm$. It was important to ensure at-least 50 elements along the estimated FPZ length for high accuracy results. Fig. 2.11 shows a typical mesh obtained for the present model and Fig. 2.12 shows a zoomed in view of the mesh in the Cohsive zone in front of the crack tip. The tab part was attached to the main SENT part using a constraint in the assembly. The modeling details for a typical simulation is shown in Table. 2.2.

$$l_{ch} = \frac{EG_F}{\sigma_y^2} \tag{2.21}$$

The modeling process was validated by performing various checks to ensure the accuracy of results. The time period of simulation was brought to an order of magnitude such that further increase in time period led to no significant improvement in accuracy. Using too small a time period led to significant oscillations in the output data and it is important

Part type	main SENT -2D planer, deformable shell; tab - 2d planar, discrete rigid, wire
Elastic material properties	E=70000 MPa, Poisson's ratio = 0.3
Density	1.6 e-06 ton/mm^3
Maxs damage inputs (CZ material)	Nominal stress=1200MPa
Damage evolution properties	Type:displacement, softening:tabular (damage displacement data was entered in a tabular form in this section)
Section	Section type: Refer to Fig. 2.10. Section A - cohesive, response:traction separation, initial thickness=0.05 (has to be same as l_c), out of plane thickness=1 ; Section B,C,D,E - Elastic section with out of plane thickness=1
Mesh	Refer to Fig. 2.10. Section A- quad structured ; Section - B,C,D,C - quad dominated, free, advancing front
Element type	Refer to Fig. 2.10. SectionA - Linear explicit Cohesive - COH2D4: A 4-node two-dimensional cohesive element; Section B,C,D,E - Linear explicit plane strain: CPE4R: A 4-node bilinear plane strain quadrilateral, reduced integration, hourglass control.
Step	dynamic explicit(Explicit solver was used), non-linear geometry ON
Field output history request	Stress, logarithmic strain, displacement, forces we requested for 200 intervals
History output requests	ALLIE (Internal energy), ALLKE (kinetic energy) and ALLSE (strain energy) were requested
Boundary conditions	refer to Fig. 2.13

Table 2.2: Modeling details for SENT CZ simulation

to use a time period which leads to smooth curves but at the same time does not take an unreasonable time to execute. The mesh dependence was also studied and it was ensured that the mesh was dense enough to obtain consistent results. The displacement at the end of the tab also affected the accuracy of results. A displacement too large may lead to very few data points till the point of final failure for the various field variables and a small displacement may prevent final failure from occurring. Thus, the various simulation parameters were optimized to obtain a model which could be solved within a reasonable time and still yielded accurate results.

For a typical simulation, Fig. 2.14 shows the first cohesive element next to the crack tip and the stress strain curve for this element was compared to the actual cohesive law in Fig. 2.15. We see a perfect match between these curves thus verifying proper implementation of the CZ modeling technique. Fig. 2.16 shows the development of reaction forces at the tab with time and Fig. 2.17 shows how the different forms of energy vary with simulation time. The reaction force reaches its peak value with minimal oscillations in the plot and shows a clear peak value. This is desirable and is a result of optimizing various simulation parameters as described in the previous paragraph. Also from Fig. 2.17, we see that up until the approximately 0.7 seconds, the kinetic energy is negligibly small compared to the internal energy and strain energy of the structure. This shows that the simulation was very stable till the peak value of reaction was reached and thus further validates our choice of simulation parameters.

Cohesive zone simulations were thus performed on a wide range of SENT samples where the sample width (D), length (l) and crack length (a) was scaled across the different sized samples. The dimensions of the range of SENT models are shown in Table. 2.3. Each model was simulated using both convex and concave Cohesive Law shapes.

The results are shown in Table. 2.5 abd Table. 2.4 for the concave and convex cohesive law shapes respectively. The peak force was obtained from the reaction vs simulation time

Width (mm)	length (mm)	crack length (mm)
0.25	1	0.125
0.5	2	0.25
1	4	0.5
5	20	2.5
10	40	5
20	80	10
50	200	25
100	400	50
200	800	100
500	2000	250

Table 2.3: Dimensions of the range of SENT simulations

plot (similar to the one shown in Fig. 2.16) for each individual simulation. Fig. 2.18 compares the size effect plots for the concave and convex bi-linear cohesive shapes. When these plots are compared to a typical size effect plot for a fractured quasi-brittle material (Fig. 2.2) the typical characteristics are apparent - we see the initial portion of the plots tend to fall on a horizontal asymptote representing strength dominated failure and the points at the other extreme tend to fall on a line with a negative 45° slope representing LEFM based fracture behavior. Also, we see that the failure stress values for the extreme sizes - i.e. the smallest and the largest sized models, are very close to each other for the two different cohesive shapes. But, if we look at the failure loads for the intermediate points, there is a strong dependence on the type of cohesive law used. This can be explained based on the fact that for the largest sized models, the structure is large enough compared to the FPZ size to allow the FPZ to develop completely before complete failure occurs. Thus, the failure load does not depend on the shape of traction-separation law. For smaller sizes the FPZ develops only partially. This can be proved by noting that the cohesive stresses at peak load are different the zero.

Width (mm)	Peak force (N)	Peak nominal stress
0.25	147.805	591.22
0.5	291.526	583.052
1	566.776	566.776
5	2130.27	426.054
10	3414.07	341.407
20	5259.33	262.9665
50	8916.19	178.3238
100	13113.4	131.134
200	18460.5	92.3025
500	29363.6	58.7272

Table 2.4: Results obtained for SENT simulations using the convex cohesive law

Depending on the shape of the cohesive curve shape, the apparent fracture energy of the material (i.e. integral of the cohesive stresses as a function of the crack opening at the time of peak load) may be substantially different. For example, for the same crack mouth opening displacement, a convex cohesive law will provide generally more energy than a convex law.

2.5.3 Size effect studies in parametric space - Obtaining fitting equation for specific modeling parameters

The size effect plots shown previously can be interpreted in a parametric space to obtain generalized results which can facilitate comparison with similar size effect studies carried out on different geometry and materials with different mechanical and fracture properties. The parametric space involves X and Y coordinates where X is a normalized measure of structural size and Y is a normalized measure of failure strength. They are given by,

Width (mm)	Peak force (N)	Peak nominal stress
0.25	140.933	563.732
0.5	268.01	536.02
1	478.978	478.978
5	1575.81	315.162
10	2476.06	247.606
20	3814.01	190.7005
50	6843.27	136.8654
100	10909.7	109.097
200	16304	81.52
500	27584.5	55.169

Table 2.5: Results obtained for SENT simulations using the concave cohesive law

$$X = \frac{g_\alpha D}{g'_\alpha l_{ch}} \tag{2.22}$$

$$Y = \frac{(\frac{\sigma_y}{\sigma_N})^2}{g(\alpha)'} \tag{2.23}$$

Here, D is the sample width, l_{ch} is the Hillerborg Characteristic length, σ_y is the Yield Strength of the material, σ_N is the peak stress or failure stress for a particular structure (this is size dependent as seen previously) and $g(\alpha)$ is the dimensionless energy release rate calculated according to LEFM and is a function of α - the ratio of crack length to sample width ($\frac{a}{D}$). The first derivative of $g(\alpha)$ with respect to α is $g(\alpha)'$. Now,

$$g(\alpha) = \frac{G(\alpha)E}{D\sigma_N^2} \tag{2.24}$$

Here $G(\alpha)$ is the energy release rate. Since it is calculated according to LEFM, the J-Integral is a valid measure of energy release rate. The J-Integral can be readily obtained

from an ABAQUS simulation, the details of which are described next.

The ABAQUS model used to perform the J-Integral calculations essentially involved modeling an SENT sample similar to the ones described in the previous section, but instead of CZ modeling, the crack was incorporated as an interaction as shown in. The crack was modeled using quarter elements to capture the $\frac{1}{\sqrt{r}}$ singularity near the crack tip. Quarter elements are quadratic elements with some midside nodes located at a quarter of the edge as shown in Fig. 2.19 and the ABAQUS options used to incorporate them into a crack is shown in Fig. 2.20. Another important feature of the model is that the region around the crack tip is modeled using a sweep mesh (shown in Fig. 2.23) with with a bias (element size decreasing as we move towards the crack tip) to replicate the contours around the crack tip used to calculate J-Integral. Having a significant number of contours is important, because if it is shown that the J-Integral value converges to almost a constant value for the largest contour sizes, we can be sure that the J-Integral calculation is highly accurate and it gives us a way to validate the simulation. Other details of the simulation is shown in Table. 2.6.

$g(\alpha)$ is independent of the sample dimensions as long as the major dimensions are scaled and since we scaled all the major dimensions in the previous SENT simulations, only one set of J-Integral simulations was sufficient to obtain the $g(\alpha)$ value. In order to calculate $g(\alpha)^{'}$ we need to perform two more simulations, for α values slightly above and below the target α value for central difference calculations (Eq. 2.25). For example,if we seek the $g(\alpha)^{'}$ value at $\alpha = 0.5$, we can perform simulations for $\alpha = 0.49$ and $\alpha = 0.51$ (by simply changing the crack length used in simulations) and use the central difference method to obtain the required value of $g(\alpha)^{'}$. For the present set of simulations ($\alpha = 0.5$) we required $g(0.5)$ and $g^{'}(0.5)$. Using 20 contours in the central contour region, we obtained $g(0.5) = 4.09$ and $g^{'}(0.5) = 17.4$. Table. 2.7 shows the J-Intgeral values obtained for the 20 contours and we see very good convergence demonstrated by very close J Integral values obtained for the largest contour sizes.

Part type	main SENT -2D planer, deformable shell
Elastic material properties	E=70000 MPa, Poisson's ratio = 0.3
Density	1.6 e-06 ton/mm^3
Section	Section type: Solid homogeneous, 1mm thick
Mesh	Refer to Fig. 2.22. Quad dominated sweep mesh at central circular region and quad free advancing front mesh elsewhere
Element type	Standard quadratic plane strain - CPE8: An 8-node bi-quadratic plane strain quadrilateral
Interaction	crack (Contour integral). Refer to Fig. 2.20
Step	Static general (Implicit solver was used), non-linear geometry ON
Field output history request	Stress, logarithmic strain, displacement, forces we requested for 200 intervals
History output requests	Refer to Fig. 2.24
Boundary conditions	refer to Fig. 2.25
Loading	Uniform pressure load. refer to Fig. 2.25

Table 2.6: Modeling details for J-Integral simulation

$$g(\alpha)' = \frac{g(\alpha+\delta) - g(\alpha-\delta)}{2\delta} \tag{2.25}$$

Using the above values of $g(\alpha)'$ and $g(\alpha)$, the size effect plots in the $X-Y$ parametric space were generated for the simulations performed previously on a wide range of sizes and for both the convex and concave cohesive law shape. Other than that, a set of simulations were also performed on different SENT configurations in order to verify the validity of the modeling technique. The details of these SENT configurations is shown in Table. 2.8. The simulation labeled O1 and I1 were intended to represent behavior similar to that of concrete and the subsequent simulation parameters were obtained by changing just the Modulus and yeild strength to obtain higher X values. Increased values of X could also be obtained using specimens of higher dimensions but it increases computation time significantly. Simply scaling up the stiffness and strength decreases one of the denominators in the expression for X (l_{ch}) and provides an elegant way of achieving higher X values without significant increase in computation time. It should be ensured that the mesh density in front of the crack tip is changed to account for the change in l_{ch} since it is necessary to always have 50 or more elements withing the span of l_{ch}.

A similar size effect study involving a concave bi-linear cohesive crack law with $GF/G_f = 2$ and $k_d = 0.25$ was performed in [11] and the results are shown in Fig. 2.26. The authors demonstrate that the size effect curves can be related to Bažant's Size effect law and for larger X values (Fig. 2.26a), the size effect curves for different loading configurations tend to asymptotes given by $Y = X + c$ where c ranges from 2.21 to 2.56 with the average value of 2.31. In an average sense, the asymptotes are represented by the line $SEL - G_F$ in the figure. For lower values of X it was seen that the points tend to an asymptote with a higher slope given by $Y = (G_f/G_f)X + 0.44 = 2X + 0.44$. Simulations performed using a linear Cohesive crack law showed that the points tend to $Y = X + 0.44$ for higher X values. So, we see that the intercept on the vertical axis for the asymptote related to the initial points of the

Contour number	J-Integral value (N/mm)
1	3.341
2	3.501
3	3.535
4	3.554
5	3.566
6	3.574
7	3.581
8	3.586
9	3.59
10	3.594
11	3.597
12	3.6
13	3.602
14	3.605
15	3.607
16	3.608
17	3.61
18	3.612
19	3.613
20	3.614

Table 2.7: J Integral values obtained for the 20 contours

Label	D (mm)	l (mm)	a (mm)	E(GPa)	σ_y (MPa)	kd	gf/GF	GF(N/mm)
O1	200	800	100	40	4	0.8	2	0.0125
O2	100	400	50	400	40	0.8	2	0.0125
O3	100	400	50	800	80	0.8	2	0.0125
I1	200	800	100	40	4	0.2	0.5	0.0125
I2	100	400	50	400	40	0.2	0.5	0.0125
I3	100	400	50	800	80	0.2	0.5	0.0125

Table 2.8: Details of the other SENT configurations molded

size effect curve obtained using the bi-linear concave cohesive crack law and the asymptote representing the linear cohesive crack law has the same value, i.e. 0.44 and in both these cases the slope is equal to G_F/G_f (since $G_F = G_f$ for a linear cohesive law $G_F/G_f = 1$ and the slope is also equal to 1).

Now, we take a look at the curves obtained for the present simulations. The results of all these simulations in the $X - Y$ parametric space is shown in Fig. 2.27 and Fig. 2.28. If we consider the linear fit of the data points obtained for the convex cohesive crack law (Fig. 2.27), we see that the size effect curve tends to an asymptote given by $Y = X + 0.05$. For the concave cohesive law, for higher values of X, the curve is asymptotic to the line given by $Y = X + 2.4$. On investigating the behavior for the initial portion of the size effect curve related to concave cohesive shape, we see that the data points corresponding to lower X values tend to fall in line with $Y = 2X + 0.3$. Thus, we see that for both cohesive law shapes, data points for higher X tend to follow asymptotes with unity slope and for the concave cohesive shape, the intercept of 2.4 falls in the 2.21 to 2.56 range reported by the authors in [11]. For lower X values, the slope is $G_F/G_f = 2$ same as what was observed in [11].

So we see that the behavior for the size effect curves obtained for the present set of simulations is similar to the results obtained by [11]. From these findings, we can infer that the initial part of the size effect curve of a bi-linear cohesive crack law with a concave shape depends mainly on the initial fracture energy G_f. As we move towards higher X values we see the effects of the total fracture energy G_F which leads to the curve changing its slope until it reaches a point where the data points fall in line with an asymptote of unity slope. The behavior for a convex cohesive law is not much different other than the fact that for even low values of X, the data points tend to follow the linear fit line.

The various simulations discussed hitherto were conducted to develop a robust simulation algorithm. The various checks performed on the simulations, such as matching the stress-strain curves for the cohesive elements with the actual cohesive law, ensuring mesh independence, demonstrating the smoothness of the reaction-time curves, ensuring that the kinetic energy is very small compared to the strain energy. etc. serves to support the accuracy and validity of the simulation techniques developed. The fact that the size effect curves show similar behavior to a previous computational study conducted in this domain further validates the simulation methodology used in this project.

2.5.4 Conducting parametric study and developing master curve of fitting equations

Once the validity of the simulation technique was ensured, parametric studies were conducted to obtain results for a range of the values of the three dimensionless parameters seen in Eq. 2.20 - $X, k_d, G_f/G_F$. Fig. 2.30, Fig. 2.31 and Fig. 2.32 shows some typical plots obtained during this parametric study with $k_d = 0.25$, $k_d = 0.5$ and $k_d = 0.75$. $\sigma_y/E = 0.02$ for all three cases and G_f/G_F was varied from $0.3to1$ for all cases thus representing the concave cohesive law shape. We see that the curves behave similar to the size effect plots mentioned previously in that they all show the transition from a high initial slope for lower X values to a line of unity slope for higher values of X.

Parametric curves such as these were used to obtain fitting equations which capture not only the initial and final asymptotes but give a very good approximation of the entire size effect curve for a given set of cohesive parameters. A Non-Linear least square fitting method was used in MATLAB to carry out the curve fitting operation. The general fitting equation used was

$$Y(X) = \left(\frac{1}{1-1/\beta^m}\right)^{1/m} \psi(X) \left\{1 + \left[\frac{\psi(X)}{\chi(X)}\right]^m \left(\frac{1}{1-1/\beta^m}\right)\right\}^{-1/m} \tag{2.26}$$

where,

$$\psi(X) = \frac{G_F}{G_f} X + \frac{1 + 0.44a\sqrt{G_F/G_f X}}{9(1-\alpha)^4 g'(\alpha) + a\sqrt{G_F/G_f X}} \tag{2.27}$$

$$\chi(X) = X + \frac{1 + \xi a\sqrt{X}}{9(1-\alpha)^4 g'(\alpha)/\beta + a\sqrt{X}} \tag{2.28}$$

For the above set of equations, ξ is the Y intercept for the asymptote obtained for the portion containing higher values of X. For the fitting, the following should be ensured: $m \geq 1$, $a \geq 0$ and $\beta > 1$. The above set of equations were obtained by incorporating the fact that the initial part of the size effect curve has a slope equal to G_F/G_f and the final slope is equal to unity. For specific set of cohesive law parameters, we obtain the values of the unknowns a, β, m, ζ. Fig. 2.33 shows a typical fitting curve obtained using the above technique. For $k_d = 0.25$ and $\sigma_y/E = 0.02$ and $G_f/G_F = 0.3$ the values of the fitting parameters were : $a = 5.9706, \beta = 1.1001, m = 4.2956, \xi = 5.1897$. It is observed that the fitting equation is quite accurate and it even captures the change in curvature during the initial portion of the size effect plot for lower values of X. The Root mean square value was obtained to be 1.0000 (upto 4 decimal places) which corroborates the accuracy of the fitting technique.

Fitting curves such as these can be obtained for any given set of cohesive parameters. The cohesive parameters can be obtained by curve fitting experimental data. Once we have

the fitting equation, it becomes very easy to predict failure loads for a given configuration. Say we obtain the X value for a given structural dimension and configuration. Using the fitting equation, we get the corresponding value of Y. Now Y is related to σ_N and so we can obtain the failure load provided all other quantities related to the structural configuration are known (which is usually the case). This shows the utility of the overall modeling technique and the wide range of situations to which it is applicable makes it a very powerful tool.

2.6 *Obtaining $g(\alpha)$ and $g(\alpha)'$ values using CZ modeling and comparison with J-Integral*

This section discusses an alternative way of calculating the normalized energy release rate ($g(\alpha)$) and its derivative ($g(\alpha)'$). This method models the crack using CZ modeling as described in Section. 2.5 and we make use of an alternate definition of energy release rate, which after using the central difference formula for the derivative take the form shown in Eq. 2.29. Here P is the load applied and b is the thickness. This equation can be used to calculate energy released when the load is kept constant. In order to implement this using CZ modeling in ABAQUS, instead of displacement control loading, the load was applied as a pressure on the sample edge. U was taken as the maximum value of internal strain energy for a given simulation. So, in order to obtain the energy release rate for crack size a, it was necessary to perform two more simulations for crack sizes, $a + \delta$ and $a - \delta$. Once G was calculated using Eq.2.29, $g(\alpha)$ was calculated using Eq.2.24 and ($g(\alpha)'$) was obtained using Eq.2.25. The primary objective of this set of simulations was to compare the $g(\alpha)$ and ($g(\alpha)'$) values obtained using CZ modeling with that obtained using the J-Integral technique discussed previously. So, simulations were performed on a $100mm$ by $400mm$ SENT sample with crack sizes ranging from $40mm$ to $60mm$ with increments in steps of $0.5mm$. Thus these simulation covered $\alpha = 0.4$ to $\alpha = 0.6$. Two sets of simulations were performed for this size range - one set used the CZ modeling technique and the other set used the J-Integral to obtain energy release rate.

Fig. 2.34 compared the results obtained using the two different modeling techniques. From Fig. 2.34a and Fig. 2.34b we can say that there is very good agreement between the results obtained from these two techniques. But when we observe the comparison of the $g(\alpha)^{'}$ results from these techniques, we see some discrepancy. Moreover, there is significant scatter in the values obtained using the CZ modeling technique.

$$G(P,a) = \frac{1}{b}\left[\frac{U(P,a+\delta a) - U(P,a-\delta a)}{2a}\right]_P \tag{2.29}$$

2.7 Cohesive Zone modeling VUMAT

The ABAQUS implementation of MATLAB runs into problems when used to run simulations on 3-D structures featuring layered configurations. Cohesive zone modeling in layered configurations is important to model advanced fracture mechanics simulations such as the cohesive zone modeling of composite laminates. In order to tackle this problem a VUMAT (Virtual User Material for Explicit ABAQUS simulations) was developed. It uses a bi-linear cohesive law and incorporates the concept of damage introduced in Sec. 2.4. This VUMAT has been attached in the Appendix.

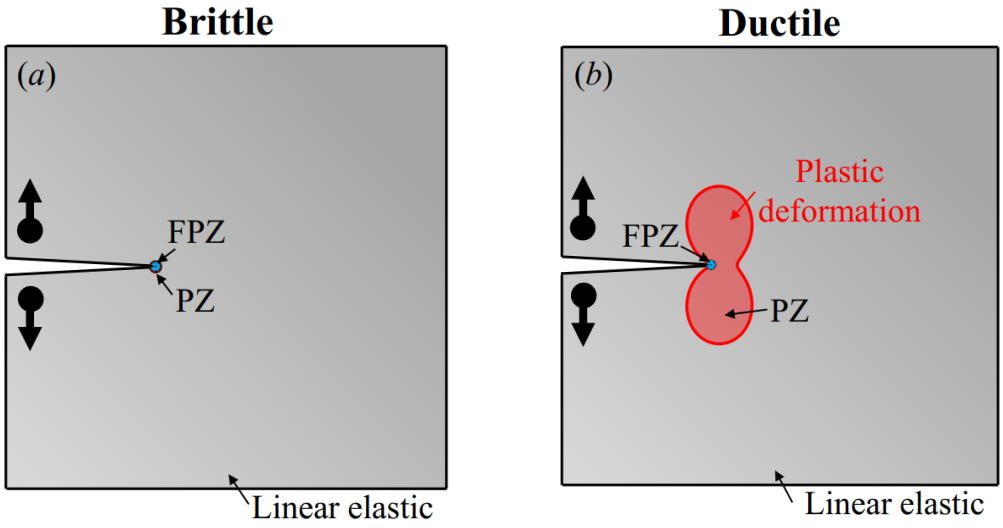

(a) Brittle

(b) Ductile

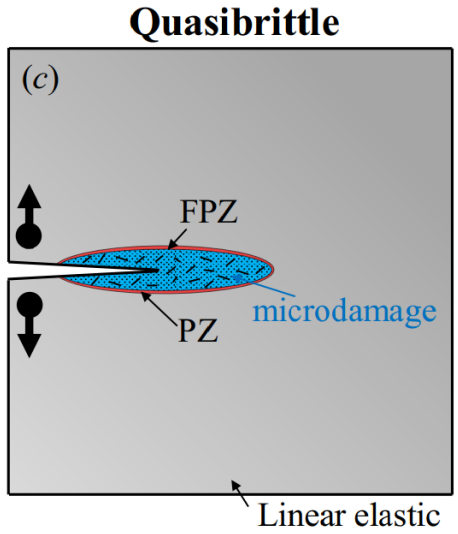

(c) Quasi-brittle

Figure 2.1: Different types of fracture behavior

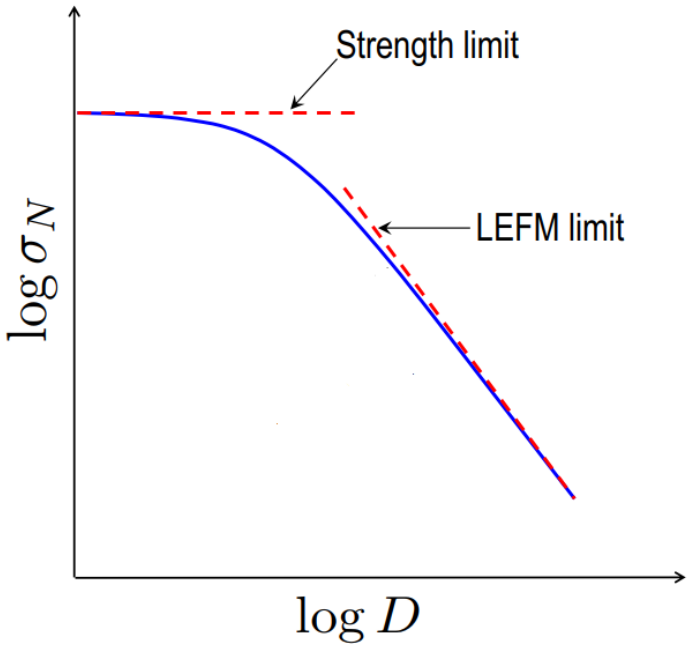

Figure 2.2: Typical size effect behavior for a quasi brittle material

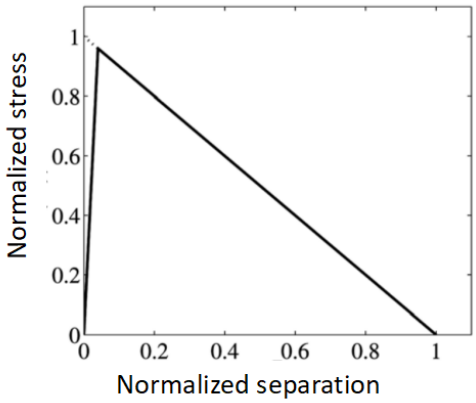

(a) Linear

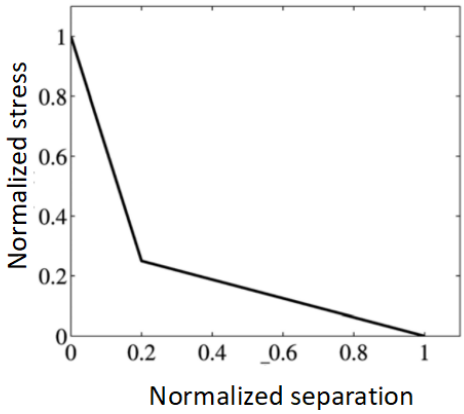

(b) Bi-linear

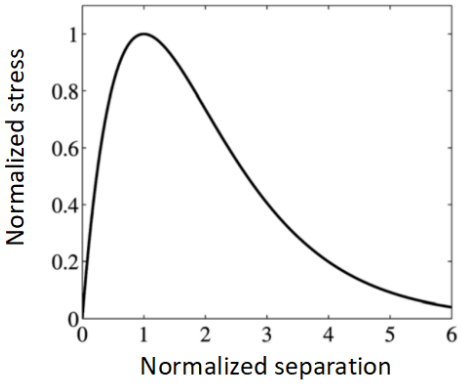

(c) Exponential

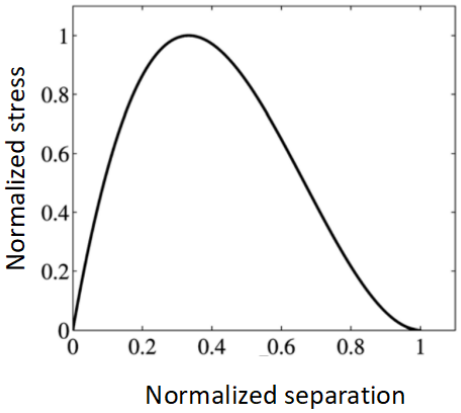

(d) Polynomial

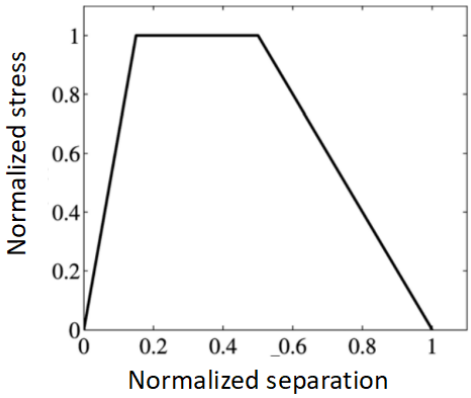

(e) Trapezoidal

Figure 2.3: Different types of cohesive law shapes

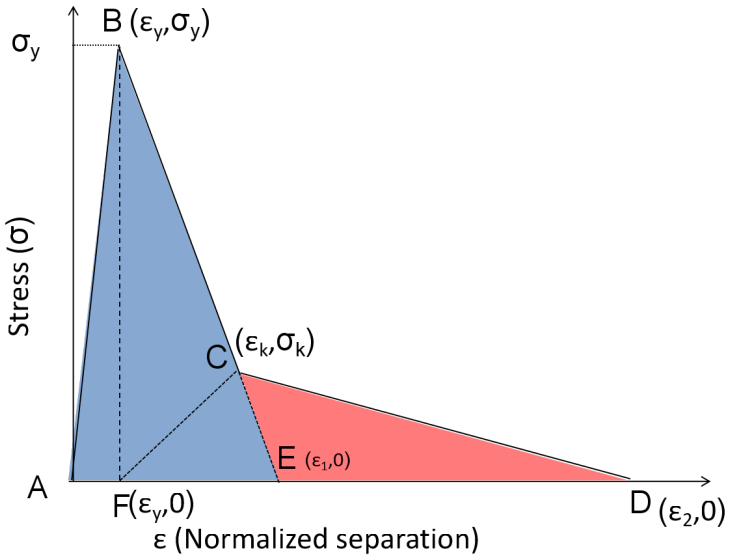

Figure 2.4: Bi-linear cohesive law

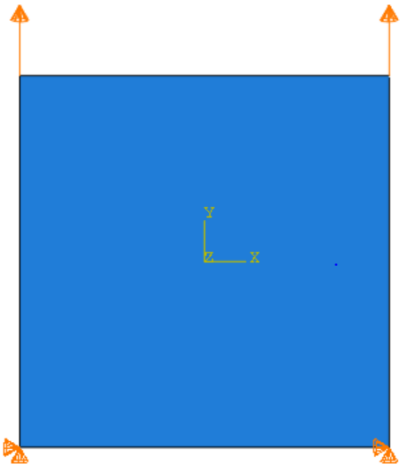

Figure 2.5: Boundary conditions for 1 element cohesive zone simulations - Bottom two nodes nodes were fixed and displacement was applied to the top two nodes using an amplitude definition

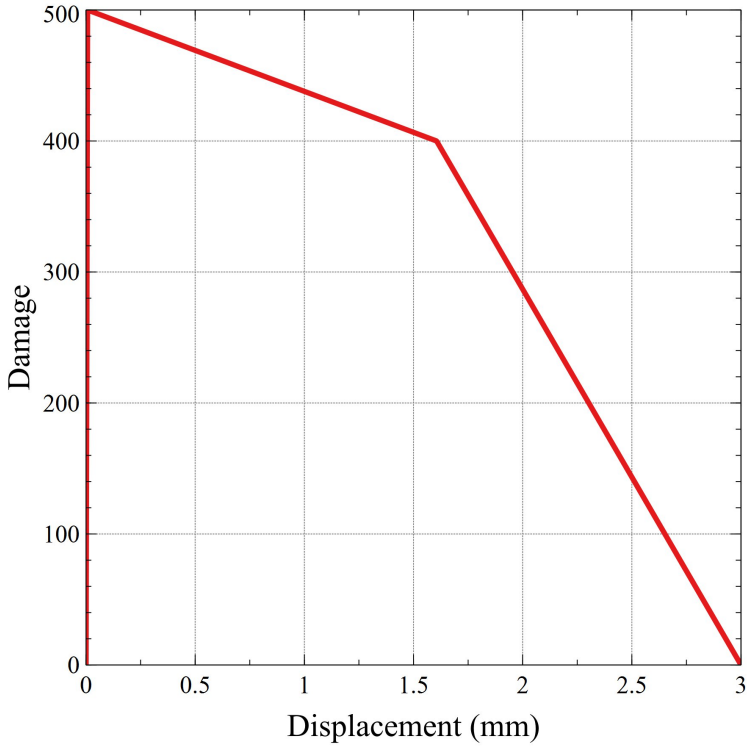

Figure 2.6: Damage parameter-deformation plot used for single element simulation

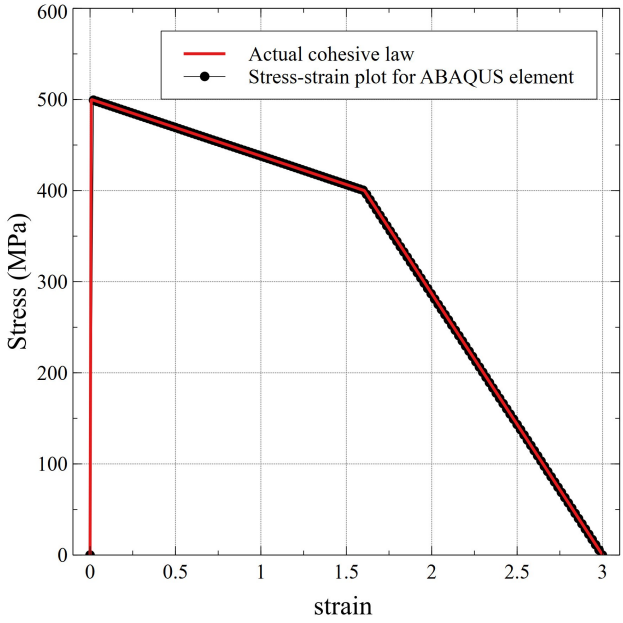

Figure 2.7: Comparison of actual cohesive law curve with stress-strain curve obtained from ABAQUS simulation

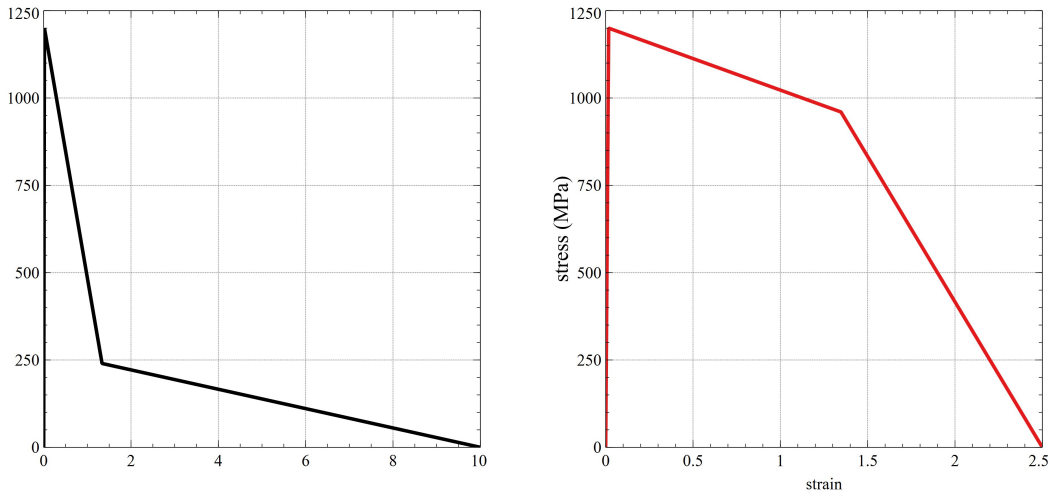

(a) Concave

(b) Convex

Figure 2.8: Cohesive law shapes used for SENT simulations

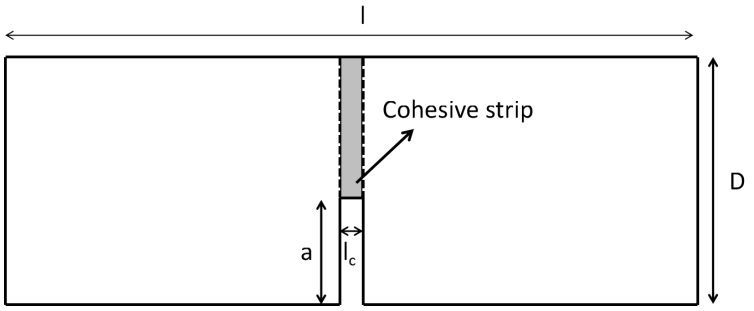

Figure 2.9: Schematic of the SENT model

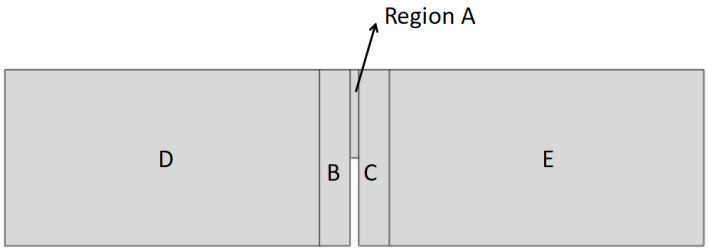

Figure 2.10: Partitions used in modeling SENT samples

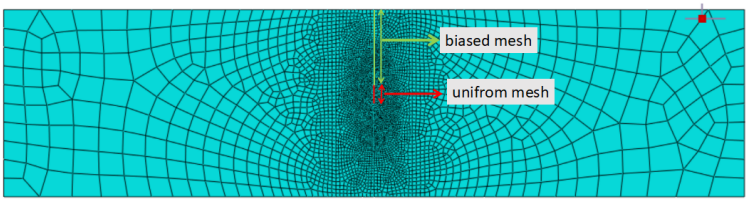

Figure 2.11: Partitions used in modeling SENT samples

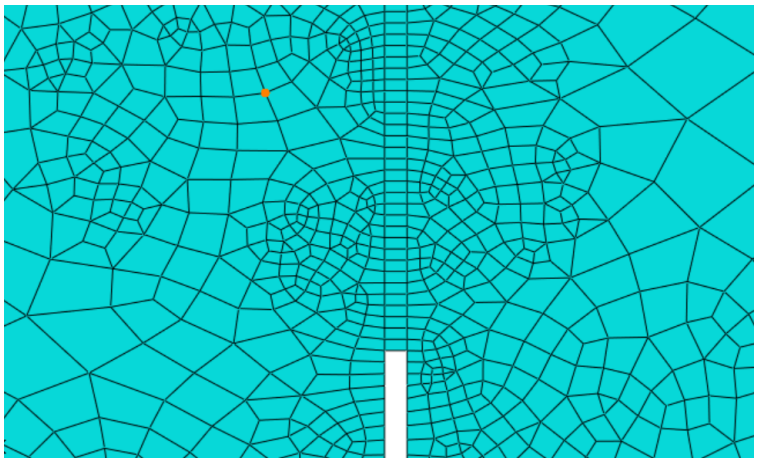

Figure 2.12: Partitions used in modeling SENT samples

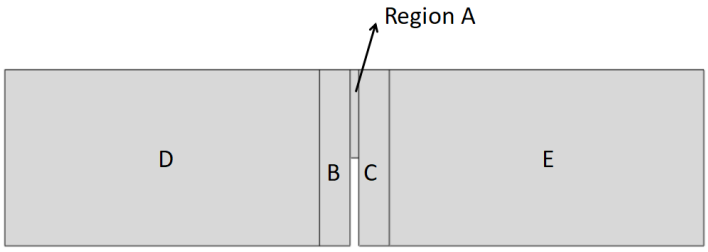

Figure 2.13: Partitions used in modeling SENT samples

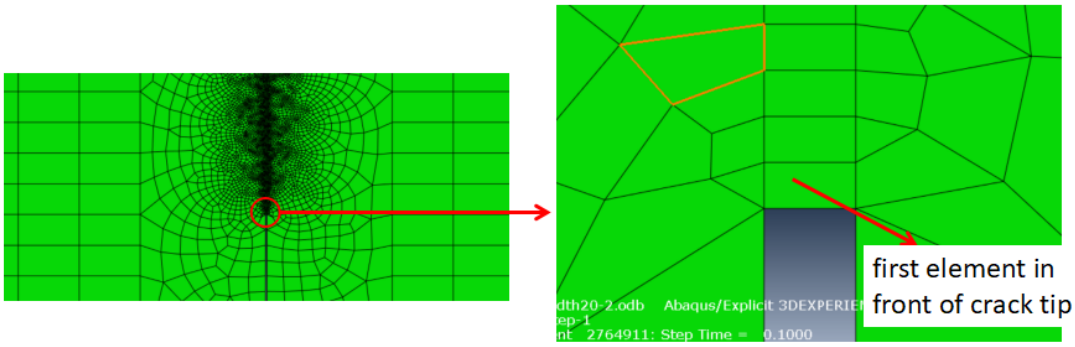

Figure 2.14: First element in front of the crack tip

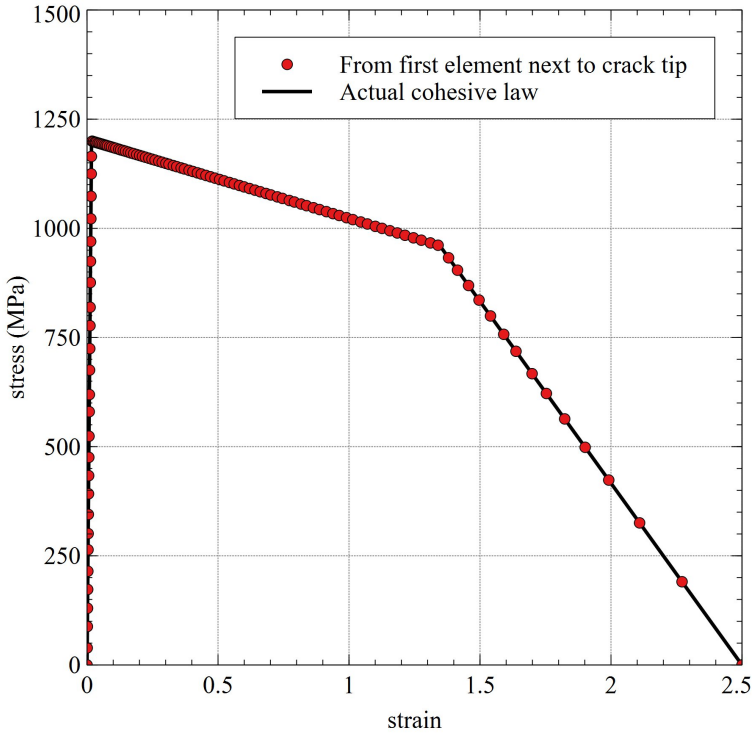

Figure 2.15: Stress-strain plot for first element in front of the crack tip

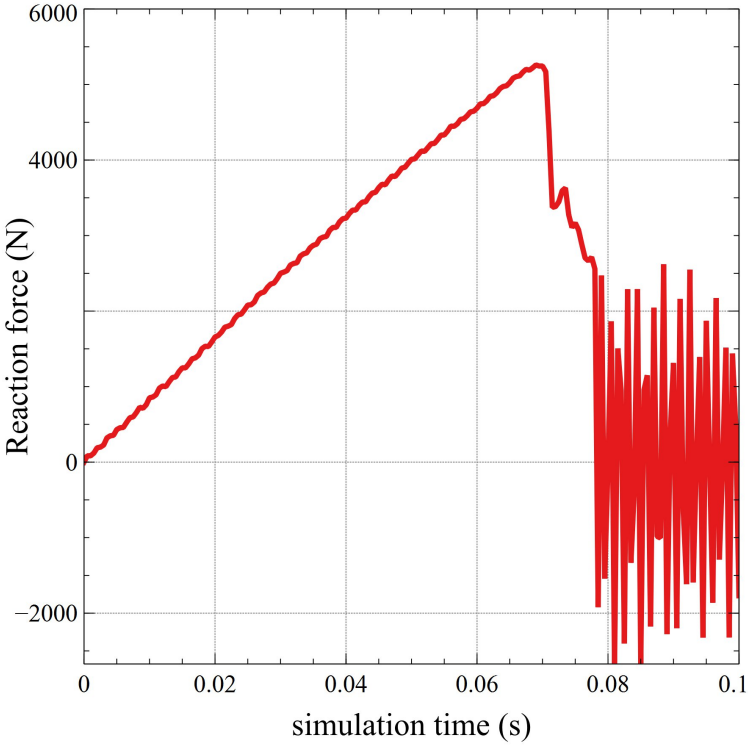

Figure 2.16: Plot showing the reaction at the tab as a function of simulation time

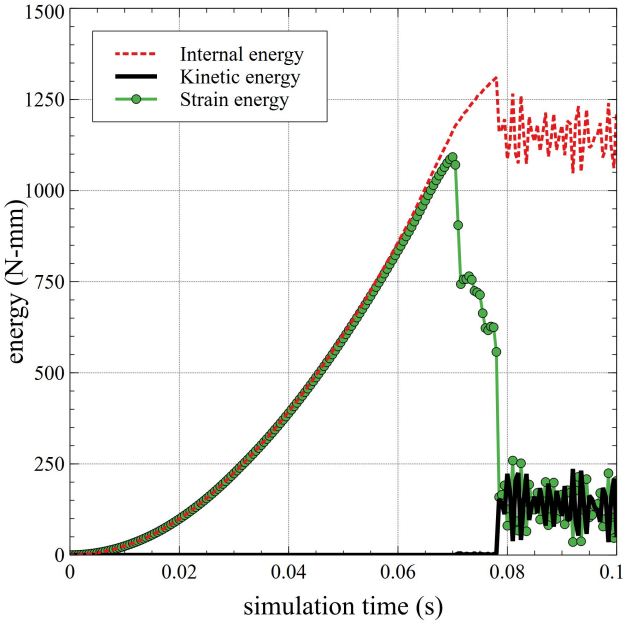

Figure 2.17: Variation of energy with simulation time

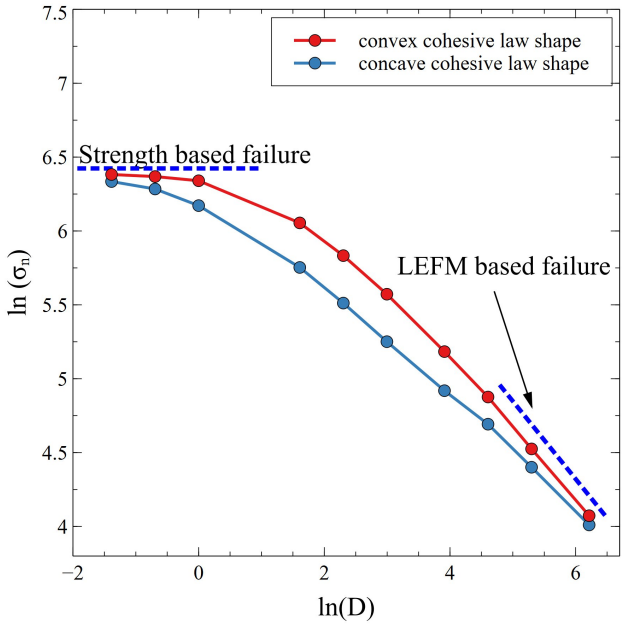

Figure 2.18: Size effect plot comparing the concave and convex cohesive law shapes

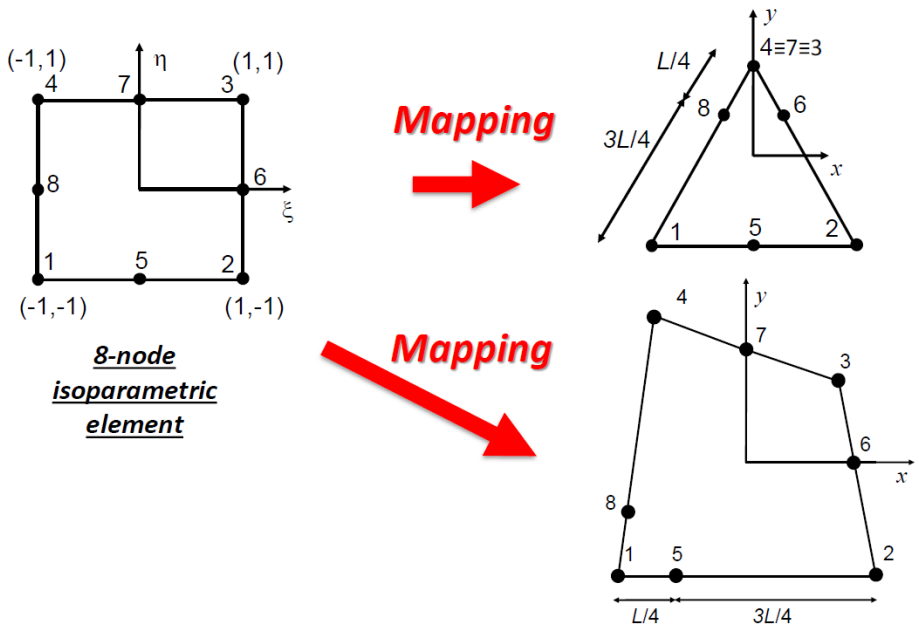

Figure 2.19: Quarter element

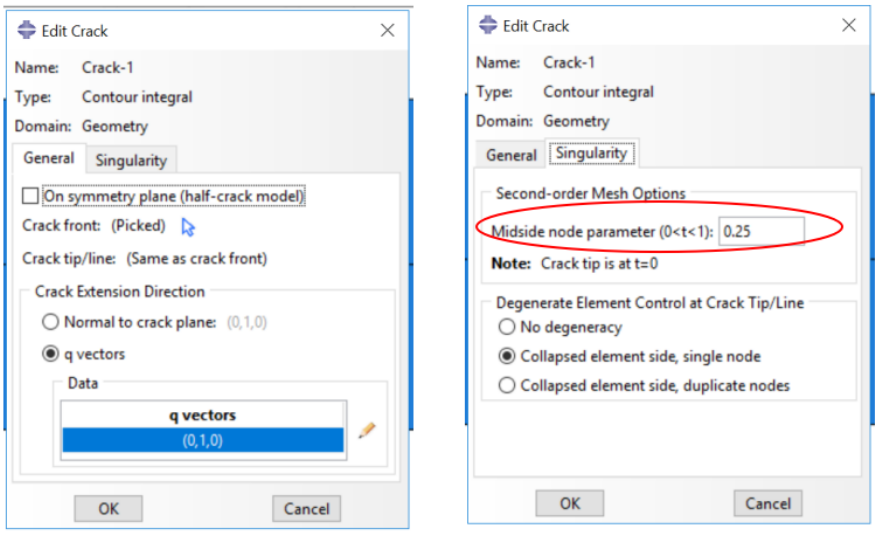

Figure 2.20: Options used to set up the crack in ABAQUS. The midside node parameter settings are used to create the quarter elements

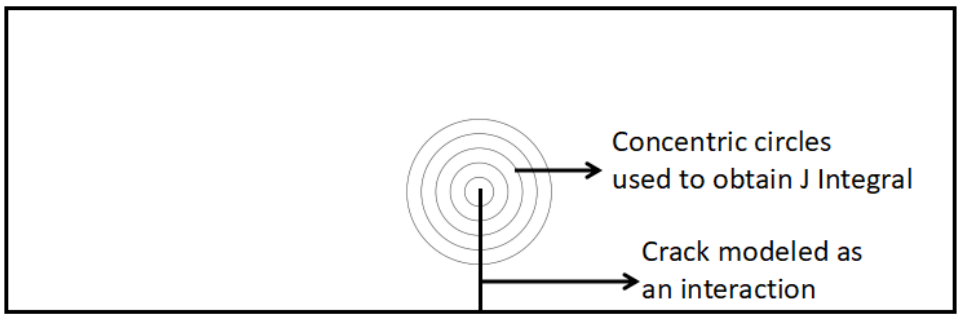

Figure 2.21: Schematic of the SENT model used for ABAQUS simulations used to obtain J-Integral

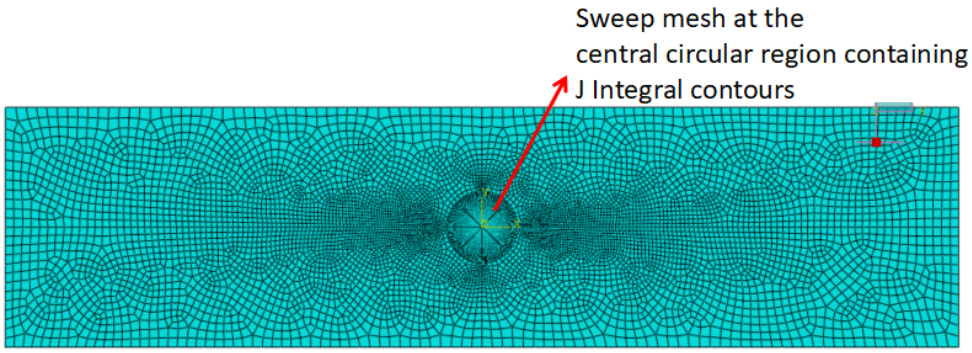

Figure 2.22: Mesh used in a typical J-Integral simulation

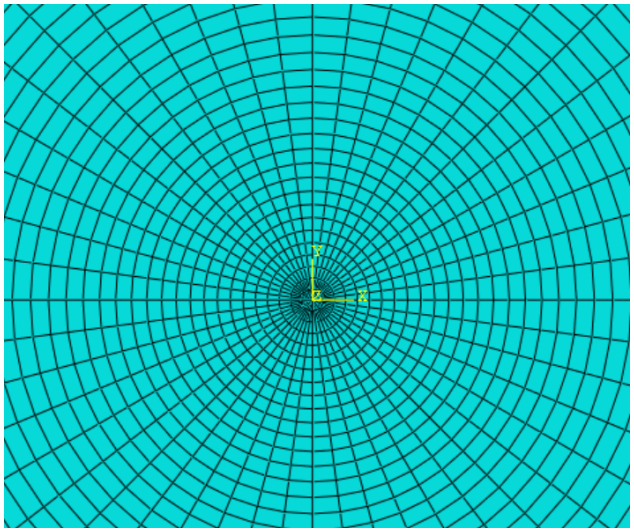

Figure 2.23: Zoomed in view of sweep mesh used in the central circular region around crack tip

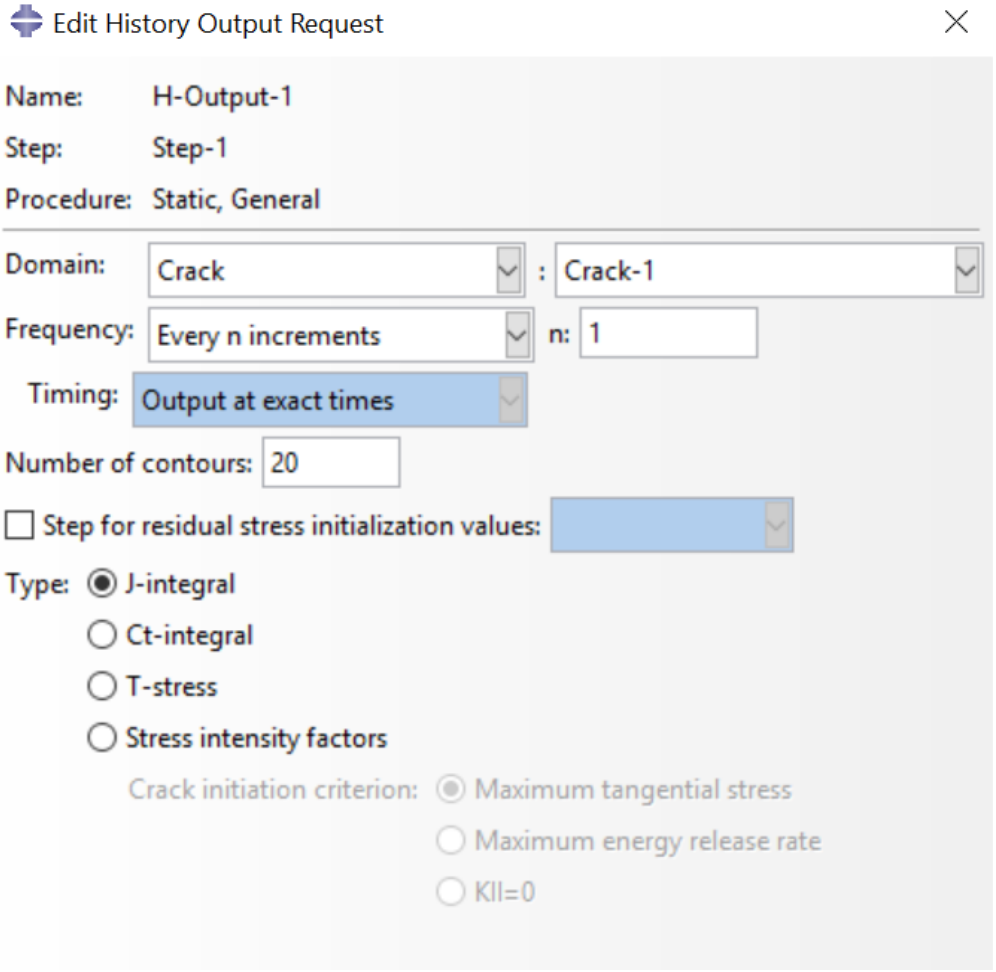

Figure 2.24: History output options used - J Integral will be calculated over 20 contours

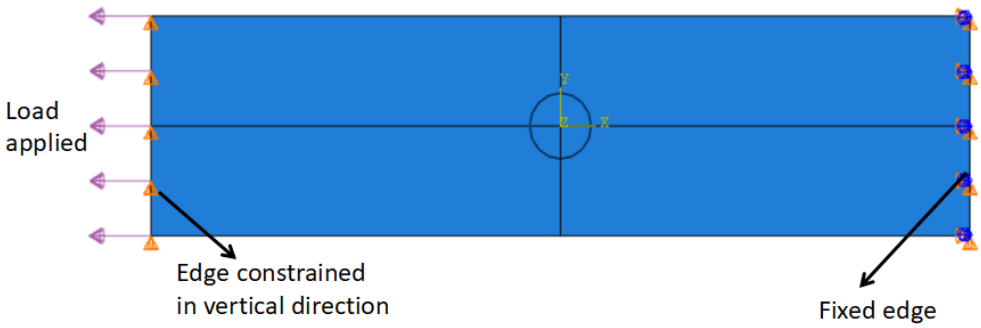

Figure 2.25: Boundary conditions and loading used in J-Integral simulations

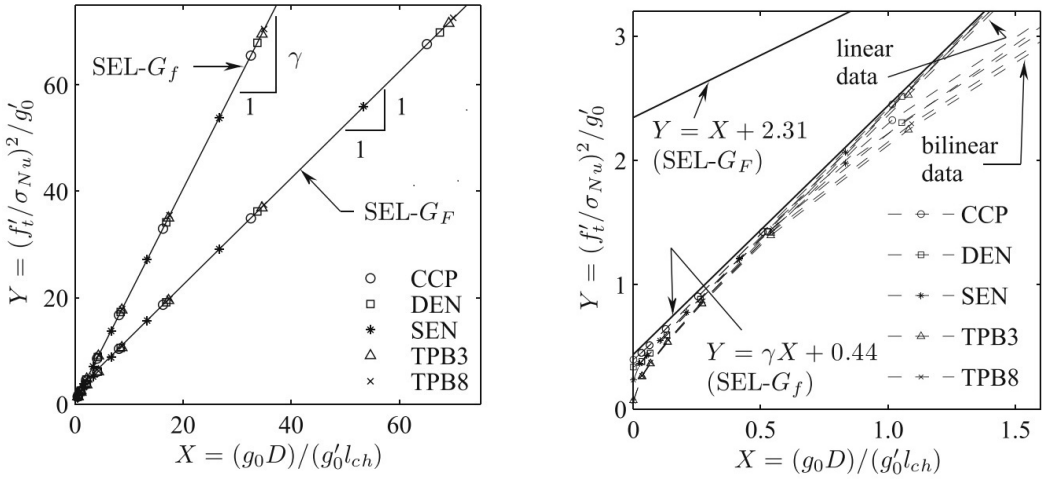

(a) Complete size effect curve showing asymptote for higher X values

(b) Initial part of the size effect plots showing the asymptote for lower X values [11]

Figure 2.26: Size effect plots in parametric space for a concave bi-linear cohesive crack law for different loading conditions [11]

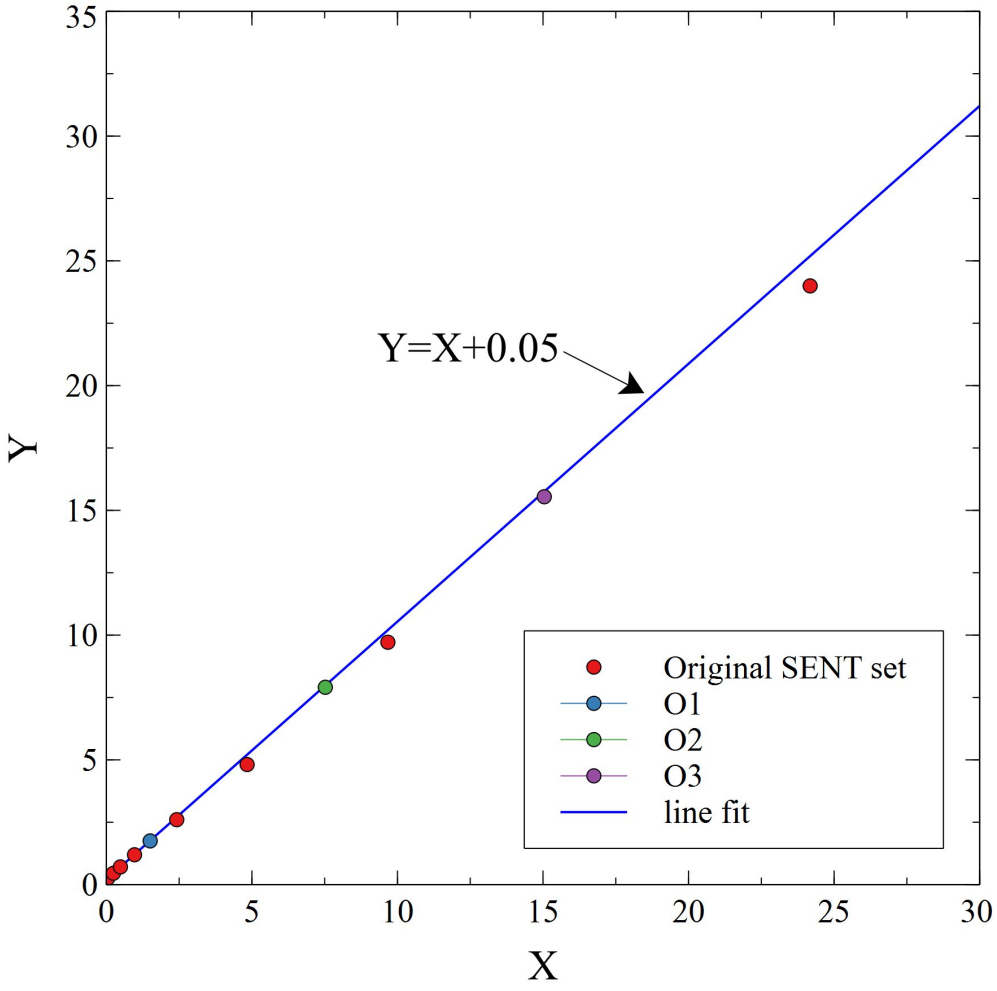

Figure 2.27: Size effect plot in X-Y parametric space for convex cohesive law shapes

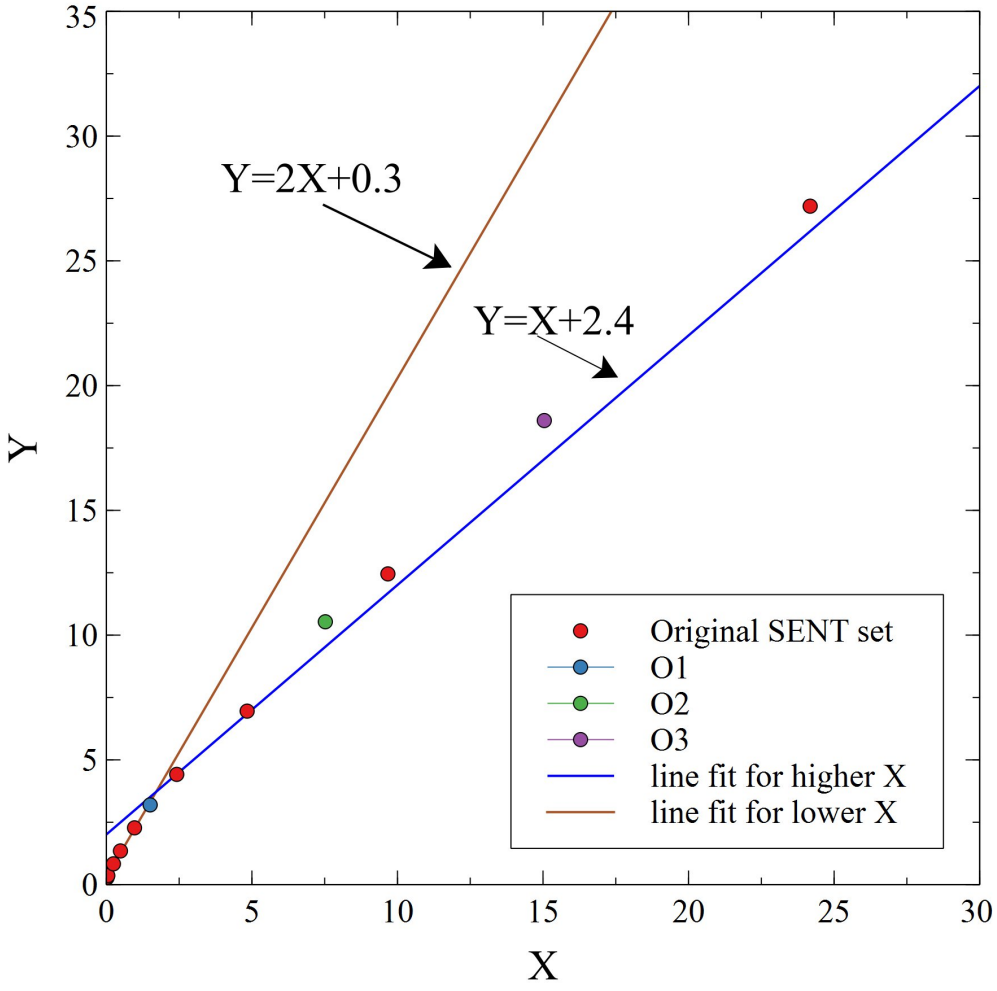

Figure 2.28: Size effect plot in X-Y parametric space for concave cohesive law shapes

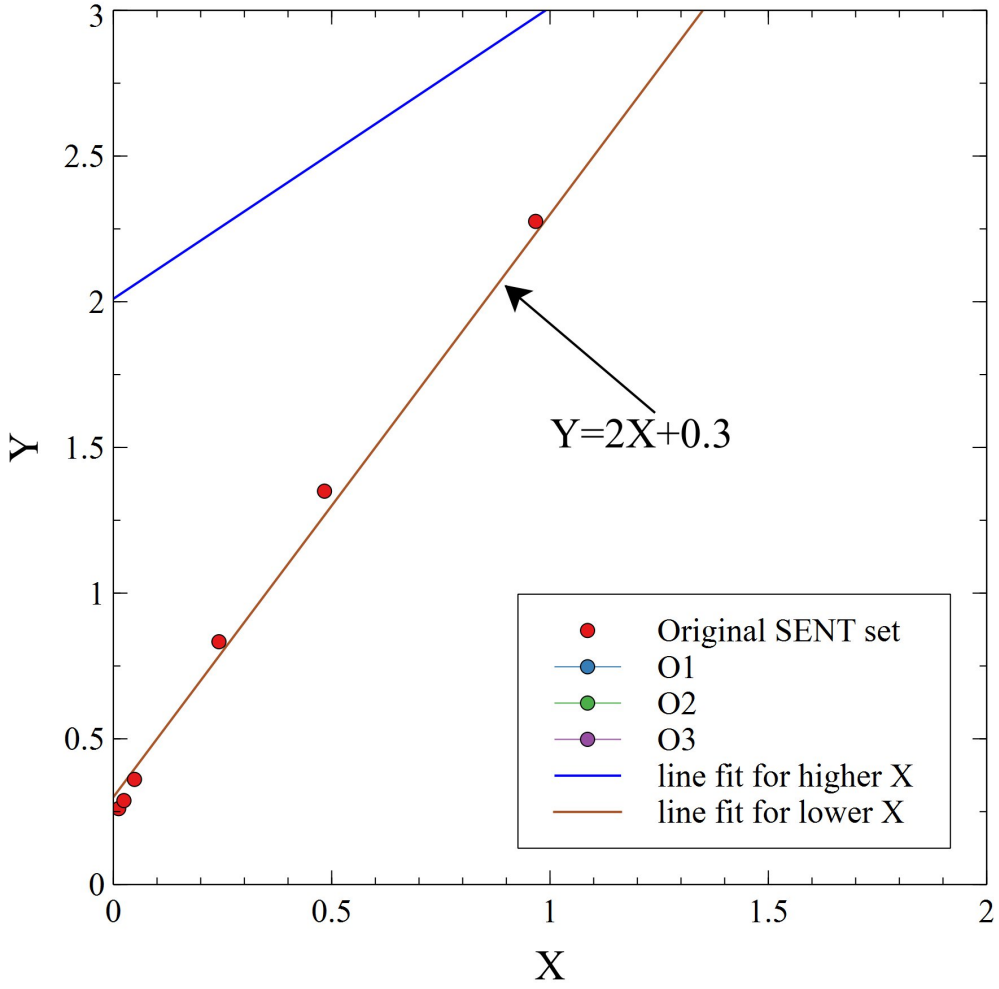

Figure 2.29: Initial portion of th size effect plot in X-Y parametric space for concave cohesive law shapes

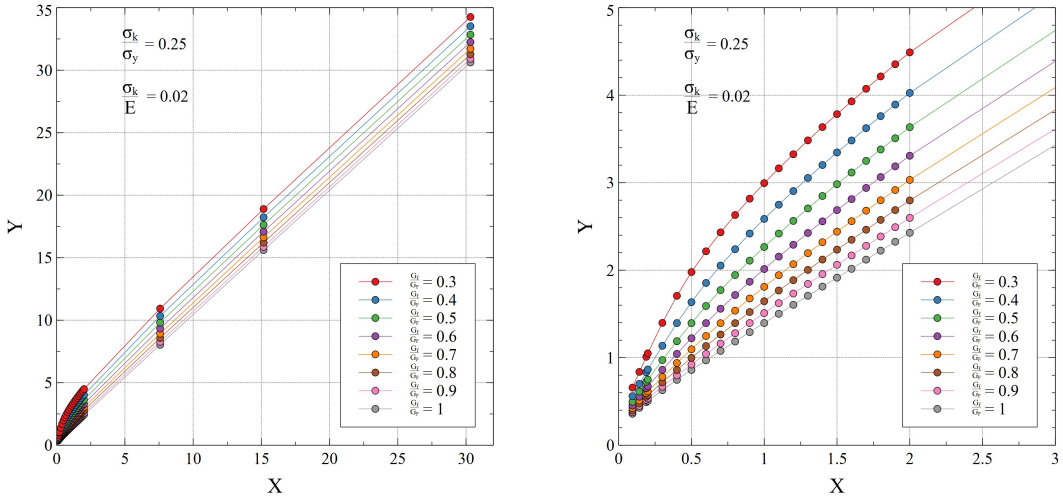

(a) Complete size effect curve

(b) Initial part of the size effect plots

Figure 2.30: Parametric plots representing size effect curves in $X - Y$ parametric space for bi-linear cohesive crack law with $k_d = 0.25$ and $\sigma_y/E = 0.02$

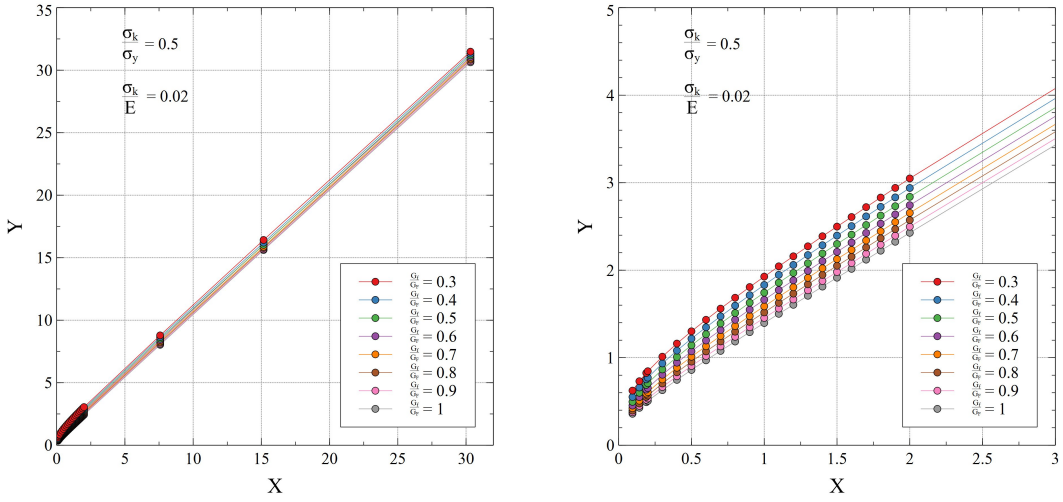

(a) Complete size effect curve

(b) Initial part of the size effect plots

Figure 2.31: Parametric plots representing size effect curves in $X - Y$ parametric space for bi-linear cohesive crack law with $k_d = 0.5$ and $\sigma_y/E = 0.02$

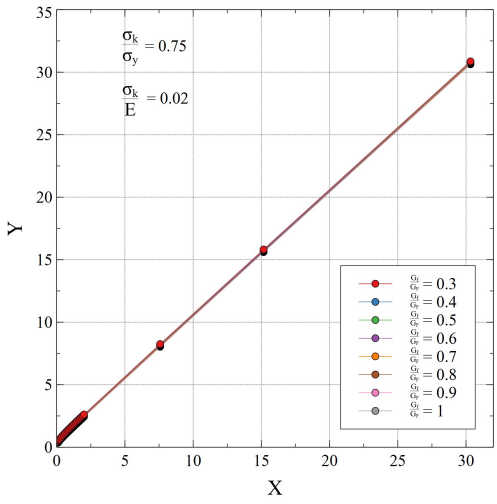

(a) Complete size effect curve

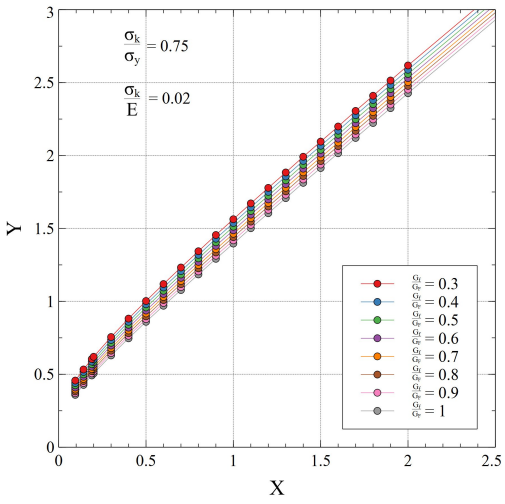

(b) Initial part of the size effect plots

Figure 2.32: Parametric plots representing size effect curves in $X - Y$ parametric space for bi-linear cohesive crack law with $k_d = 0.75$ and $\sigma_y/E = 0.02$

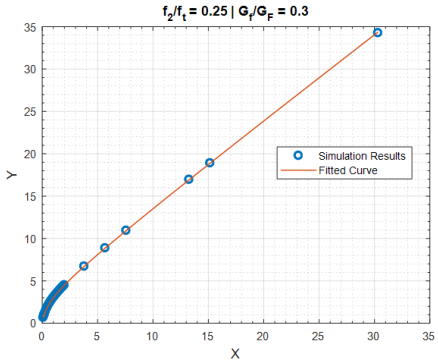

(a) Complete size effect curve with fitting equation

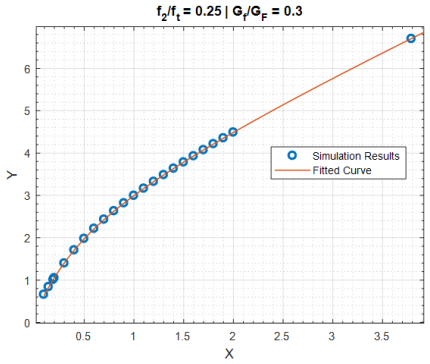

(b) Initial part of the size effect plots showing the accuracy of the fit even for lower X values

Figure 2.33: Curve fitting for plot representing size effect curve in $X - Y$ parametric space for bi-linear cohesive crack law with $k_d = 0.25$ and $\sigma_y/E = 0.02$ and $G_f/G_F = 0.3$

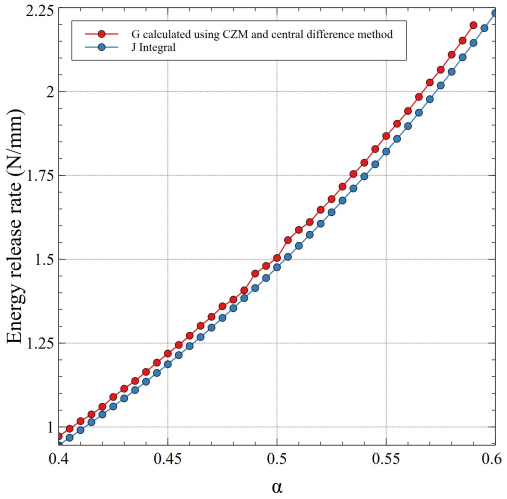

(a) Comparison of energy rate obtained using CZM with J-Integral

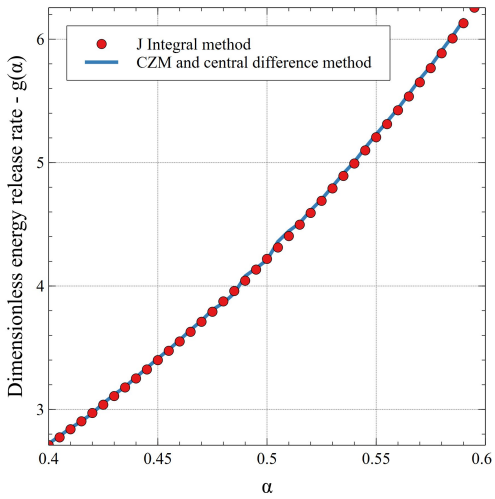

(b) Comparison of the $g(\alpha)$ values obtained using the two different techniques - the J Integral method and the CZM modeling method

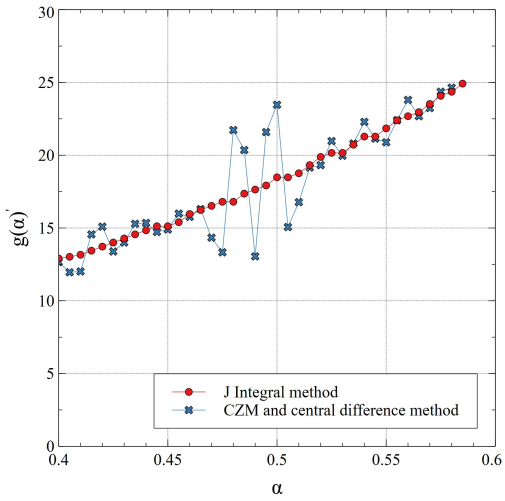

(c) Comparison of the $g(\alpha)^{'}$ values obtained using the two different techniques - the J Integral method and the CZM modeling method

Figure 2.34: Comparison of the results obtained from simulations using the CZ modeling method and the j-Integral technique

Chapter 3

EXPERIMENTAL TESTING

The modeling techniques and design protocols developed through the computational studies were implemented on Carbon/Glass hybrid specimens in an attempt to explain their fracture behavior.

3.1 Material selection

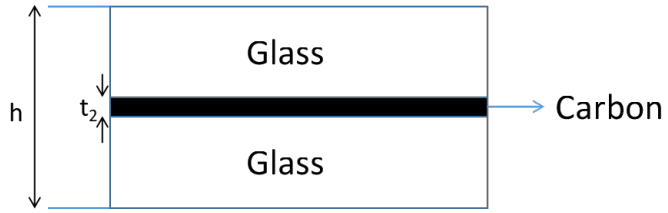

Figure 3.1: Basic layup for hybrid composite

Material selection and proper composite layup design are key steps towards ensuring that the resulting composite exhibits a positive hybrid effect. The current work uses a layup $[G_m C_n G_m]$ similar to the one used in [14] and is shown in Fig.3.1. The layup basically consists of m glass pre-preg plies on either side of n layers of the Carbon pre-preg. The idea behind [14] was to make use of thin Carbon plies to avoid the typical failure profile seen in hybrid composites (blue curve in Fig. 3.2) characterized by sudden load drops after failure of the Carbon layers. By ensuring that the thickness of the central Carbon layers is below a critical value, it is possible to obtain a relatively smooth failure profile (pseudo-ductile failure) with negligible load drops associated with Carbon ply failure - similar to the red

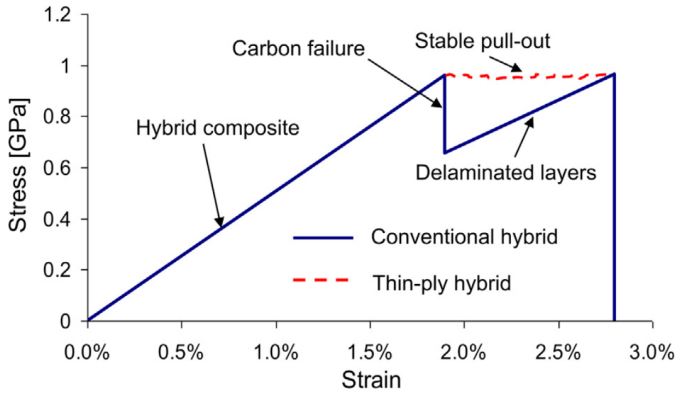

Figure 3.2: Typical stress strain curves for conventional and thin-ply hybrid laminates

dashed line in Fig. 3.2. When all the layers are aligned at 0 degrees (i.e. aligned along the loading direction)[14] mentions two main criteria which need to be met to ensure pseudo ductile failure of the hybrid:

1. The failure of one layer should not cause its sudden pullout. To prevent this, the strain energy released as a result of the failure of this layer should not exceed the fracture toughness of the interfaces. As shown in [14], comparing the strain energy of the structure before and after pullout, an expression can be obtained for the critical thickness of the material which has a low strain to failure (Carbon in the present case). A brief derivation of the critical thickness expression and the mechanics governing the pullout phenomenon has been described below.

   We consider the layup shown in Fig. 3.6. Prior to the pullout of the central Carbon layer, the equivalent Elastic modulus of the hybrid laminate is given by

$$E_{eq0} = \frac{E_1(h - t_2) + E_2 t_2}{h} \tag{3.1}$$

   where E_1 and E_2 are the moduli of the Glass and Carbon layers respectively in the

fiber direction. Once the central layer delaminates, their contribution to the stiffness of the laminate is removed and the new equivalent stiffness is given by

$$E_{eqf} = \frac{E_1(h - t_2)}{h} \tag{3.2}$$

Assuming unit length and width of the laminate, the elastic strain energy of the laminate is given by

$$U = \frac{1}{2}\sigma\varepsilon h = \frac{1}{2}\frac{\sigma^2 h}{E_{eq}} \tag{3.3}$$

where σ is the average stress applied to the laminate, ε is the longitudinal strain and E_{eq} is the equivalent modulus. The difference between the strain energies before and after pullout can be obtained by substituting E_{eq} in Eq. 3.3 with E_{eqf} and E_{eq0} from 3.2 and 3.1 and taking their difference. This difference in the strain energies is nothing but twice the energy release rate G for the pullout of the embedded layer (twice since delamination takes place on either side of the central layer). So, we have

$$G = \frac{\sigma^2 h^2}{4(E_1(h - t_2) + E_2 t_2)} - \frac{\sigma^2 h^2}{4E_1(h - t_2)} = \frac{\sigma^2 h^2 E_2 t_2}{4E_1(h - t_2)(E_1(h - t_2) + E_2 t_2)} \tag{3.4}$$

Assuming iso-strain condtions through the thickness of the laminate, we can obtain the stress on the central carbon layer σ_2 in terms of the average stress σ

$$\sigma_2 = \frac{\sigma h E_2}{E_1(h - t_2) + E_2 t_2} \tag{3.5}$$

Finally we have the expression for the interfacial fracture toughness G given by

$$G = \frac{\sigma_2^2 t_2(E_1(h - t_2) + E_2 t_2)}{4E_1 E_2(h - t_2)} \tag{3.6}$$

In the above equation, we can replace σ_2 as the strength of the Carbon pre-preg and provided all the other parameters are known, we can obtain an expression for the critical thickness t_2 of the central carbon layers.

2. Once a layer fails, the redistribution of load to the remaining layers should not cause them to fail immediately. This leads us to Eq. 3.7 from which we obtain a minimum required strength of the glass layers σ_{1min}

$$\sigma_{1min} = \frac{\sigma_2(E_1 t_1 + E_2 t_2)}{E_2 t_1} \tag{3.7}$$

Here, t_1 is the total thickness of the glass layers (upper and lower half combined).

Keeping the above criteria in mind, the materials were chosen such that they meet the strength and thickness requirements. 7781 E-Glass reinforced epoxy (NB301) matrix Unidirectional pre-preg was supplied by Mitsubishi Rayon Carbon Fiber and Composites were used as the high strain to failure material for the hybrid composites. The Carbon fiber pre-pregs - SkyFlex USN020A were supplied in kind support by SK Chemicals. The average values of the mechanical properties of the Carbon fiber pre-preg as reported in [14] were: Elastic modulus $E_2 = 101.7GPa$, strain to failure = 1.5%, Strength $\sigma_2 = 1503MPa$ and cured ply thickness $t_c = 0.029mm$. The UD glass fiber pre-pregs were tested in our lab and the average Elastic Modulus along the fiber direction was $E_1 = 43GPa$ and the ply thickness t_g was found to be $0.2125mm$

The layup was designed to have eight layers of glass in total - four on either side of the central Carbon layers, so as to facilitate flexibility in the configuration of the layup allowing us to replace one or more 0° glass layers with 90° ones as may be required. Thus, the total thickness t_1 of the eight glass layers comes to $1.7mm$. Using the above properties of the carbon and glass fiber pre-pregs and assuming $h \approx t_1 = 1.7mm$ (since the Carbon layers

are much thinner than the glass layers),the critical value of the total thickness of the central Carbon layers was obtained as $0.1479mm$.

3.2 Specimen preparation

The preparation of the samples for uni-axial tensile and fracture experiments involved the following steps:

1. **VBO (Vacuum Bag Only)** - VBO is a technique used for manufacturing high performance composites and since it does not use the autoclave, it is much cheaper and energy efficient. The composite laminates used in the present work were prepared using VBO and a schematic of the process is shown in Fig. 3.3. We start with a metal plate cleaned with acetone and subsequently apply a layer of release agent to prevent sticking of the laminate to the plate. To further prevent sticking, a piece of peel ply is affixed to the plate on which we prepare the laminate. Carbon and glass pre-preg layers cut to the desired shape and size were assembled to create the layup shown in figure 3.1 and covered with another layer of peel ply on top. We put a layer of breather on top of the layup and a small patch of peel ply and breather is placed below the lower half of the vacuum valve. Heat resistant sealant tape was affixed along the periphery of the plate and the vacuum bag was placed on top of the plate to cover everything inside. Finally the top half of the vacuum valve locks with the bottom half through a slit in the vacuum bag, thus completely sealing the system.

   It is very important to make sure that there are no air-gaps between the sealant tape and the bag because air leakages can lead to voids in the final laminate thus affecting the quality and performance of the composite. After the bag has been sealed properly, the assembly goes into a programmable oven where the vacuum valve is connected to a pump to create the vacuum. Subsequently the oven is started to run a pre-loaded program with the curing cycle for the layup. Fig. 3.5 shows the final assembly ready

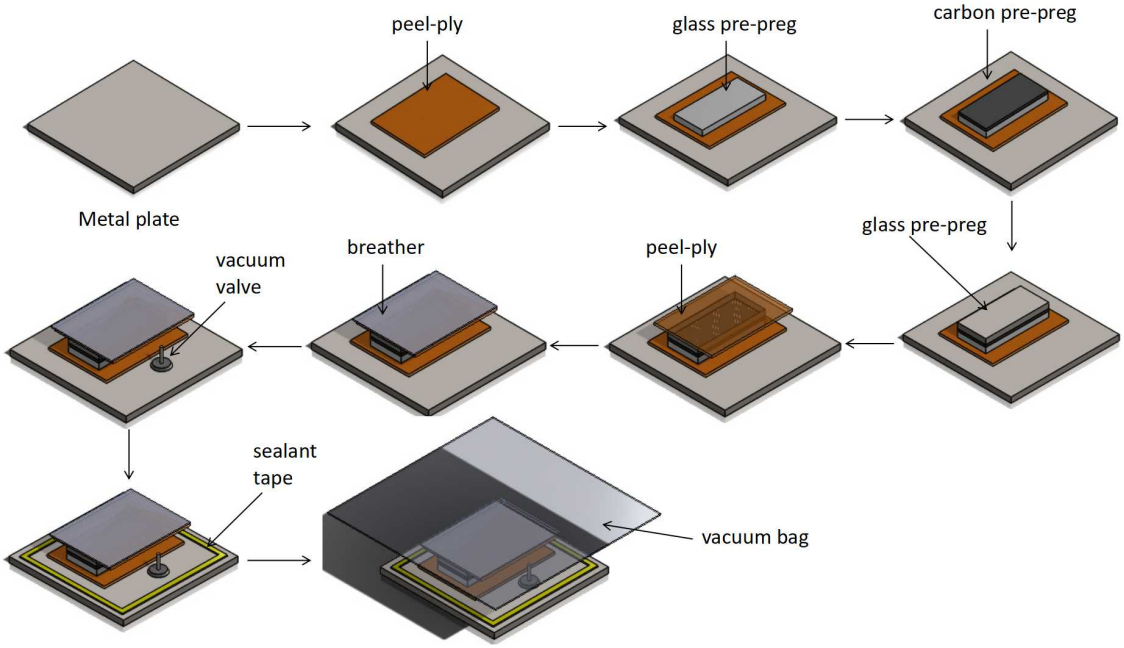

Figure 3.3: Schematic diagram of the VBO process used in manufacturing the layup

to go into the oven. The recommended curing cycle for the Carbon fiber pre-preg as provided by the suppliers is shown in Fig. 3.4.

2. **Cutting and attaching end tabs** - To ensure that failure of the specimen is not affected by stress concentration at the grips, we attach epoxy-glass tabs with chamfered edges to the gripping section of the specimen. The tabs were cut using a wet saw as shown in Fig. 3.6 and the edges were chamfered using a sanding machine (Fig. 3.7). The tabs were attached to the gripping section using an epoxy adhesive - Loctite EA E-60HP and left to cure for at least 16 hours as shown in Fig. 3.8. The surfaces of the tab and gripping section where the adhesive was applied was roughened using coarse grit sand paper prior to attaching the tabs to ensure better adhesion. The clips attached to hold the tabs tightly against the specimen (as seen in Fig. 3.8) also ensures a stronger hold.

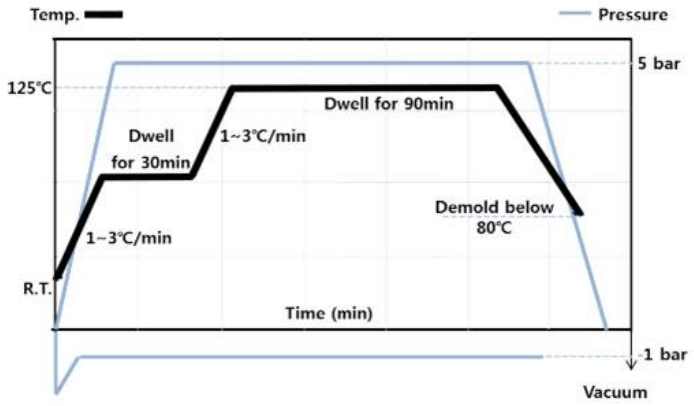

Figure 3.4: Curing cycle recommended by suppliers

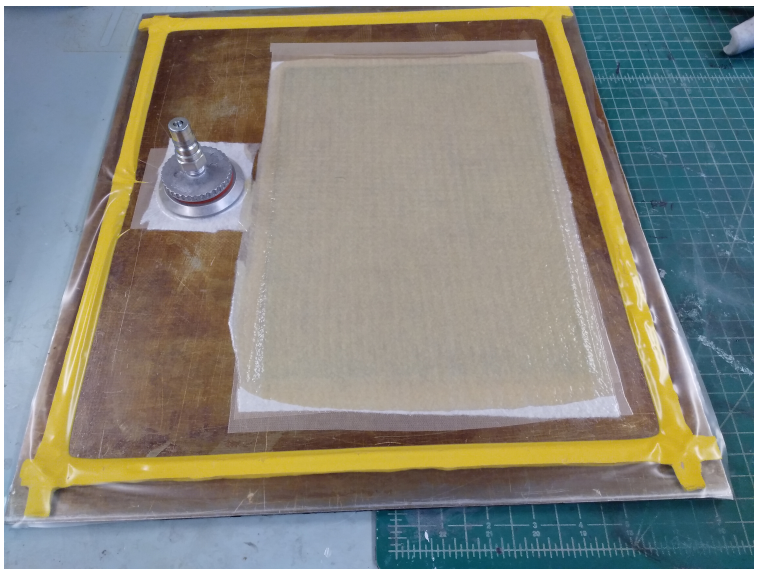

Figure 3.5: Final assembly of the vacuum bag with the layup

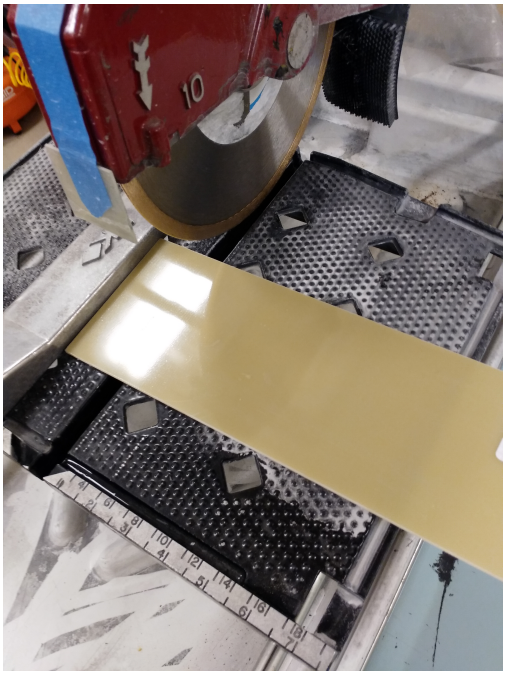

Figure 3.6: Wet saw used to cut the end tabs

3. **Speckle patterning** - In order to perform Digital Image Correlation (DIC) post testing, the gauge section of the samples were given a speckle pattern. First, we created a white background using white spray paint which was followed by a mist of black paint sprayed from a distance to create the speckle pattern. The speckled surface is shown in Fig. 3.10.

4. **Cutting individual samples** - Once the glue was cured, individual coupons of the exact dimensions as required for testing were obtained by cutting them out using a wet saw. Fig. 3.9 shows some typical specimens cut out and ready to be tested.

5. **Creating a notch/crack** - For the specimens to be used for fracture testing it was necessary to create to a crack or a pre-existing notch to initiate and control the fracture

Figure 3.7: Sanding machine used to obtain the chamfered edges

Figure 3.8: The tabs were attached to the gripping section with glue and left for about 16 hours for the glue to cure

Figure 3.9: Specimens of different sizes ready for testing

process. This was done by fastening the specimen firmly using a bench vice and then creating the notch/crack using a saw-tooth edged blade. Fig. 3.10 shows a closeup view of a speckle patterned fracture specimen with an edge crack.

3.3 Experimental setup

Uni-axial tensile experiments were performed on uncracked as well as Single Edge Notch Tension (SENT) specimens as a part of this study. Two different test setups were used.

For the relatively smaller sized samples, where the peak load was not expected to exceed 60 kN, the experiments were performed on a servo-hydraulic testing machine - Instron 8801. Two different cameras were placed on either side of the specimen to capture images of its surface as it is loaded. The first camera (Dino-Lite AM3111 0.3MP Digital Microscope),

Figure 3.10: Fracture specimen with speckle pattern

with an in-built light source, was used to capture images of the patterned surface of the gauge section to be used for DIC. A Raspberry pi 2.0 camera (need details) was positioned to capture images of the un-patterned side to observe the progression of damage as the specimen fails. The final setup used for testing on the Instron 8801 is shown in Fig. 3.11.Fig. 3.12 shows a more proximate view of the specimen being tested.

For larger sized specimens where the load was expected to exceed 60kN, an MTS 809 Axial/Torsional test system was used to perform the experiments. The components of the testing system included the testing machine and two cameras to capture images of the patterned and un-patterned surface of the specimen to be used for DIC and damage propagation studies respectively. The final setup is shown in Fig. 3.13 and Fig.3.14 gives a closer look at the specimen being tested.

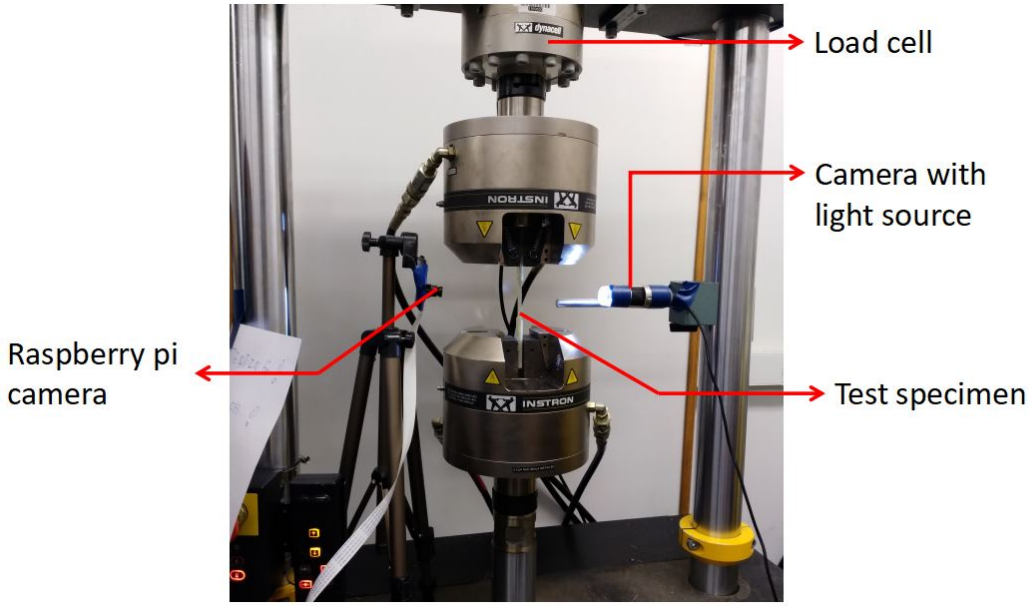

Figure 3.11: Setup for tensile/fracture testing on Instron 8801

Figure 3.12: Close-up view of the specimen being tested

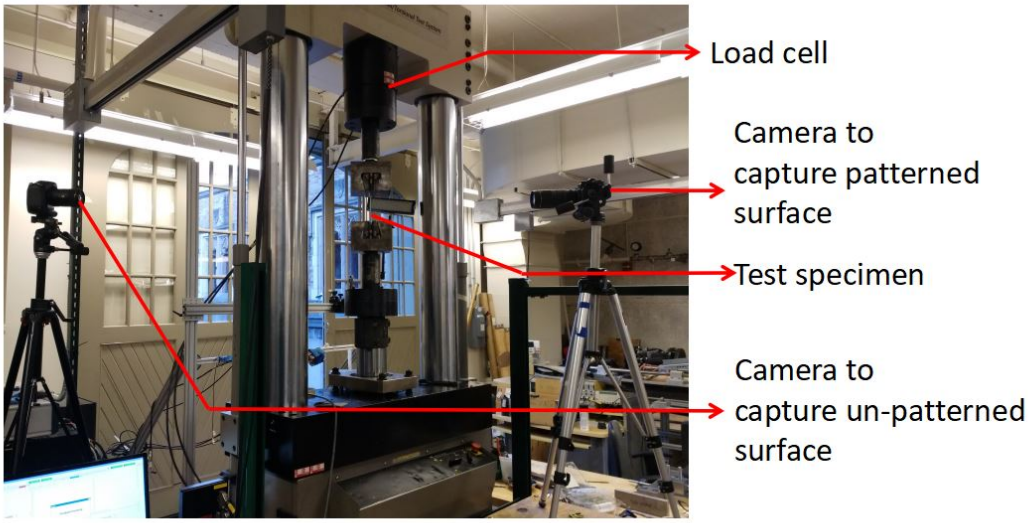

Figure 3.13: Setup for tensile/fracture testing on MTS 809 Axial/Torsional test system

Figure 3.14: A closer view of the specimen being tested on the MTS testing machine

3.4 Test procedure

A wide range of tensile and fracture tests on specimens of different sizes and layups were performed as a part of this work. As mentioned previously, all the layups tested contained four glass layers on either side of the central Carbon layers to facilitate flexibility in the quantity of the 0° and 90° glass layers contained in the layup. All the tests involved displacement controlled tensile loading of the samples in conjunction with in-situ imaging for DIC and damage propagation studies. The displacement rate was varied in proportion with the gauge length to ensure approximately similar strain rates across different specimens. As a part of the post processing, DIC was performed using an image correlation software - GOM Correlate 2017, to obtain strain. For the experiments involving specimens without a crack, the modulus was obtained by truncating the stress-strain plot to obtain the local slope in a linear part of the curve. At-least three tests were performed for each set of experiments to demonstrate repeatability of the results. The following sections include detailed information on the different types of tests performed, description of the specimens being tested and the experimental results.

3.4.1 Verification of Pseudo-ductility and hybrid effect for materials used in the present study

The authors in [14] have shown the presence of a positive hybrid effect for the $[G_2C_1G_2]$ and $[G_2C_2G_2]$ configurations. Even though the Carbon pre-pregs used in the present work is same as the ones in [14], the Glass plies were different. In order to verify the presence of a synergistic effect with the current materials it was important to perform some uniaxial tensile experiments on layups with all fibers oriented along 0 degrees.

Two sets of tests - one with one Carbon pre-preg layer at the center $[G_4C_1G_4]$ and the other with four Carbon-pre preg layers $[G_4C_4G_4]$ were performed. Since the critical value for

the total thickness of the central Carbon layers was calculated to be $0.1479mm$ as mentioned in Sec. 3.2, both the configurations, with thicknesses of approximately $0.029mm$ (for 1 Carbon layer) and $0.116mm$(for 4 carbo layers) were below the critical value and were expected to avoid catastrophic failure.

The sample dimensions were 190/50/20/2.08 mm overall length/free length/width/thickness for one Carbon layer at the center and 190/50/20/1.96 mm overall length/free length/width/thickness for four Carbon layers at the center. The displacement rate used for testing the specimens was 2mm/min.

Fig 3.15 shows a typical stress-strain plot obtained for the $[G_4C_1G_4]$ layup and a typical plot for the $[G_4C_4G_4]$ layup is shown in Fig 3.16. It was observed that both sets of experiments led to gradual transition in mechanical behavior from the failure of the first ply through propagation of damage. No sudden load drops were observed before the final damage phase towards the end. No tangible changes in the slope of the stress-strain curve - often acting as an indicator of the breaking of fibers, was observed in 3.15a. This can be attributed to the low volume fraction of Carbon fibers, as a result of which, even though the Carbon layers quite possibly failed first, the stiffness of the composite was not substantially affected and hence not apparent in the plot. Fig. 3.16a, on the other hand, shows slope changes at around 1.75% and again at 2.2% strain. The first change in slope is expected to be the signature of failure of Carbon layers thus temporarily reducing the stiffness of the composite, before the glass fibers take over completely leading to an increase in slope around 2.2% strain. When to comes to the final failure stage, the layup with one Carbon ply showed a much more stable behavior as the glass plies failed whereas the one with four carbon plies showed a sudden load drop during the failure of the glass plies. This sudden load drop is a sign of failure with relatively less warning compared to cases showing a gradual drop in load and as a result, layups with one central Carbon layer were chosen for future experiments.

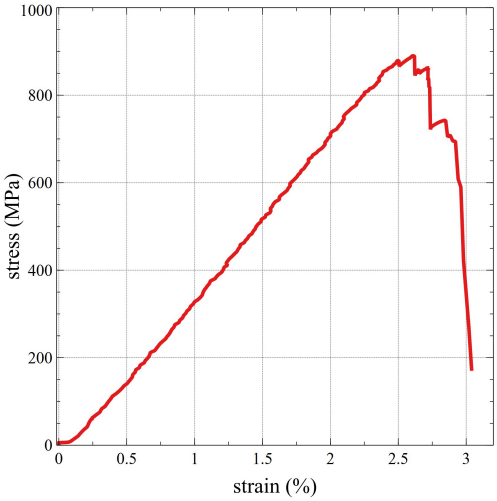

(a) Typical complete stress strain plot

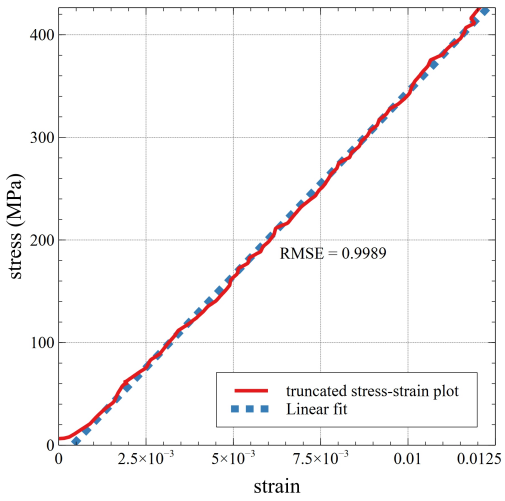

(b) Truncated stress strain plot

Figure 3.15: A typical stress-strain curve for $[G_4C_1G_4]$ layup

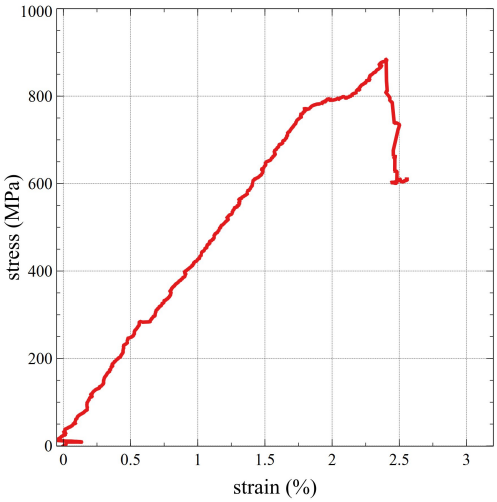

(a) Typical Complete stress strain plot

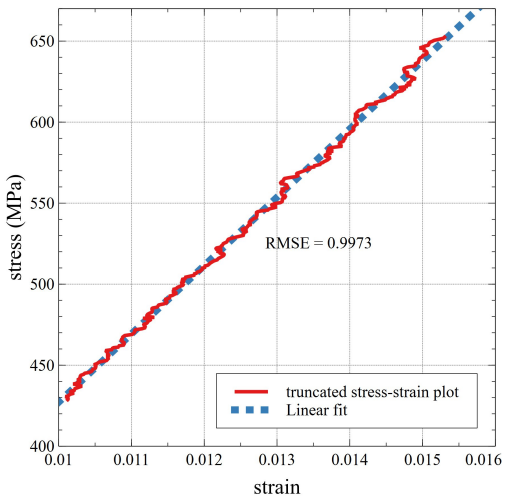

(b) Truncated stress strain plot

Figure 3.16: A typical stress-strain curve for $[G_4C_4G_4]$ layup

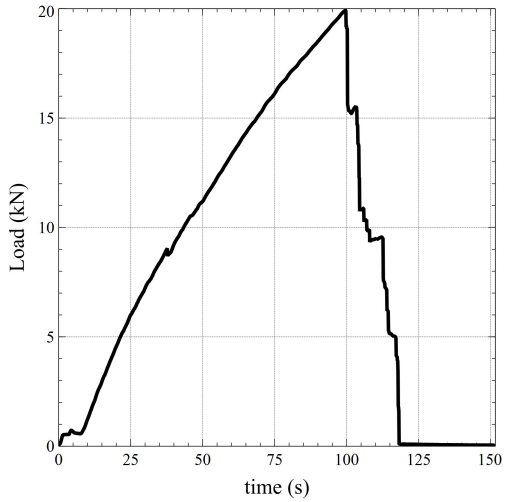

Figure 3.17: Typical load time plot for $[(G_{90})_2(G_0)_2C_0(G_0)_2(G_{90})_2]$ layup

3.4.2 Obtaining the optimal distribution of 0° and 90° glass layers

The previous set of experiments gave us an idea about how the failure behavior of the layup changes with the Carbon fiber content. Once we decided to proceed with layups containing one Carbon layer at the center, we moved on to experiments geared towards obtaining an optimal distribution of 0° and 90° glass layers on either side of the Carbon layers. It should be noted that in order to have the crack propagate perpendicular to the loading direction, it is necessary to have at least one 90° glass layer on either side of the Carbon layer.

The first set of tests were conducted on a configuration containing two 90° glass layers on either side of the Carbon layer in a $[(G_{90})_2(G_0)_2C_0(G_0)_2(G_{90})_2]$ layup. The sample dimensions were 190/50/20/1.8 mm overall length/free length/width/thickness. The displacement rate used for testing the specimens was 2mm/min. Fig. 3.17 shows a typical load vs time plot for this layup. As can be seen from the plot there is a sudden drop in load after the peak value was reached and the final failure was relatively quick. Since we trying to avoid such abrupt load drops, we did not proceed on further testing with this layup.

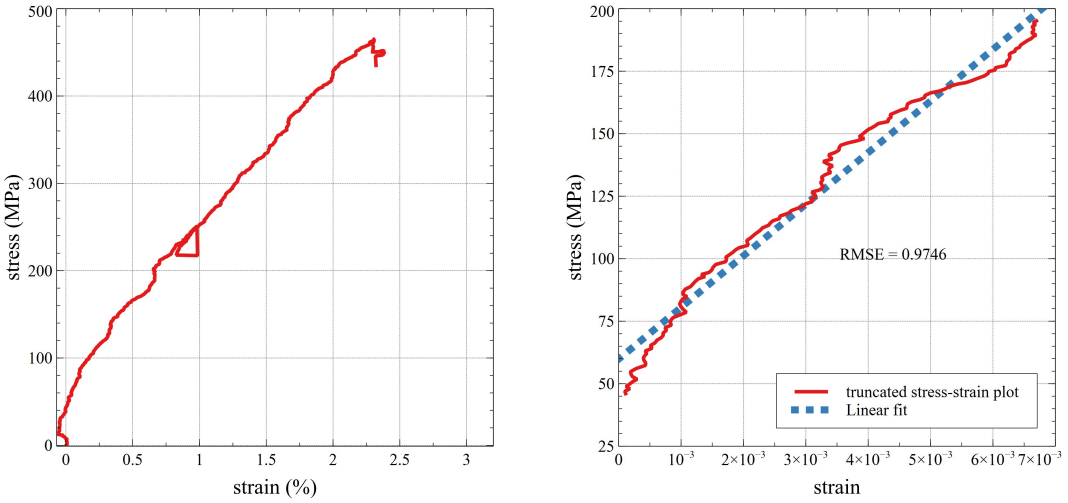

(a) Typical complete stress strain plot

(b) Truncated stress strain plot

Figure 3.18: Typical stress-strain curve for $[G_{90}(G_0)_2G_{90}C_0G_{90}(G_0)_2G_{90}]$ layup

Another set of tests were performed with a $[G_{90}(G_0)_2G_{90}C_0G_{90}(G_0)_2G_{90}]$ layup where instead of putting the two 90° glass layers together, a pair of 0° layers were sandwiched in between them. The sample dimensions and loading rate was same as that of the previous tests. Fig.3.18 shows a typical stress strain plot for this configuration and Fig.3.19 shows the load time plot. Even in this case, the load time plot shows a sudden load drop beyond the peak, as a result of which this layup was also not considered suitable for further testing. Also, in both the layups $[(G_{90})_2(G_0)_2C_0(G_0)_2(G_{90})_2]$ and $[G_{90}(G_0)_2G_{90}C_0G_{90}(G_0)_2G_{90}]$, the fact that the outer layers were 90° glass layers hindered image correlation as these layers failed at a much earlier stage compared to the 0° glass layers. Since DIC was not possible beyond a certain point of loading, the load-time plot was used to make inferences about the post peak behavior of the composite.

In order to circumvent the issues with the previous layups, a $G_0G_{90}(G_0)_2C_0(G_0)_2G_{90}G_0$ layup was considered. In this configuration, one 90° glass layer on either side of the Carbon layer was replaced by a 0° glass layer. This was expected to make it tougher than the previous

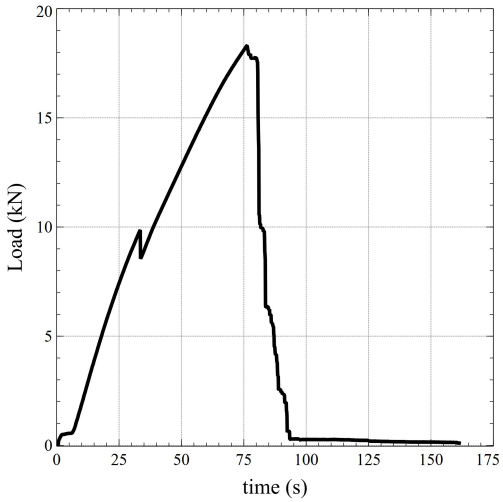

Figure 3.19: Load time plot for $[G_{90}(G_0)_2G_{90}C_0G_{90}(G_0)_2G_{90}]$ layup

layups. The displacement rate during testing and the sample dimensions were not changed. Fig. 3.20 shows a typical stress-strain curve obtained for this layup The load time plot is shown in Fig. 3.21. Even though there was a small sharp load drop just after the peak, it was followed by softening and gradual drops in load thereafter, thus exhibiting increased energy dissipation and higher toughness. This layup was thus considered to be suitable for fracture experiments.

3.4.3 Fracture experiments

The experiments discussed in the previous sections were geared towards obtaining the most suitable layup for the testing of fractured samples. To study the fracture behavior of the hybrid composite, size effect experiments were performed, where SENT specimens of three different sizes were tested. The gauge length, width and crack length were scaled across different sizes. As mentioned before, the $[G_0G_{90}(G_0)_2C_0(G_0)_2G_{90}G_0]$ layup was chosen for the fracture tests. The 20mm and 40 mm wide samples were tested on the Instron 8801 testing system and the MTS 809 Axial/Torsional test system was used for the 80 mm wide

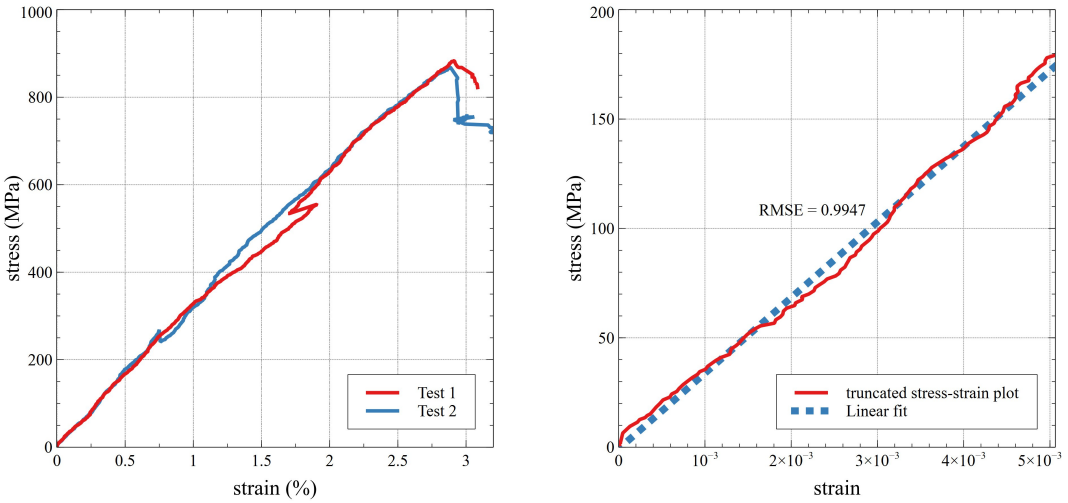

(a) Typical complete stress strain plot (b) Truncated stress strain plot

Figure 3.20: Typical stress-strain curve for $[G_0G_{90}(G_0)_2C_0(G_0)_2G_{90}G_0]$ layup

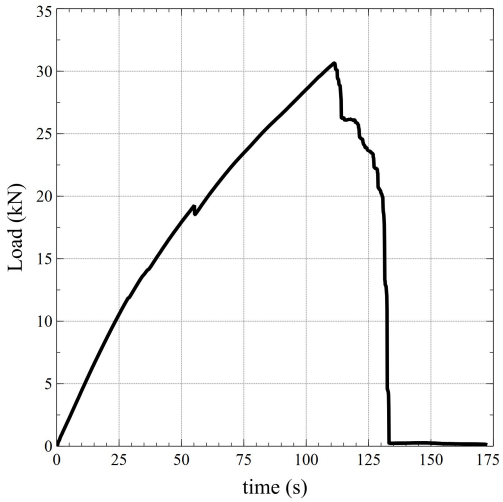

Figure 3.21: Load time plot for $[G_0G_{90}(G_0)_2C_0(G_0)_2G_{90}G_0]$ layup

Set	Gauge length (mm)	width (mm)	crack length (mm)	Displacement rate (mm/min)
1	50	20	4	2
2	100	40	8	4
3	200	80	16	8

Table 3.1: Specimen details for fracture tests

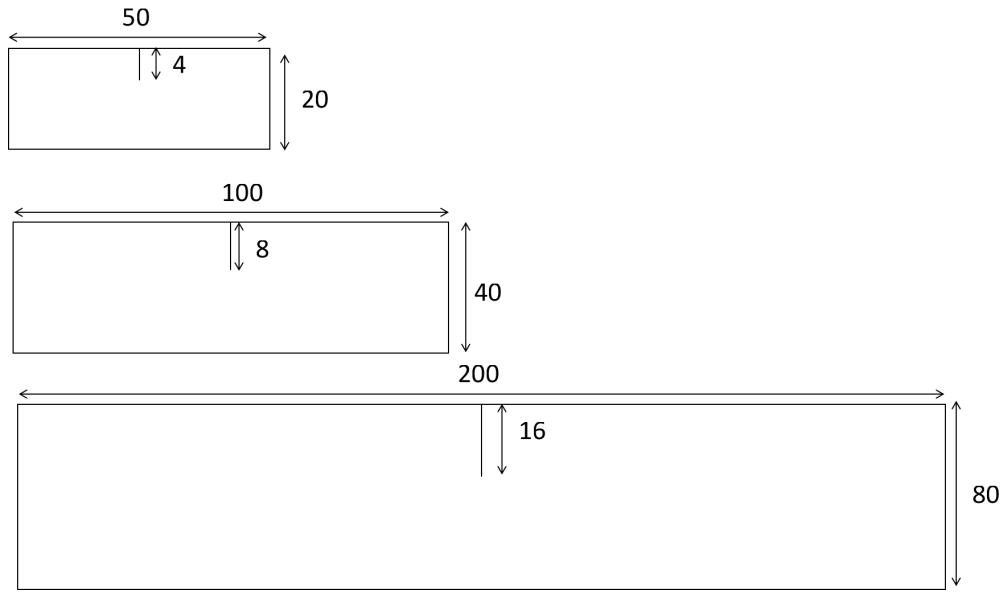

Figure 3.22: SENT sample dimensions (mm)

samples. Table. 3.1 and Fig. 3.22 give the details on specimen dimensions and displacement rates used for the fracture tests. The samples had a thickness of around $1.7mm$.

To compare the fracture behavior of the hybrid with a layup composed of only glass fibers, SENT tests were performed on a $[G_0G_{90}(G_0)_2(G_0)_2G_{90}G_0]$ layup where essentially the central Carbon layers were removed from the hybrid layup. The specimen dimensions (other than a negligible change in thickness) and displacement rates were same as that used for the hybrid.

Fig. 3.23a, Fig. 3.23b, Fig. 3.23c shows the results for fracture experiments on $20mm$ wide, $40mm$ wide and $80mm$ wide SENT samples. Fig. 3.24 is a typical load-time plot for a fracture test representative of the behavior of an SENT sample of any dimension or layup (hybrid or glass). Let tp represent the time elapsed from starting the test until the peak load is reached and tpf be the time elapsed from the point at which peak load was reached until final failure (corresponding to nearly zero load). From the load-time plots obtained from the experiments (Fig. 3.23) it is apparent that almost all the specimens show major softening, given by the fact that the time elapsed from the point at which peak load was reached till the point of final failure (tpf) was substantial. Even though it is difficult to clearly determine tp and tpf for these tests, qualitatively one can say tpf is very close to tp in magnitude for the $20mm$ wide hybrid and glass samples, which means that the duration of softening is close to the amount of time it took to reach peak load. As the specimen size increases, we can observe that the magnitude of tpf decreases relative to tp, or in other words the ratio of tpf to tp decreases with sample dimensions. If we relate this ratio to softening, we can infer that the amount of softening decreases with increase in size.

Size effect studies (discussed in Section. 2.2) were performed for the fracture experiments, where the peak nominal stress was plotted against the sample width across the different specimen dimensions on a logarithmic scale and is shown in Fig. 3.25. As seen from the plot, there is no drop in values of $log(\sigma_N)$, thus indicating that the points still lie on the initial plateau of the size effect curve and strength based criteria might be enough to characterize failure of the glass as well as the hybrid samples.

On perusing through the images and videos obtained during experiments, it was observed that the crack did not propagate across the width of the specimen in a conventional fashion. Instead, as demonstrated through Fig. 3.26, with increasing load, a splitting crack developed in front of the original crack which in turn blunted the original crack. The splitting crack propagated almost along the entire length of the specimen. Thus, after the splitting crack propagates completely, the specimen essentially behaves as a rectangular coupon of

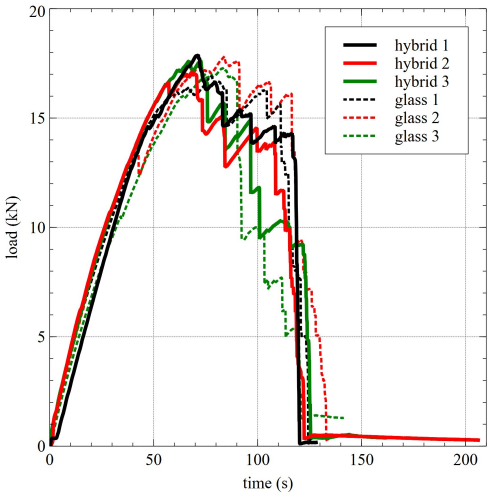

(a) Load-time plots for 20 mm wide SENT hybrid and glass specimens

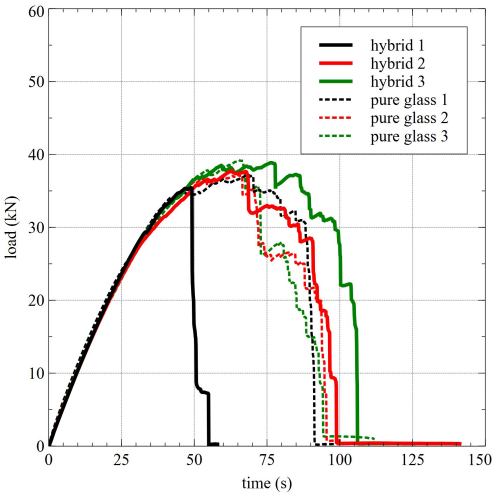

(b) Load-time plots for 40 mm wide SENT hybrid and glass specimens

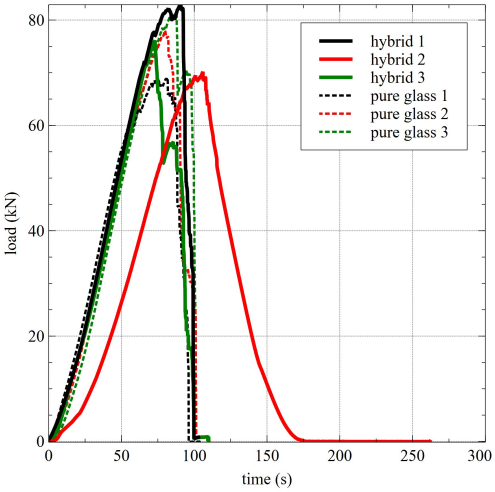

(c) Load-time plots for 80 mm wide SENT hybrid and glass specimens

Figure 3.23: Load-time plots for fracture experiments

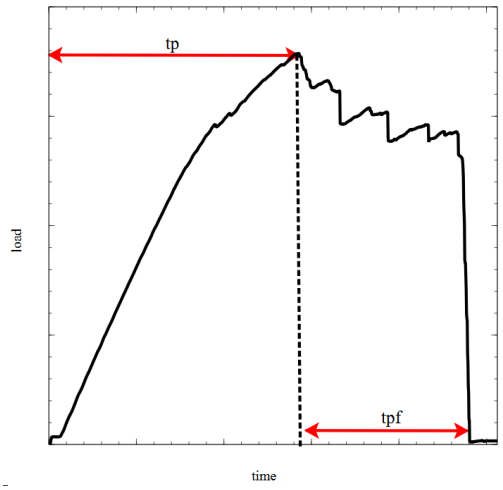

Figure 3.24: A typical load-time plot representing a fracture test on a SENT sample

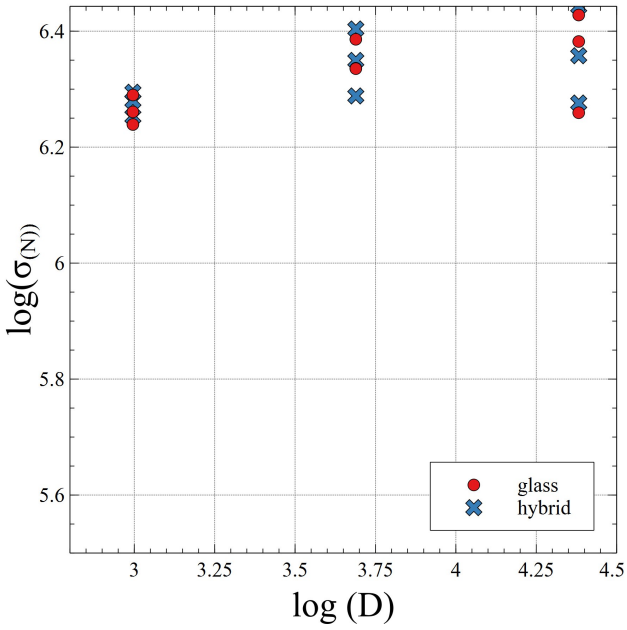

Figure 3.25: Size effect plot for fracture experiments

gauge length same as the original gauge length and a wifth slightly less (to account for the minimal crack propagation perpendicular to the loading direction) than the crack length subtracted from the original width (w-a) as shown in a very simplified schematic in Fig. 3.27. Thus this reduced rectangular coupon becomes the primary load bearing section and it is barely affected by the original crack, as a result of which it does not show the effects of stress concentration due to the notch/crack. This also explains the behavior observed in Fig. 3.25 where the peak stress remains consistent with increasing dimensions. Since the sample ceases to feel the effect of the crack post splitting, it is not surprising that the failure behavior follows a strength based criteria.

A modified size effect study was conducted where instead of plotting the peak nominal stress, the nominal stress at the point of splitting was plotted against the sample width on a logarithmic scale. Determining the point at which splitting occurred was challenging as it is not possible make a judgment based on an observation of the images using our naked eyes. Instead, DIC was performed on the images of the speckled surface of the sample obtained during testing. The Von-Mises strain was plotted and the point at which a very high localized value of strain (indicted by red contours in Fig. 3.29) was observed in front of the crack tip (the region where splitting crack originates) or when correlation failed (Fig. 3.28) for the region in front of the crack was taken as the point at which splitting was initiated and the load at that point was used to calculate the nominal stress at splitting. This technique was considered to be a fairly accurate way or determining the splitting stress. The size effect curves thus obtained is shown in Fig. 3.30. Even in this case there is no tangible drop in nominal stress with increasing structure size.

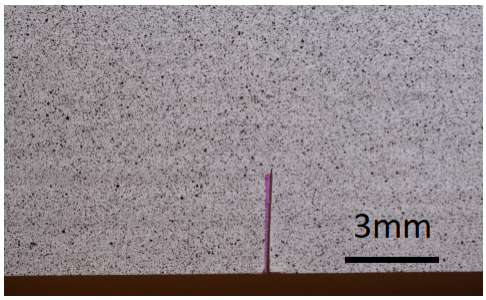

(a) Cracked sample at zero load

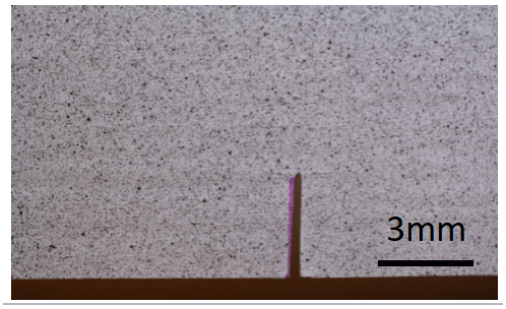

(b) Crack blunting initiates along with early stages of splitting

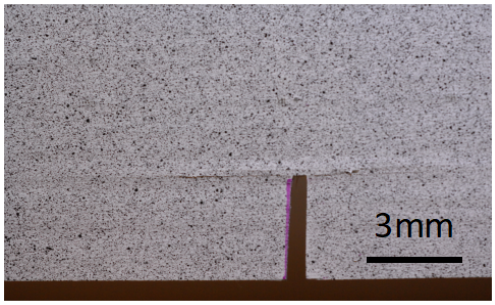

(c) Splitting crack devlops along with further blunting of crack

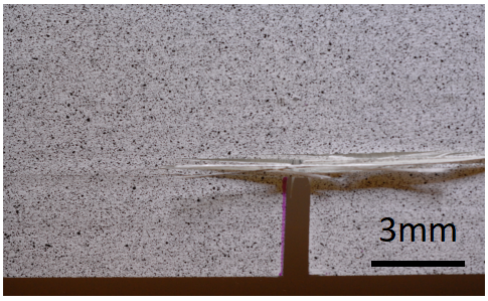

(d) Splitting crack propagates and domiantes fracture enroute to specimen failure

Figure 3.26: Images captured during experiment showing the initiation and propagation of splitting in front of crack and the resultant blunting of the crack

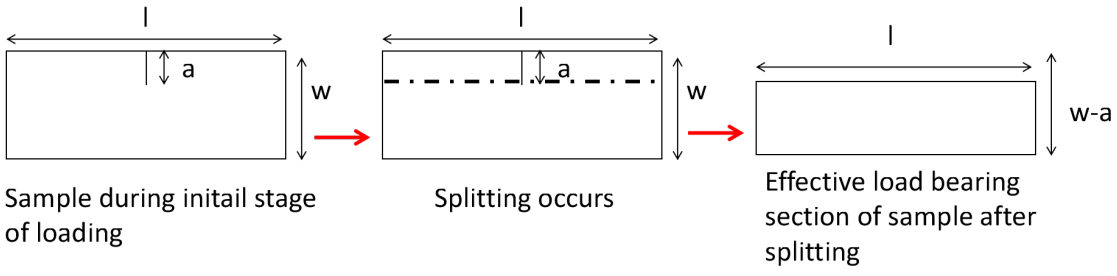

Figure 3.27: Simplified schematic depicting how the sample experiences loading after splitting

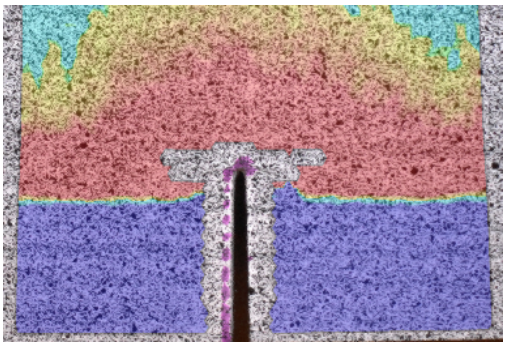

Figure 3.28: A screen shot of an instance where DIC failed in front of crack tip

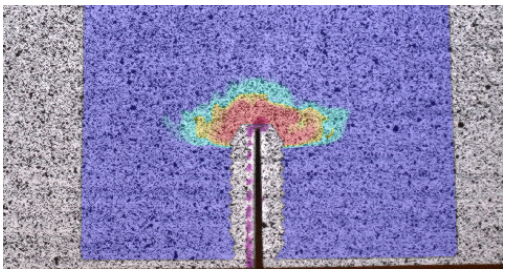

Figure 3.29: Screen shot of an instance where Von-mises strain plot showed high localization in front of crack tip

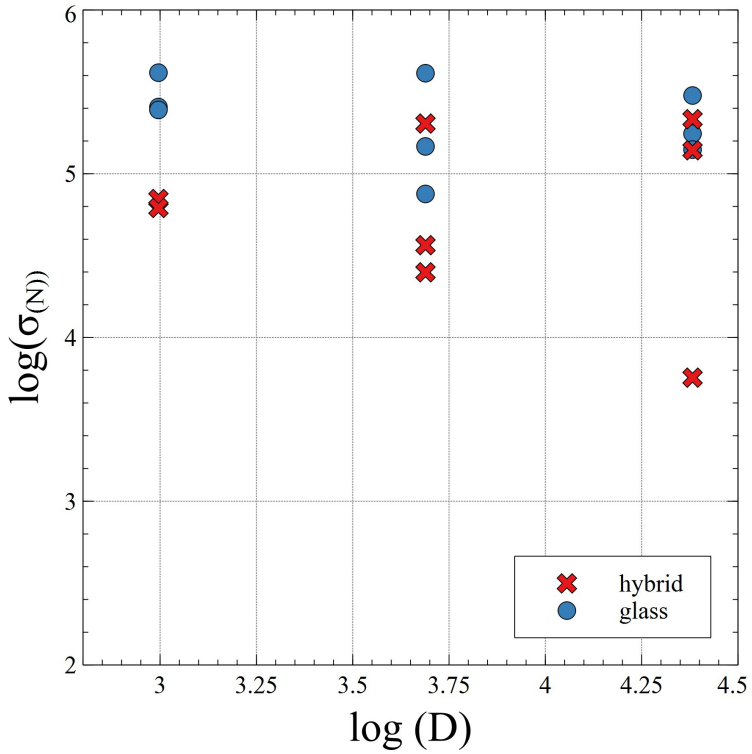

Figure 3.30: Modified size effect curves obtained using the point at which splitting occurred

Chapter 4

CONCLUSION

The domain of computational mechanics have undergone major improvements over the last few decades and along with it, the realm of fracture mechanics has seen some major improvements in modeling capabilities to simulate and capture advanced aspects of fracture. While Linear Elastic Fracture Mechanics (LEFM) and Elastic Plastic Fracture Mechanics (EPFM) concepts can explain the fracture behavior of many structures, a large class of materials such as composites, nano-composites, concrete, polymers .etc. fall into the category of quasi-brittle materials. The present work is an effort to (a) formulate a universal model for the analysis of the cohesive behavior of quasi-brittle materials and (b)leverage the obtained model to develop an experimental protocol to characterize the fracture behavior of composites. The framework was applied to pseudo-ductile composites to improve our understanding on the hybrid effect both in terms of total fracture energy and cohesive law shape.

The first stage of the work involved the development of a computational framework to capture and explain the size effect behavior of quasi-brittle materials using Cohesive zone modeling. Since a non-linear cohesive law shape is necessary for accurate modeling of a wide range of quasi-brittle materials [38], a bi-linear cohesive law shape was chosen. The damage behavior and softening aspects involved in a bi-linear cohesive crack law were discussed and a MATLAB subroutine was developed to generate bi-linear cohesive curves and Damage parameter data for any given set of cohesive parameters. This subroutine was used to generate damage variable data which was used to perform Cohesive zone simulations in ABAQUS. A wide range of models of different dimensions and mechanical properties were modeled using concave and convex cohesive law shapes and their results were analyzed. Various checks were

performed to confirm the accuracy of the simulations and the validity of the technique. The results showed that for the relative small and large structural dimensions, the failure load does not depend on the cohesive law shape, but for intermediate sizes, the failure stresses were significantly different. The size effect curves were plotted on a $X - Y$ parametric space and compared with results obtained in a previous work [11] which also studied size effect in fracture using a concave bi-linear cohesive crack law. As demonstrated by the authors in [11], if a concave bi-linear cohesive law is used, the initial part of the curves fell in line with an asymptote of slope G_F/G_f which for higher X, the curves was asymptotic to lines with unity slope. On the other hand, the convex cohesive law does not lead to the establishment of these two asymptotes as the points tend to lines with unity slope even for lower X values. The fact that size effect behavior for the present of simulations were very mich similar to that shown in [11] further validates this modeling technique.

Once the FEA modeling method was established, it was necessary to generalize the results and develop a method to extend the applicability of this technique to a wide range of situations.Taking advantage of a comprehensive dimensional analysis of the problem, the dimensionless cohesive parameters - X, G_f/G_F and k_d were chosen as the representative variables which were swept over a wide range of values to generate parametric size effect curves. These size effect curves also complied with the expected behavior seen previously for concave cohesive crack laws. Finally a general equation was conceived which uses four fitting parameters to fit any size effect curve with high accuracy. The accuracy of the fit was demonstrated for a particular case with $k_d = 0.25$, $\sigma_y/E = 0.02$ and $G_f/G_F = 0.3$.

While size effect studies in conjunction with cohesive zone crack analysis have been conducted before [11], the utility of the present work is the ability to generalize the results and develop the capability to cover a wide array of configurations and cohesive law shapes. It is an extension of the work done in [11] where the dependence of Y, which represents the failure load, was studied as a function of only X and the loading configuration. The current

computational study incorporates two other variables - k_d and G_f/G_F which makes these results much more general.This enables the use of the obtained universal cohesive size effect law for the characterization of the bi-linear cohesive law of any quasi-brittle material and specimen geometry.

Furthermore, the fitting equation gives a very powerful tool for the mechanical design community to develop damage tolerant designs for quasi-brittle structures. The existence of size effect in these structures is a major hindrance to structural design because test results for a particular set of specimen dimensions cannot be simply scaled up and down and applied to structures of other sizes. This issue is mitigated for material systems which follow a bi-linear cohesive law by using the method outlined in this work. Once 3-4 experiments are performed, the data can be used to obtain the parameters of the cohesive law. Then, the size effect curve is constructed and the corresponding fitting equation is generated by calculating the fitting parameters corresponding to this particular configuration. Once we have the fitting equation, it is very easy to obtain the failure load for any other structural dimension. All we need to do is calculate X for the required size, obtain the corresponding value of Y from the fitting equation and subsequently calculate the failure load which is directly related to Y. Thus, we do not need to perform new tests every time a new structure is required to be designed with modified dimensions. This saves a lot of time, design effort and cost. Also, in many cases it may not be feasible to perform experiments on certain structural dimensions which are either too large or too small to be tested. In such cases, the failure loads can not be predicted with accuracy if the size effect behavior is unavailable. This 'unknown' factor makes the design of such structures highly uncertain, due to which designers tend to use high values of Safety factors to account for unforeseeable failure events. The design protocol which is being established through this computational technique, which involves the use of fitting equations, will enable designers to make much more confident predictions about the failure behavior of quasi-brittle structures, thus reducing the cost of using extra material associated with high Safety factors and at the same time leading to safer structural designs.

The second part of this project involved the implementation of the modeling technique developed through the computational study to actual structures. It was intended to model the failure of Carbon-glass hybrid composites using this method.

Combining multiple materials in a structure to tailor their mechanical properties to suit specific needs is a technique which is more than a few centuries old. While there have been many instances in history where human beings have used composite materials for various small or large scale structural applications, the concept of using hybrid composites is somewhat new and has been explored by researchers since the 1970s. Synergistic effect has been established over the past few decades for Carbon-Glass hybrid composites for specific configurations and layups. This work was an effort towards investigating the fracture behavior of Carbon-glass hybrids.

Through experiments performed on scaled SENT specimens, it wad established that the hybrid composite did not show size effect behavior (for the present configuration) for fractured samples. This behavior was initially unexpected on the basis of the fact that composites tend to show quasi-brittle fracture and hence are expected to follow the fracture Size effect curve discussed previously (Sec. 2.2). This anomaly was attributed to the splitting crack failure dominating the initial phases of fracture and finally the specimen does not feel the effect of the crack and fails in a manner similar to that of a notch-less coupon with reduced width.

The splitting load was detected by DIC analysis of the images taken during the experiment and a size effect study was performed using the load at which splitting was initiated. It was observed that the splitting load was much smaller than the peak load reached during testing (around 15 to 30 % of the peak stress). Even though the fracture specimens show substantial softening after reaching the peak load and before final failure, the relatively early

onset of splitting damage is detrimental to the use of the current hybrid configuration in aerospace applications. The aerospace industry protocols for design are based on the first sign of failure, which in this case is the onset of splitting. As a result of this, even though the composite can take much higher loads and even show stable failure behavior, we will not end up utilizing its full strength due to splitting cracks originating early in its loading cycle. On the other hand, if splitting occurred at a much later stage (say 60 to 80 % of the peak load value), then we would have had a composite which not only has a high strength which can be utilized, but also shows substantial softening and can be used in critical applications, such as those in the aerospace industry, without fear of catastrophic failure. The current configuration may still be used for applications where initial signs of failure are an acceptable trade-off for a structure which has high strength and stiffness and shows a stable failure profile.

The results confirm that the the hybridization concept proposed by [14] and investigated in this work is not a suitable choice in the presence of sharp notches. Further investigations are required to clarify the role of the notch acuity and composite layup on the emergence of the first splitting crack. This will be the subject of future studies.

BIBLIOGRAPHY

[1] Leon Battista Alberti. *Ten books on architecture*. Transatlantic arts, 1966.

[2] MG Bader and PW Manders. Failure strain enhancement in carbon/glass fibre composites. *Discussion Meeting: 'Hybrid Fibre and Fibre and Particulate Reinforced Thermosets*, 1978.

[3] Grigory Isaakovich Barenblatt. The mathematical theory of equilibrium cracks in brittle fracture. In *Advances in applied mechanics*, volume 7, pages 55–129. Elsevier, 1962.

[4] Zdeněk P Bažant. Size effect in blunt fracture: concrete, rock, metal. *Journal of Engineering Mechanics*, 110(4):518–535, 1984.

[5] Zdeněk P Bažant and MT Kazemi. Determination of fracture energy, process zone longth and brittleness number from size effect, with application to rock and conerete. *International Journal of fracture*, 44(2):111–131, 1990.

[6] Goldsworthy William Brandt and Landgraf Fred. Apparatus for producing elongated articles from fiber-reinforced plastic material, February 3 1959. US Patent 2,871,911.

[7] AR Bunsell and B Harris. Hybrid carbon and glass fibre composites. *Composites*, 5(4):157–164, 1974.

[8] Harold L Cacak. Filament winding process and apparatus, June 13 1989. US Patent 4,838,971.

[9] Godofredo T Camacho and M Ortiz. Computational modelling of impact damage in brittle materials. *International Journal of solids and structures*, 33(20-22):2899–2938, 1996.

[10] Gianluca Cusatis and Luigi Cedolin. Two-scale study of concrete fracturing behavior. *Engineering Fracture Mechanics*, 74(1-2):3–17, 2007.

[11] Gianluca Cusatis and Edward A Schauffert. Cohesive crack analysis of size effect. *Engineering Fracture Mechanics*, 76(14):2163–2173, 2009.

[12] Gergely Czél, Meisam Jalalvand, and Michael R Wisnom. Demonstration of pseudo-ductility in unidirectional hybrid composites made of discontinuous carbon/epoxy and continuous glass/epoxy plies. *Composites Part A: Applied Science and Manufacturing*, 72:75–84, 2015.

[13] Gergely Czél, Meisam Jalalvand, and Michael R Wisnom. Design and characterisation of advanced pseudo-ductile unidirectional thin-ply carbon/epoxy–glass/epoxy hybrid composites. *Composite Structures*, 143:362–370, 2016.

[14] Gergely Czél and MR Wisnom. Demonstration of pseudo-ductility in high performance glass/epoxy composites by hybridisation with thin-ply carbon prepreg. *Composites Part A: Applied Science and Manufacturing*, 52:23–30, 2013.

[15] ASTM D5045-99. Standard test methods for plane-strain fracture toughness and strain energy release rate of plastic materials. Technical report, ASTM International, West Conshohocken, PA, 1999.

[16] Donald S Dugdale. Yielding of steel sheets containing slits. *Journal of the Mechanics and Physics of Solids*, 8(2):100–104, 1960.

[17] Horacio D Espinosa and Pablo D Zavattieri. A grain level model for the study of failure initiation and evolution in polycrystalline brittle materials. part i: Theory and numerical implementation. *Mechanics of Materials*, 35(3-6):333–364, 2003.

[18] Hiroshi Fukuda. An advanced theory of the strength of hybrid composites. *Journal of materials science*, 19(3):974–982, 1984.

[19] Slayter Games. Method and apparatus for making glass wool, October 11 1938. US Patent 2,133,235.

[20] Amaninder Singh Gill, Darian Visotsky, Laine Mears, and Joshua D Summers. Cost estimation model for polyacrylonitrile-based carbon fiber manufacturing process. *Journal of Manufacturing Science and Engineering*, 139(4):041011, 2017.

[21] Shale Gordon. Composite sports board such as a skateboard deck, November 18 2003. US Patent 6,648,363.

[22] Martin Granlund, Gustav Gräsberg, Hana Zrida, Martin Fagerström, and Andreas Karlsson. Increased impact resistance of cross-country ski poles by improved, simulation assisted composite design. In *Multidisciplinary Digital Publishing Institute Proceedings*, volume 2, page 318, 2018.

[23] B Harris and AR Bunsell. Impact properties of glass fibre/carbon fibre hybrid composites. *Composites*, 6(5):197–201, 1975.

[24] Keijiro Hayashi, Toshimi Awano, Masayuki Yoshikawa, Kouzou Yazawa, and Takashi Ito. Golf club head of carbon fiber reinforced plastic, May 22 1984. US Patent 4,449,707.

[25] T Hayashi, K Koyama, A Yamazaki, and M Kihira. On the improvement of mechanical properties of composites by hybrid composition.

[26] Arne Hillerborg, Mats Modéer, and P-E Petersson. Analysis of crack formation and crack growth in concrete by means of fracture mechanics and finite elements. *Cement and concrete research*, 6(6):773–781, 1976.

[27] Meisam Jalalvand, Gergely Czél, and Michael R Wisnom. Numerical modelling of the damage modes in ud thin carbon/glass hybrid laminates. *Composites Science and Technology*, 94:39–47, 2014.

[28] Meisam Jalalvand, Gergely Czél, and Michael R Wisnom. Damage analysis of pseudo-ductile thin-ply ud hybrid composites–a new analytical method. *Composites Part A: Applied Science and Manufacturing*, 69:83–93, 2015.

[29] Meisam Jalalvand, Gergely Czél, and Michael R Wisnom. Parametric study of failure mechanisms and optimal configurations of pseudo-ductile thin-ply ud hybrid composites. *Composites Part A: Applied Science and Manufacturing*, 74:123–131, 2015.

[30] IL Kalnin. Evaluation of unidirectional glass-graphite fiber/epoxy resin composites. In *Composite Materials: Testing and Design (Second Conference)*. ASTM International, 1972.

[31] G Kretsis. A review of the tensile, compressive, flexural and shear properties of hybrid fibre-reinforced plastics. *Composites*, 18(1):13–23, 1987.

[32] S Kwoleck. Wholly aromatic carbocyclic polycarbonamide fiber having orientation angle of less than about 45 (20, June 25 1974. US Patent 3,819,587.

[33] SJ Lewis. The use of carbon fibre composites on military aircraft. *Composites Manufacturing*, 5(2):95–103, 1994.

[34] Yue Liu, Bernd Zwingmann, and Mike Schlaich. Carbon fiber reinforced polymer for cable structuresa review. *Polymers*, 7(10):2078–2099, 2015.

[35] G Marom, S Fischer, FR Tuler, and HD Wagner. Hybrid effects in composites: conditions for positive or negative effects versus rule-of-mixtures behaviour. *Journal of Materials Science*, 13(7):1419–1426, 1978.

[36] G Marsh. Composites flying high (part 1), 2014.

[37] H Massengill. Applied aerodynamics commercial flight. *Aerospace America*, pages 6–7, 2005.

[38] Cory Hage Mefford, Yao Qiao, and Marco Salviato. Failure behavior and scaling of graphene nanocomposites. *Composite Structures*, 176:961–972, 2017.

[39] Richard B Millington and Robert C Nordberg. Process for preparing carbon fibers, December 27 1966. US Patent 3,294,489.

[40] Marilyn MInus and Satish Kumar. The processing, properties, and structure of carbon fibers. *Jom*, 57(2):52–58, 2005.

[41] Maria Mrazova. Advanced composite materials of the future in aerospace industry. *Incas bulletin*, 5(3):139, 2013.

[42] Alan Needleman. A continuum model for void nucleation by inclusion debonding. *Journal of applied mechanics*, 54(3):525–531, 1987.

[43] W Paton. Carbon fibre in sports equipment. *Composites*, 1(4):221–226, 1970.

[44] LN Phillips. On the usefulness of glass fibre carbon hybrids. *10th Congress: 'Innovation - the basis of reinforced plastics' Paper 21*, pages 207–211.

[45] MJ Pitkethly and MG Bader. Failure modes of hybrid composites consisting of carbon fibre bundles dispersed in a glass fibre epoxy resin matrix. *Journal of Physics D: Applied Physics*, 20(3):315, 1987.

[46] Adam Quilter. Composites in aerospace applications.

[47] Varun P Rajan and William A Curtin. Rational design of fiber-reinforced hybrid composites: A global load sharing analysis. *Composites Science and Technology*, 117:199–207, 2015.

[48] Bacon Roger. Filamentary graphite and method for producing the same, October 25 1960. US Patent 2,957,756.

[49] K Rokugo. Testing methods to determine tensile strain softening curve and fracture energy of concrete, fracture toughness and fracture energy. *Test Methods for Concerete and Rock*, pages 153–163, 1989.

[50] B Walter Rosen. Tensile failure of fibrous composites. *AIAA j*, 2(11):1985–1991, 1964.

[51] Leigh R Sargent. Carbon bodied bicycle rim, November 2 1999. US Patent 5,975,645.

[52] D Short and J Summerscales. Hybridsa review: Part 2. physical properties. *Composites*, 11(1):33–38, 1980.

[53] Richard Stewart. Rebounding automotive industry welcome news for frp. *Reinforced Plastics*, 55(1):38–44, 2011.

[54] J Summerscales and D Short. Carbon fibre and glass fibre hybrid reinforced plastics. *Composites*, 9(3):157–166, 1978.

[55] Yentl Swolfs, Larissa Gorbatikh, and Ignaas Verpoest. Fibre hybridisation in polymer composites: a review. *Composites Part A: Applied Science and Manufacturing*, 67:181–200, 2014.

[56] Yentl Swolfs, Robert M McMeeking, Varun P Rajan, Frank W Zok, Ignaas Verpoest, and Larissa Gorbatikh. Global load-sharing model for unidirectional hybrid fibre-reinforced composites. *Journal of the Mechanics and Physics of Solids*, 84:380–394, 2015.

[57] Yentl Swolfs, Robert M McMeeking, Ignaas Verpoest, and Larissa Gorbatikh. The effect of fibre dispersion on initial failure strain and cluster development in unidirectional carbon/glass hybrid composites. *Composites Part A: Applied Science and Manufacturing*, 69:279–287, 2015.

[58] Yentl Swolfs, Ignaas Verpoest, and Larissa Gorbatikh. Maximising the hybrid effect in unidirectional hybrid composites. *Materials & Design*, 93:39–45, 2016.

[59] Tetsuya Tagawa and Takashi Miyata. Size effect on tensile strength of carbon fibers. *Materials Science and Engineering: A*, 238(2):336–342, 1997.

[60] Viggo Tvergaard and John W Hutchinson. The influence of plasticity on mixed mode interface toughness. *Journal of the Mechanics and Physics of Solids*, 41(6):1119–1135, 1993.

[61] Matthew White. The great big book of horrible things. *The Definitive*, 2012.

[62] MR Wisnom. Mechanisms to create high performance pseudo-ductile composites. In *IOP Conference Series: Materials Science and Engineering*, volume 139, page 012010. IOP Publishing, 2016.

[63] FH Wittmann, PE Roelfstra, H Mihashi, Yiun-Yuang Huang, Xin-Hua Zhang, and N Nomura. Influence of age of loading, water-cement ratio and rate of loading on fracture energy of concrete. *Materials and structures*, 20(2):103–110, 1987.

[64] X-P Xu and A Needleman. Void nucleation by inclusion debonding in a crystal matrix. *Modelling and Simulation in Materials Science and Engineering*, 1(2):111, 1993.

[65] Chien-Hwa Yeh. Fabrication method of a hollow racket made of carbon fiber, June 5 1990. US Patent 4,931,247.

[66] Carl Zweben. Tensile strength of hybrid composites. *Journal of materials science*, 12(7):1325–1337, 1977.

Appendix A

MATLAB CODE AND VUMAT

VUMAT TO INCORPORATE BI-LINEAR TRACTION SEPARATION LAW

```
      subroutine vumat(
C Read only -
     1  nblock, ndir, nshr, nstatev, nfieldv, nprops, lanneal,
     2  stepTime, totalTime, dt, cmname, coordMp, charLength,
     3  props, density, strainInc, relSpinInc,
     4  tempOld, stretchOld, defgradOld, fieldOld,
     5  stressOld, stateOld, enerInternOld, enerInelasOld,
     6  tempNew, stretchNew, defgradNew, fieldNew,
C Write only -
     7  stressNew, stateNew, enerInternNew, enerInelasNew )
C
      include 'vaba_param.inc'
C
      character*80 cmname
C
C
C All arrays dimensioned by (*) are not used in this algorithm
      dimension props(nprops), density(nblock),
     1  coordMp(nblock,*),
     2  charLength(*), strainInc(nblock,ndir+nshr),
     3  relSpinInc(*), tempOld(*),
     4  stretchOld(*), defgradOld(*),
     5  fieldOld(*), stressOld(nblock,ndir+nshr),
     6  stateOld(nblock,nstatev), enerInternOld(nblock),
     7  enerInelasOld(nblock), tempNew(*),
     8  stretchNew(*), defgradNew(*), fieldNew(*),
     9  stressNew(nblock,ndir+nshr), stateNew(nblock,nstatev),
     1  enerInternNew(nblock), enerInelasNew(nblock)

        real*8       ::e,epsold(NDIR+NSHR),epsnew(NDIR+NSHR),sig_y
        real*8       ::kd,Gf_upon_GF,GF,lc,epsilon_y,epsilon_k
        real*8       ::sig_k,G_f,epsilon_2, slp1,slp2,slp3
        integer      ::i

C
        e=32700.0d0
        sig_y=900.0d0
        kd=0.2d0
        Gf_upon_GF=0.5d0
        GF=65.0d0
        lc=.05d0
        epsilon_y=sig_y/e
        sig_k=sig_y*kd
        G_f=Gf_upon_GF*GF


        G_f=G_f/lc
        GF=GF/lc

         epsilon_k=(sig_k*sig_y**2.0d0 + 2.0d0*E*G_f*sig_y -
     $ 2*E*G_f*sig_k)/(E*sig_y**2)
         epsilon_2=(2.0d0*(GF + (epsilon_y*sig_k)/2.0d0
     $ - (sig_y*(epsilon_k -
     $ epsilon_y))/2.0d0 - sig_y**2.0d0/(2.0d0*E)))/sig_k

        slp1=(sig_k-sig_y)/(epsilon_k-epsilon_y)
        slp2=sig_k/(epsilon_k-epsilon_2)

        do i = 1, nblock

        if (stateold(i,1) .GE. 0.0d0) then

        if (strainInc(i,1) .GE. 0.0d0) then
```

```
70
71              if (stateold(i,1) .LT. epsilon_y) then
72
73              epsold(1)=stateold(i,1)
74              epsold(2)=stateold(i,2)
75              epsold(3)=stateold(i,3)
76              epsold(4)=stateold(i,4)
77
78            epsnew(1)=epsold(1)+strainInc(i,1)
79            epsnew(2)=epsold(2)+strainInc(i,2)
80            epsnew(3)=0.0d0
81            epsnew(4)=epsold(4)+strainInc(i,4)
82    C
83            stressNew(i,1) = e*epsnew(1)
84            stressNew(i,2) = e*epsnew(2)
85            stressNew(i,3) = 0.0d0
86            stressNew(i,4) = (e/2.0d0)*epsnew(4)
87
88            statenew(i,1)=epsnew(1)
89            statenew(i,2)=epsnew(2)
90            statenew(i,3)=epsnew(3)
91            statenew(i,4)=epsnew(4)
92            statenew(i,5)=1.0d0
93
94            else
95
96              if (stateold(i,1) .LT. epsilon_k) then
97
98            epsold(1)=stateold(i,1)
99            epsold(2)=stateold(i,2)
100           epsold(3)=stateold(i,3)
101           epsold(4)=stateold(i,4)
102
103           epsnew(1)=epsold(1)+strainInc(i,1)
104           epsnew(2)=epsold(2)+strainInc(i,2)
105           epsnew(3)=0.0d0
106           epsnew(4)=epsold(4)+strainInc(i,4)
107   C
108           stressNew(i,1) = sig_y + slp1*(epsnew(1) - epsilon_y)
109           stressNew(i,2) = e*epsnew(2)
110           stressNew(i,3) = 0.0d0
111           stressNew(i,4) = (e/2.0d0)*epsnew(4)
112
113           statenew(i,1)=epsnew(1)
114           statenew(i,2)=epsnew(2)
115           statenew(i,3)=epsnew(3)
116           statenew(i,4)=epsnew(4)
117           statenew(i,5)=1.0d0
118
119           else
120
121           if (stateold(i,1) .LT. epsilon_2) then
122           epsold(1)=stateold(i,1)
123           epsold(2)=stateold(i,2)
124           epsold(3)=stateold(i,3)
125           epsold(4)=stateold(i,4)
126
127           epsnew(1)=epsold(1)+strainInc(i,1)
128           epsnew(2)=epsold(2)+strainInc(i,2)
129           epsnew(3)=0.0d0
130           epsnew(4)=epsold(4)+strainInc(i,4)
131   C
132           stressNew(i,1) = sig_k + slp2*(epsnew(1) - epsilon_k)
133           stressNew(i,2) = e*epsnew(2)
134           stressNew(i,3) = 0.0d0
135           stressNew(i,4) = (e/2.0d0)*epsnew(4)
136
137           statenew(i,1)=epsnew(1)
138           statenew(i,2)=epsnew(2)
```

```
            statenew(i,3)=epsnew(3)
            statenew(i,4)=epsnew(4)
            statenew(i,5)=1.0d0

            else

            epsold(1)=stateold(i,1)
            epsold(2)=stateold(i,2)
            epsold(3)=stateold(i,3)
            epsold(4)=stateold(i,4)

            epsnew(1)=epsold(1)+strainInc(i,1)
            epsnew(2)=epsold(2)+strainInc(i,2)
            epsnew(3)=0.0d0
            epsnew(4)=epsold(4)+strainInc(i,4)
C
            stressNew(i,1) = 0.0d0
            stressNew(i,2) = e*epsnew(2)
            stressNew(i,3) = 0.0d0
            stressNew(i,4) = (e/2.0d0)*epsnew(4)

            statenew(i,1)=epsnew(1)
            statenew(i,2)=epsnew(2)
            statenew(i,3)=epsnew(3)
            statenew(i,4)=epsnew(4)
            statenew(i,5)=1.0d0


            end if
            end if
            end if

            else

              epsold(1)=stateold(i,1)
            epsold(2)=stateold(i,2)
            epsold(3)=stateold(i,3)
            epsold(4)=stateold(i,4)

            epsnew(1)=epsold(1)+strainInc(i,1)
            epsnew(2)=epsold(2)+strainInc(i,2)
            epsnew(3)=0.0d0
            epsnew(4)=epsold(4)+strainInc(i,4)
C
            stressNew(i,1) = stressOld(i,1) +
            (stressOld(i,1)/(1E-14+epsold(1)))*strainInc(i,1)
            stressNew(i,2) = e*epsnew(2)
            stressNew(i,3) = 0.0d0
            stressNew(i,4) = (e/2.0d0)*epsnew(4)

            statenew(i,1)=epsnew(1)
            statenew(i,2)=epsnew(2)
            statenew(i,3)=epsnew(3)
            statenew(i,4)=epsnew(4)
            statenew(i,5)=1.0d0

            end if

            else

              epsold(1)=stateold(i,1)
              epsold(2)=stateold(i,2)
              epsold(3)=stateold(i,3)
              epsold(4)=stateold(i,4)

            epsnew(1)=epsold(1)+strainInc(i,1)
            epsnew(2)=epsold(2)+strainInc(i,2)
            epsnew(3)=0.0d0
            epsnew(4)=epsold(4)+strainInc(i,4)
```

```
C
            stressNew(i,1) = e*epsnew(1)
            stressNew(i,2) = e*epsnew(2)
            stressNew(i,3) = 0.0d0
            stressNew(i,4) = (e/2.0d0)*epsnew(4)

            statenew(i,1)=epsnew(1)
            statenew(i,2)=epsnew(2)
            statenew(i,3)=epsnew(3)
            statenew(i,4)=epsnew(4)
            statenew(i,5)=1.0d0

            end if


            end do


          return
          end

```

MATLAB CODE TO PLOT COHESIVE ZONE CURVE AND OBTAIN DAMAGE PARAMETER DATA

Contents


```
% We are using N, mm, MPa as base units
sig_y=80; %Yield strength
E=800e3; %Modulus
kd=0.8; % enter knock down factor - the ratio between kink point stress and yield stress
Gf_upon_GF=2;
GF=0.25*0.05; %enter total energy GF
lc=.05; %Element size or characteristic length. GF by default assumes a char length of 1 l
ength unit
epsilon_y=sig_y/E;
sig_k=sig_y*kd;
Gf=Gf_upon_GF*GF;

Gf=Gf/lc; %adjusting for element size or characteristic length
GF=GF/lc; %adjusting for element size or characteristic length

epsilon_k=(sig_k*sig_y^2 + 2*E*Gf*sig_y - 2*E*Gf*sig_k)/(E*sig_y^2);
%epsilon_k=(sig_y^3 + 2*E*Gf*sig_y - 2*E*Gf*sig_k)/(E*sig_y^2);

epsilon_2=(2*(GF + (epsilon_y*sig_k)/2 - (sig_y*(epsilon_k - epsilon_y))/2 - sig_y^2/(2*E)
))/sig_k;
%epsilon_2=(2*GF - epsilon_k*sig_y + epsilon_y*sig_k + epsilon_y*sig_y)/sig_k;

epsilon_1=(sig_y*epsilon_k - sig_y*sig_y/E)/(sig_y-sig_k) + epsilon_y;
```

plotting the softening curve

```
figure('DefaultAxesFontSize',15)
plot([0 epsilon_y],[0 sig_y],'b')
hold on
plot([epsilon_y epsilon_k],[sig_y sig_k],'b')
plot([epsilon_k epsilon_2],[sig_k 0],'b')

% title('Stress vs strain representing a softening curve ');
xlabel('strain');
ylabel('Stress (MPa)');
```

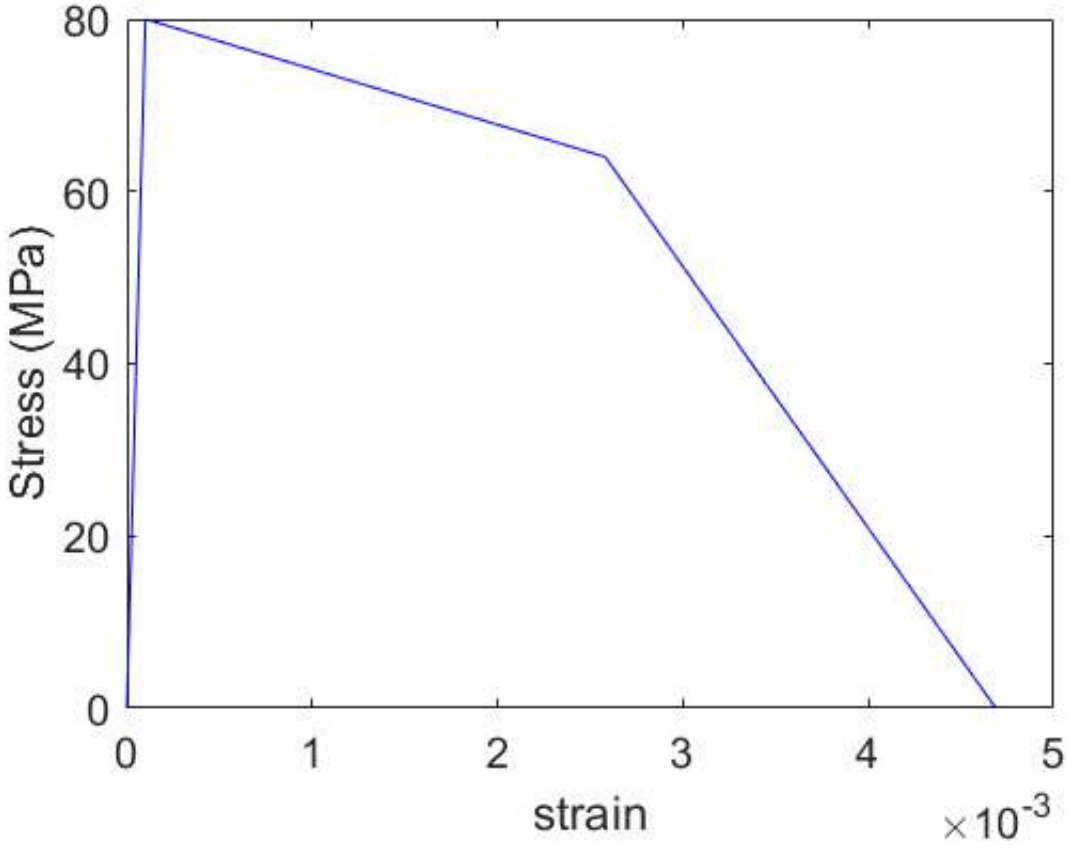

plotting damage parameter

```
ep=zeros(10000,1);
D1=zeros(10000,1);
sig=zeros(10000,1);
% ep_feed=zeros(10000,1);

figure(2)

epsilon=linspace(0,epsilon_y,100);
D=epsilon*0;

hold on;

epsilon=linspace(epsilon_y,epsilon_k,5000);
D=(E.*epsilon + ((sig_y-sig_k)/(epsilon_k-epsilon_y)).*epsilon + ((sig_k-sig_y)/(epsilon_k
-epsilon_y))*(sig_y/E) - sig_y)./(E.*epsilon);
plot(epsilon,D)
ep(1:5000)=epsilon;
D1(1:5000)=D;
% sig(1:5000)=((sig_k-sig_y)/(epsilon_k-sig_y/E)).*(epsilon-epsilon_y)+sig_y;
% sig_temp=sig(1:5000);
% ep_feed_1=epsilon'-sig_temp/E;
% ep_feed(1:5000)=ep_feed_1;

epsilon=linspace(epsilon_k,epsilon_2,5000);
D=(E.*epsilon + (sig_k/(epsilon_2-epsilon_k)).*(epsilon-epsilon_2))./(E.*epsilon);
plot(epsilon,D)
ep(5001:10000)=epsilon;
```

```
D1(5001:10000)=D;
% sig(5001:10000)=((sig_k)/(epsilon_k-epsilon_2)).*(epsilon-epsilon_2);
% sig_temp=sig(5001:10000);
% ep_feed_1=epsilon'-sig_temp/E;
% ep_feed(5001:10000)=ep_feed_1;

title('Variation of Damage parameter with strain');
xlabel('strain');
ylabel('D');

disp=ep*lc;
```

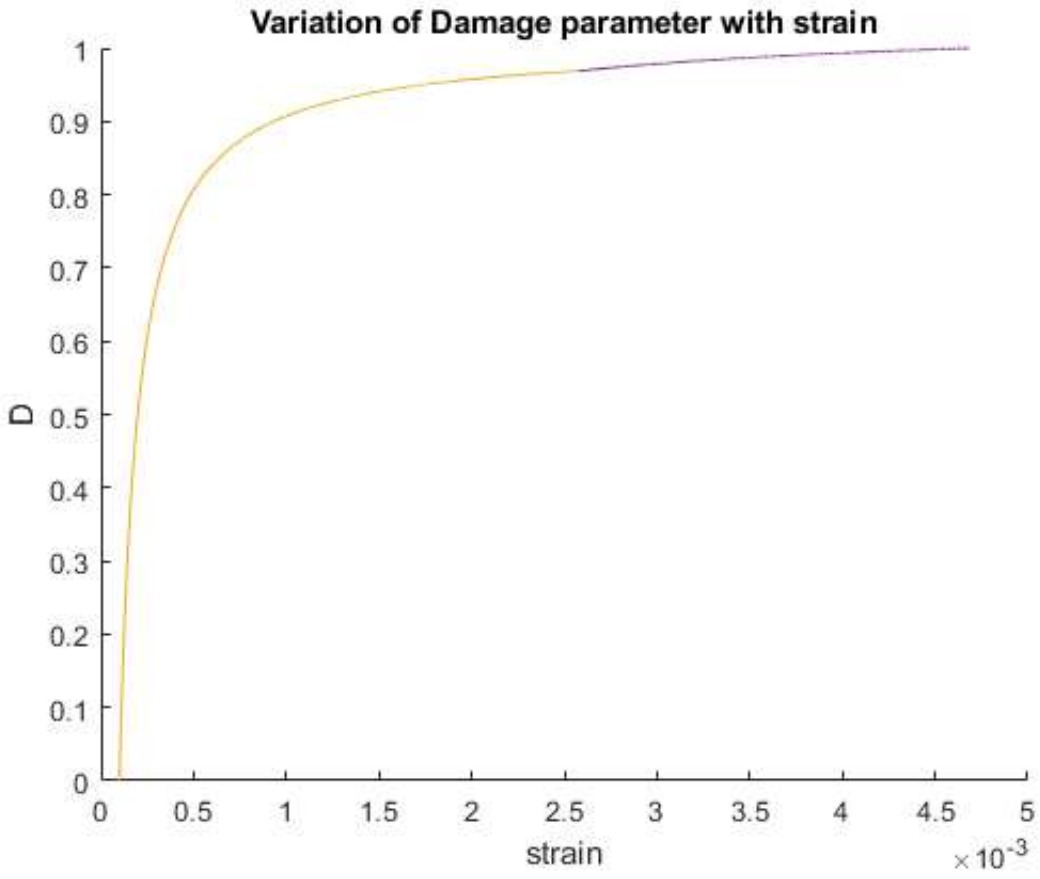

Published with MATLAB® R2017b